Published in "Active Galactic Nuclei", eds. R.D. Blandford, H. Netzer and L. Woltjer, 1990.

AGN EMISSION LINES

H. Netzter

Table of Contents

- THEORETICAL MODELS
  - The BLR and the NLR
  - Photoionization Models
  - Other Models
  - Bibliography
- PHOTOIONIZATION MODELS FOR ISOLATED CLOUDS
  - Photoionization equilibrium
  - Thermal Equilibrium
  - Additional Heating and Ionization Processes
  - Radiative Transfer
  - The Emergent Spectrum
  - Bibliography
- PHOTOIONIZATION MODELS FOR A SYSTEM OF CLOUDS
  - Spherical BLR Models
  - Non-spherical Models
  - Bibliography
- COMPARISON WITH THE OBSERVATIONS
  - The Broad Line Region
  - The Narrow Line Region
  - The Energy Budget of the BLR
  - Bibliography
- DUST AND REDDENING
  - Thermal Emission and Polarization
  - Internal and External Dust
  - Dust and Reddening in the NLR
  - Dust and Reddening in the BLR
  - Continuum Reddening
  - Bibliography
- LINE AND CONTINUUM VARIABILITY: MAPPING THE BLR
  - Line and Continuum Light Curves
  - Cross Correlation
  - The Transfer Function
  - Light Curve Modeling
  - The BLR Size
  - Anisotropic Emission and Beaming
  - Bibliography
- GAS MOTION AND DYNAMICS
  - Confined Cloud Models
  - Other Models
  - Observed Line Profiles
  - Theoretical Line Profiles
  - Cross-correlation Tests
  - Bibliography

- LINE AND CONTINUUM CORRELATIONS
  - Line Intensity vs. Continuum Luminosity
  - Line - Line Correlations
  - Line Width vs. Continuum Luminosity: M/L for AGNs
  - The Baldwin Relationship
  - AGN Accretion Disks
- QUASARS, MINIQUASARS AND MICROQUASARS
  - Narrow Line X-ray Galaxies
  - Seyfert 2 Galaxies
  - LINERs
  - AGN Classification: QI, QII and QIII
  - Bibliography
- REFERENCES
- LIST OF SYMBOLS

3. THEORETICAL MODELS

3.1. The BLR and the NLR

The first and obvious consequence of the spectral observations is the division into broad and narrow emission lines that seem to come from two distinct parts of the nucleus. The first is named the "Broad Line Region" (hereafter BLR). Its typical size, as deduced from the broad line variability, is 10-100 light-days Seyfert 1 galaxies, and up to a few light years in bright quasars. The electron density in the BLR is at least 10^8 cm^{-3}, as judged from the absence of strong, broad forbidden lines, and the typical gas velocity is 3000-10,000 $km\ s^{-1}$. The second region is the "Narrow Line Region" (hereafter NLR). Here the typical density is 10^3-10^6 cm^{-3}, and the gas velocity 300-1000 $km\ s^{-1}$. The NLR must be much larger than the BLR, since no clear variation of the narrow emission lines is observed in objects undergoing large continuum variations. The NLR is resolved by ground-based observations in several nearby Seyferts, showing dimensions of 100-300 pc. There are good theoretical reasons to believe that the NLR in bright quasars, in those cases where it is observed, is much larger than that, perhaps a few kpc in diameter.

The crude division into BLR and NLR works very well when modeling AGNs. In particular, there is no clear evidence, so far, for a transition region between the two, with intermediate dimension, density and velocity.

The general picture adopted here, and in many review papers on the subject, is that of a small continuum source, around a massive black hole, surrounded by a much larger emission line region. Support for the small dimension of the continuum source comes from the short time scale variation of the optical, ultraviolet and X-ray continuum. The situation may be different at longer wavelengths, where the observed continuum radiation can originate in a region comparable in size to the BLR. Most of the discussion in the following chapters is independent of this extra complication related to the dimension of the millimeter-infrared continuum source. The parts that are likely to depend on it are specifically explained.

3.2. Photoionization Models

Photoionization is the most likely source of excitation for the emission line gas in AGNs. The intense, nonstellar continuum is directly observed in many objects, in some cases well beyond the Lyman edge, and there is nothing to prevent this radiation from interacting with the surrounding material. Direct evidence for this is the correlated line and continuum variations in many Seyfert 1 galaxies, where the line luminosity changes are clearly a response to the continuum luminosity changes.

Some observed line ratios give further support to the photoionization assumption. For example, the *CIII* λ977 / *CIII]* λ1909 ratio is a good BLR temperature indicator for densities below about 10^{10} cm^{-3}. The observed line ratio in several quasars (an upper limit usually), indicates an electron temperature below 25,000K in the C^{+2} zone. This is well below the temperature required to ionize carbon by collisions to C^{+2}, and very typical of the temperature in a photoionized nebula.

An important concept in this kind of modeling is that of a "cloud", introduced to distinguish small individual entities in the emission line region. As explained earlier, the broad line gas is optically thick to the ionizing radiation, as deduced from the presence of strong MgII and FeII lines. On the other hand, in many objects the low and the high ionization lines have similar profiles, indicating that the line ratios are about the same throughout the emission line region. Thus a reasonable assumption is that there are many individual optically thick clouds, each one producing all the observed lines in roughly the same proportion. Later on we show that the number of clouds is very large and they occupy only a tiny part of the volume of the emission line

region. An alternative picture that has been considered involves a spherical shell around the ionizing source, producing high excitation lines from its inner part and low excitation lines from its outer part. The total continuum optical depth of the shell can be large but it is hard to imagine a dynamical situation in which the high and the low excitation lines would have similar profiles. Accepting the cloud picture, we are led to the conclusion, based on the very smooth line profiles, that the number of clouds must be very large. There is no direct way to obtain information about the shape and dimension of individual clouds and some assumptions about it must be made when constructing the model.

3.3. Other Models

Other models have been proposed to explain the observed emission lines. Shock-wave excitation is the most likely alternative. This cannot provide a full explanation of the broad line spectrum since the role of photoionization has been clearly established by the line variability observations. The situation is somewhat different in the NLR and some shock-wave models are moderately successful in explaining the narrow line spectrum. This is of greater interest in faint AGNs, in particular in LINERS. Recently, there have been several attempts to combine shock-wave and photoionization into a composite model. This is discussed in chapter 11.

A completely different, perhaps parallel view of activity and line excitation, is found in the so called "Warmers" model of AGN. In this model, the nuclear activity is due to a burst of star formation. The so called "nonstellar continuum" is in fact the spectrum of a young metal rich cluster containing a few, extremely hot, Wolf-Rayet stars. The broad emission lines and the observed variability are due, in this scenario, to supernovae explosions in the nuclear cluster. In this picture there is no need to assume a massive central object to provide the observed continuum. The model is getting to the stage that detailed calculations of the line and continuum spectra are becoming available. It has some very interesting features, as well as difficulties and drawbacks. It will not be discussed here any further.

Fast particles and radio wave heating have been mentioned, in several papers, as possible additional sources of heating and excitation. In particular, radio-loud AGNs are thought to host such an additional energy source. There is too little work, so far, to address this idea in any detail. There are some obvious drawbacks, similar to the ones associated with any model where much of the ionization is due to collisions. There are uncertainties to do with the unknown magnetic fields and the remarkably small observed differences between the emission line spectrum of radio-quiet and radio-loud objects.

The discussion in the following chapters concentrates on a particular AGN model in which the emission line region is made out of a large number of clouds that are photoionized by a central continuum source. The principles involved in this kind of modeling, and the physical processes affecting the spectrum of individual clouds, are discussed in chapter 4. Chapter 5 addresses the question of how to combine the flux emitted by many individual clouds into a composite theoretical spectrum and chapter 6 contains a detailed comparison with AGN observations.

3.4. Bibliography

References on AGN photoionization models are given in chapters 4 and 5. References on shock-heated AGN clouds are given in chapters 9 and 11. "Warmers" are discussed in a series of papers by Terlevich, Melnick and collaborators, see Terlevich and Melnick (1988) and Terlevich (1988) for references. Some papers on the role of fast particles are Ferland and Mushotzky (1984, emphasis on FeII emission) and Viegas-Aldrovandi and Gruenvald (1988, NLR models with relativistic electrons).

4. PHOTOIONIZATION MODELS FOR ISOLATED CLOUDS

4.1. Photoionization equilibrium

Consider an isolated cloud exposed to a monodirectional flux of ionizing photons. Let L_ν be the monochromatic luminosity of the central source, per unit frequency, and r the cloud-center distance. Consider a point at a depth s into the cloud, where the optical depth is τ_ν. Assume also that all ions are in their ground level and the ionization field is not very intense. The rate of photoionization events per unit volume, of an ion X^i with a number density N_{X^i}, is

$$N_{X^i} \int_{\nu_0}^{\infty} \frac{L_\nu e^{-\tau_\nu} \sigma_\nu(X^i)}{4\pi r^2 h\nu}\, d\nu, \qquad (2)$$

where ν_0 is the threshold ionization frequency and $\sigma_\nu(X^i)$ the photoionization cross section. The rate of the inverse process, radiative recombination, is

$$\alpha(X^{i+1})N_{X^{i+1}}N_e, \tag{3}$$

where N_e is the electron density and $\alpha(X^{i+1})$ is a recombination coefficient which includes recombinations to all levels.

If L_ν, is not varying in time or the recombination time, $t_{rec} = 1 / \alpha(X^{i+1}) N_e$, is short enough, the ionization fraction $N_{X^{i+1}} / N_{X^i}$ can be solved for by equating (2) and (3). The overall degree of ionization is found by solving such equations for all successive stages of ionizations, with the additional requirement on the total abundance of X,

$$N_{X^1} + N_{X^2} + \ldots = N_X. \tag{4}$$

Evidently, the degree of ionization depends on the ratio of the ionizing photon flux to the gas density. It is convenient therefore to introduce an *ionization parameter* that specifies this ratio. The ionization parameter for hydrogen, at the illuminated face of the cloud, is designated U and is given by

$$U = \frac{ionizong\ photon\ flux}{cN_e} = \frac{\int_{\nu_0}^{\infty} L_\nu d\nu/h\nu}{4\pi r^2 c N_e}, \tag{5}$$

where c is the speed of light which is introduced to make U dimensionless. (1) As explained below, typical values for U in AGN clouds are 10^{-3}-1.

In principle there is a different ionization parameter for each element and at each point in the cloud. In practice, U as defined for hydrogen at the front of the cloud, is very useful and characterizes the overall level of ionization very well. For example, in quasars' BLR clouds,

$$\frac{N_{H^+}}{N_{H^0}} \simeq 10^{5.3}U \quad and \quad \frac{N_{He^{++}}}{N_{He^+}} \simeq 10^{3.2}U. \tag{6}$$

This approximate relation is already enough to estimate the size of the broad line clouds. The photoionization cross section for hydrogen ($\sigma_\nu(H^0)$) at 1 Rydberg is about 6.3×10^{-18} cm^2. Using the estimated degree of ionization from (6) with $U = 0.1$, for a density of $N_e = N_H = 10^{10}$ cm^{-3}, we find that an optical depth of 10 at the Lyman limit corresponds to a physical thickness of ionized hydrogen of about 3×10^{12} cm. The column density of ionized gas is about 3×10^{22} cm^{-2}. The amount of neutral material is not well known (see below) but a rough estimate for its column density is some 10 times the column of ionized gas. If clouds are roughly spherical, and they cover about 10% of the source (chapter 2), we need more than 10^7 clouds in a bright AGN whose BLR radius is of the order of 0.1 pc. (chapter 8). The associated filling factor (the fraction of the total volume filled with such clouds) is tiny, of the order of 10^{-12}! The number of clouds is smaller for less luminous AGNs, especially if they are non-spherical, or have much larger neutral zones. Note also the small Compton depth of such clouds, which is the main reason for neglecting electron scattering in most of the following discussion.

The ionization parameter is also a measure of the way the ionization structure is changing, and it is easy to show that the thickness of ionization fronts is inversely proportional to U. Thus a large ionization parameter corresponds to sharp transition between successive stages of ionization and small U results in thick regions of gradual change in the level of ionization.

The steady state ionization structure is obtained by solving the ionization and recombination equations for all elements and at all points in the cloud. Ionization from all levels must be considered as well as corrections due to induced processes. For example, the photoionization rate per unit volume from the hydrogen level i is

$$n_i \int_{\nu_i}^{\infty} \frac{L_\nu e^{-\tau_\nu}\sigma_\nu(i)}{4\pi r^2 h\nu}[1 - \frac{\exp(-h\nu/kT_e)}{b_i}]d\nu, \tag{7}$$

where the second term on the right is the correction due to induced recombination and b_i is the departure coefficient for the level. The continuum optical depth includes a similar correction factor, thus

$$d\tau_\nu = \sigma_\nu(i)n_i[1 - \exp(-h\nu/kT_e)/b_i]ds. \tag{8}$$

Stimulated processes are important in regions of intense radiation fields and they are usually more important for high energy levels. The innermost part of the BLR is one place where they should not be neglected.

The photoionization of heavy ions by high energy X-ray photons is somewhat more complicated to treat. Such photons can eject a K-shell electron and the following ionic readjustment can often cause a removal of an additional electron. This "Auger effect" couples the ion X^i to X^{i+2}. The process is important in regions of the cloud where much of the softer ionizing radiation has already been exhausted and only the small cross-section, high energy photons can penetrate. The removal of L-shell electrons ($2s$, $2p$) is important too at high photon energies. Generally speaking, in a solar composition material with $T_e \sim 10^4$ K, the main sources of opacity between 1 and 20 *Ryd* are H^0, He^0 and He^{+1}. The metal opacity is more important at higher energies; carbon, nitrogen and oxygen up to ~ 50 *Ryd* and iron etc. beyond that. Much of the X-ray opacity is due to K-shell absorption, which is not very sensitive to the exact degree of ionization. Thus the opacity at those frequencies reflects mainly the chemical composition of the gas and not its degree of ionization.

Photoionization from excited levels is, in some cases, of great importance. An example is the ionization of O^{++} from the two metastable levels, $^1S_0$ and $^1D_2$. These levels are in their Boltzmann population in AGN high density clouds, and photoionization out of them has a comparable rate to the ground level photoionization. The ground level ionization threshold of O^{++} is just short of the He^+ ionization edge, at 54.4 eV. The gas opacity at all energies higher than 54.4 eV is almost entirely controlled by He^+, whose abundance is very high, and the O^{++} ground level opacity plays almost no role. The O^{++} metastable levels ionization is about 5 eV lower than the ground level ionization. This extends the O^{++} photoionization cross section into frequencies where it may become a dominant source of opacity. It can influence, in some cases, the ionization of C^{++} (threshold at 47.9 eV) which has a large effect on the local cooling and line emission. Other important examples of this type are ionization from excited states of N^0 and Mg^+.

The ionization structure in AGN clouds is very different from that of HII regions and planetary nebulae. The clouds can be thick enough to be highly ionized (N^{+4}, O^{+5}) at their illuminated face and almost completely neutral at the back. The large flux of X-ray photons maintains a low degree of ionization (~ 10%) over a large part of the cloud, more than 90% of its thickness in some cases. Such extended low ionization regions are thought to be the origin of the strong FeII and MgII lines. The ionization structure in the highly ionized part depends on the value of U. Large (~ 0.1 - 1) U results in sharply defined ionization fronts. Smaller U enables several stages of ionization to co-exist over large parts of the cloud.

---

[1] The term *ionization parameter* has been used loosely in the literature. In some papers it is not divided by c, which leave it in velocity units. Some authors define it as $L_\nu / 4\pi r^2 hN_e$ at a chosen frequency (usually at 1 Ryd.) and in other cases (chapter 9) it is the ratio of radiation pressure to gas pressure (i.e. divided by the temperature). Back.

4.2. Thermal Equilibrium

The equilibrium temperature of the gas is the result of heating, by absorption of the central source radiation, and cooling via several atomic processes. The temperature referred to is the kinetic temperature of the charged particles, or the *electron temperature*, T_e, which is well defined for all particles with a Maxwellian distribution of kinetic energies. It should not be confused with the *radiation temperature* (or color temperature), T_{rad}, characterizing the radiation field or the *excitation temperature*, T_{ex}, describing the populations of the atomic levels. Conditions in gaseous nebulae are far from thermodynamic equilibrium and T_e is usually different from both T_{rad} and T_{ex}. However, in some AGN clouds the density and optical depth are large enough so that for some ions $T_{ez} = T_{ex}$, i.e. the level populations are given by the Boltzmann excitation equation.

The most important heating-cooling processes in AGNs clouds are:

4.2.1. Bound-free heating-cooling. Consider the absorption of a photon with energy $h\nu$ by the ion X^i in a level whose threshold ionization frequency is ν_0. The initial kinetic energy of the freed electron is ($h\nu$ - $h\nu_0$), and this energy is quickly spread, by elastic collisions, among the charged particles. [(2)] The heating rate per unit volume due to this ionization is

$$N_{X^i} \int_{\nu_0}^{\infty} (h\nu - h\nu_0) \frac{L_\nu e^{-\tau_\nu} \sigma_\nu(X^i)}{4\pi r^2 h\nu} d\nu. \quad (9)$$

Summation over all levels of all elements gives the total bound-free heating. A correction due to stimulated recombination, as in equation (7), must be included in some cases.

The average energy of a recombining electron is close to kT_e and the total energy loss due to spontaneous radiative recombination is obtained by summing over expressions of the form

$$\alpha_T(X^{i+1}) N_e N_{X^{i+1}} k T_e, \quad (10)$$

for all ions and all levels. Here α_T is an *energy averaged recombination coefficient* which is somewhat different from the coefficient α used in equation (3).

4.2.2. Free-free heating-cooling. The free-free heating rate per unit volume, due to the ion X^{+Z}, is

$$\int_0^{\infty} \frac{L_\nu e^{-\tau_\nu(ff)} \sigma_\nu(ff)}{4\pi r^2} d\nu, \quad (11)$$

where

$$\sigma_\nu(ff) = 3.69 \times 10^8 g_{ff}(\nu, T_e) \nu^{-3} T_e^{-1/2} N_e N_{X+z} Z^2 [1 - \exp(-h\nu/kT_e)]. \quad (12)$$

In this equation $g_{ff}(\nu, T_e)$ is the thermal average of the Gaunt factor and allowance is made for stimulated emission.

Free-free absorption is a significant heating source for the gas in cases of intense low frequency radiation and large columns of ionized gas. Most low density nebulae are optically thin to free-free absorption, but some BLR clouds, with densities exceeding 10^{10} cm^{-3} and large column densities, may become opaque to this radiation, especially at low frequencies. For example, a unit free-free optical depth at a wavelength of 30 μm, for $N_e = 10^{10}$ cm^{-3} and $T_e = 10^4 K$, is obtained for a column density of $\simeq 10^{22}$ cm^{-2}.

Free-free cooling is the result of bremsstrahlung events converting some kinetic energy into radiation via electron-ion Coulomb collisions. The rate, per unit volume, is given to a good approximation by

$$1.42 \times 10^{-27} Z^2 T_e^{1/2} g_{ff} N_e N_{X+z}. \quad (13)$$

The large abundance of hydrogen and helium ensures that their contribution to free-free cooling is the most important one.

A modification of the heating-cooling rate is required in cases of significant free-free optical depth, since some of the radiation is re-absorbed and heating by the diffuse free-free radiation was not included. An approximate way to introduce the correction is to multiply the cooling rate by the factor $\exp(-h\nu_{cut} / kT_e)$, where ν_{cut} is the depth dependent frequency, where the gas becomes optically thin to free-free absorption.

4.2.3. Collisional excitation and de-excitation heating-cooling. Inelastic collisions of free electrons with ions, followed by a radiative decay, convert kinetic energy into excitation energy and contribute to the cooling of the gas. Collisional de-excitation returns energy to the electron gas and is thus a heating process. It is convenient to discuss the net cooling, which is the cooling minus heating, per unit volume and time.

Consider the two level system, i and j ($j > i$), with statistical weights g_i and g_j respectively. The levels are coupled by an optically thin line, of energy E_{ij} and a radiative transition rate A_{ji}. The collisional excitation rate between the levels is

$$C_{ij} = \frac{8.629 \times 10^{-6} N_e \Omega_{ij}}{g_i T_e^{1/2}} \exp(-E_{ij}/kT_e), \tag{14}$$

and the collisional de-excitation rate

$$C_{ji} = \frac{g_i}{g_j} \exp(E_{ij}/kT_e) C_{ij}, \tag{15}$$

where Ω_{ij} is the effective, temperature averaged, collision strength. In the absence of other populating mechanisms, the relative population of the levels is

$$\frac{N_j}{N_i} = \frac{C_{ij}}{(C_{ji} = A_{ji})}. \tag{16}$$

A useful concept is the so called "critical density", which is obtained for each transition by solving for the electron density for which $C_{ji} = A_{ji}$. Collisional de-excitation can be neglected for densities much smaller than this critical density, while the Boltzmann excitation equation can replace (16) for densities much above it.

The net cooling is the energy emitted by the atoms per unit volume and time

$$E_{ij} A_{ji} N_j. \tag{17}$$

In the limit of low density this is reduced to

$$E_{ij} N_i C_{ij}. \tag{18}$$

Thus, in this limit, the net cooling is proportional to N_e^2. In the high density limit $N_j \propto N_i$ and the net cooling is proportional to the gas density. Since the net cooling is basically the line emission, this is also the density dependence of the emergent line flux.

The formalism used here is easily generalized to a multi-level system and to the case where other atomic processes contribute to the level populations.

The steady state electron temperature is obtained by solving the simple energy conservation equation

$$\sum Heating = \sum Cooling. \tag{19}$$

This requires the full solution of the statistical equilibrium equations at all points in the cloud. The ionization and thermal solutions are of course coupled and iterative methods must be used to solve them, simultaneously.

---

[2] see however the note below about secondary electrons. Back.

4.3. Additional Heating and Ionization Processes

The following are additional processes that are likely to be important in AGN clouds.

4.3.1. Dielectronic recombination. Radiative recombination is the term used to describe the interaction of the ion X^{i+1} with a free electron, leading to the ion X^i in a ground or excited state *below* the ionization limit. Recombination can also proceed via autoionization states, *above* the ionization limit, in which case it is called dielectronic recombination. At high temperatures the free electrons cover an infinite number of autoionization states. Dielectronic recombination, in this case, is fast but density dependent. At low temperatures individual autoionization states are the main contributors to the recombination rate. The process

is important in AGN clouds and can also result in emission lines of ion X^i. Such lines are weak but are of great importance in determining the chemical composition of the gas.

4.3.2. Collisional ionization and three-body recombination. The rates of collisional ionization and its inverse process, three-body recombination, depend on N_e^2, T_e, and the statistical weight of the level in question. Such processes are not very important in photoionized galactic nebulae, where the density is low and most ions are in their ground state. This is not the case in the broad line clouds, where many atoms are in excited states, due to the high density and large optical depth. For example, in the BLR clouds, the $n \geq 10$ levels of hydrogen, helium and some metals are collisionally coupled to the continuum and their populations are completely controlled by such processes. The $n < 10$ levels of hydrogen are affected too.

The treatment of these processes is rather tricky. A very large number of levels must be considered, and many unknown cross sections must be guessed. As a general rule, three-body recombination is faster than radiative recombination, for many ions, at $N_e \geq 10^{11}\ cm^{-3}$. The process is therefore important in the very dense parts of the BLR.

4.3.3. Compton heating-cooling and ionization. Compton scattering by bound and free electrons can be an important ionization and heating source for the gas, because of the intense X-ray radiation in AGNs. For nonrelativistic electrons, the energy transfer per scattering is approximately

$$\frac{h\nu}{m_e c^2}(4kT_e - h\nu), \tag{20}$$

thus photons with energies greater than about 2.6 keV can ionize hydrogen from its ground level. Heavier elements can be ionized too, at higher energies, with an effective cross section which is proportional to the number of bound electrons. In realistic situations, the process is important only for mostly neutral gas, and hydrogen ionization is the only important source of free electrons because of the small abundance of the heavier elements.

The Compton heating rate is

$$\frac{N_e}{m_e c^2}\int_{\nu_0}^{\infty}\frac{L_\nu \sigma_h h\nu}{4\pi r^2}d\nu. \tag{21}$$

Compton cooling ("inverse Compton") occurs when a low energy photon, ($h\nu < 4kT_e$) is scattered by an electron. The cooling rate is

$$\frac{4kT_e N_e}{m_e c^2}\int_{\nu_0}^{\infty}\frac{L_\nu \sigma_c}{4\pi r^2}d\nu. \tag{22}$$

In these expressions σ_h and σ_c are heating and cooling effective cross sections that agree with the Thomson cross section at low photon energy and with the Klein-Nishina formula at $h\nu \sim m_e c^2$. The correction due to stimulated processes, that can be important in intense radiation fields, was not included in these equations.

Compton heating and cooling is most important for the (hypothetical) hot gas suggested as a confining medium for AGN clouds (chapter 9).

4.3.4 Secondary electrons. Photoionization by high energy photons results in the ejection of an energetic electron. Because of the smaller Coulomb-scattering cross section at high energies, the mean free path of such electrons is long and several other reactions can occur before thermalization takes place. Most important are collisional ionization (leading to more secondary electrons) and collisional excitation. The result is more ionizations and less heating per incident high energy photon. The process is well known in the interstellar medium.

Secondary electrons related processes are very important in the partly neutral zone of AGN broad line clouds. The fast electrons are produced mainly by photoionization of He^0 and some metals, and they loose much of their energy by collisional excitation and collisional ionization of hydrogen. Calculations giving the number of extra ionizations, and the effective heating due to such electrons, are available. Care must be taken in calculating the cooling rate since excitation to high levels may be followed by collisional de-excitation, i.e. additional heating. There is also some extra line emission due to this process.

4.3.5 Charge exchange. These are reactions of the type

$$X + Y^+ \rightleftharpoons X^+ + Y, \tag{23}$$

where X and Y are two ions. The most important cases at $T_e \sim 10^4$ K, involve neutral hydrogen. Well known examples are charge exchange reactions of H^0 with O^+ and N^+, that control the ionization of oxygen and nitrogen near the hydrogen ionization front.

Atomic calculations show that charge exchange with hydrogen, at a rate of 10^{-9} cm^{+3} s^{-1} or larger, is common for many ions. The typical recombination coefficients for metals, at $T_e = 10^4$ K, are about 10^{-12} cm^{+3} s^{-1}, and charge exchange with hydrogen is therefore an important process for all regions where $N(H^0) / N(H^+) \geq 10^{-3}$. For example, the charge exchange of H^0 with Fe^{++} is an important factor in increasing the Fe^+ fraction in AGN clouds.

Charge exchange can proceed via excited states, leading to some line emission. There is not yet any clear evidence that this is important in AGN clouds.

4.3.6 H^- and molecules. In large column density clouds, a trace amount of hydrogen can be in the form of H^- and H_2. This can be an important opacity source at infrared frequencies that increases the amount of infrared heating. The expected amount of H^- and H_2 must therefore be considered.

An important creation mechanism for H^- is collisions with free electrons

$$H^0 + e \rightleftharpoons H^- + h\nu. \tag{24}$$

Several other processes, such as charge exchange of H^- with positively charged ions (*charge neutralization*), can be important too. Out of the possible heating-cooling processes applicable to H^- and H_2, those associated with bound-free and free-free transitions in H^- are probably the most important.

The H^- and H_2 related processes are of marginal importance in AGN clouds, unless the column density is extremely large (~ 10^{25} cm^{-2}).

4.4. Radiative Transfer

The photoionization calculations described above are relatively straight forward, provided the internally produced radiation can freely escape the cloud. This is the case in most galactic nebulae, and possibly also in AGN NLR clouds, but not in the BLR, where the optical depth to line and continuum radiation is significant. In this case the calculations must be modified, and the following pages describe some commonly used ways to do so.

4.4.1 Continuum transfer. The internally produced recombination (bound-free) radiation can have a large effect on the degree of ionization by interacting with the gas far from its point of creation. Sophisticated, iterative methods have been developed to account for the propagation of this radiation in the cloud. They depend on the gas distribution and geometry and cannot be applied, in a simple way, to all configurations.

Approximate methods have been developed too, to shorten the calculations and reduce the number of iterations. The "on-the-spot" approximation is based on the assumption that the diffuse radiation is absorbed very close to its point of creation. This is normally a good assumption for the ground level recombination of helium and hydrogen, in nebulae that are very optically thick to the Lyman ionizing radiation. In this case the mean free path of the ground level recombination radiation is very short, and the assumption of local absorption works very well. The approximation is easy to apply since all that is required is to omit recombination to the ground level from the total recombination coefficient in the ionization (3) and thermal equilibrium (10) equations. The method cannot be used for treating recombination to excited levels, where the mean free path of the bound-free radiation is of the order of the cloud size or larger. It also fails near the boundaries of the cloud, where the optical depth to the surface is short even for the ground level recombination radiation.

There are ways to improve this simplified treatment. In the "modified on-the-spot" approximation, a correction factor is applied to each of the recombination coefficients, depending on the optical depth to the surface at the relevant frequency. The

application is particularly simple in a slab geometry, where the radiation can be divided into inward going and outward going beams, and only optical depths to two surfaces need to be computed. For example, the recombination coefficient for hydrogen in equation (3), at a point inside the cloud where the Lyman continuum optical depth to the inner (illuminated) side is τ_{in} and to the outer side is τ_{out}, can be written in the following way:

$$H^- + H^0 \rightleftharpoons H_2 + e, \tag{25}$$

where α_1 is the recombination coefficient to n = 1 and α_B is the sum of all recombination coefficients to levels with n > 1. The factor a_1, which is of the order of 2, takes into account the oblique escape of the ground level recombination photons and the frequency dependence of the optical depth. A modification of α_2, α_3 etc. can be included in a similar way. Here the frequency dependence of the optical depth must be calculated with great care, which means that a_1 is a strong function of the location in the cloud.

In a second approximation, named "outward only", the locally produced diffuse radiation is added to the incident flux and carried into the cloud in one, or more directions. Its obvious limitations is near the illuminated surface, where no diffuse radiation is allowed to escape. The process puts much of the heat deep in the cloud, causing an unrealistic temperature structure.

The free-free optical depth is never very large and the above approximate transfer methods are not adequate in this case. In many cases the optical depth is so small that no correction term is required. In other cases the free-free optical depth, τ(ff) must be calculated at all frequencies and included in the free-free heating integral (11). The free-free cooling rate is then modified using the exp(-hν_{cut} / kT_e) factor mentioned in 4.2.2. This local treatment is only a first order approximation to the rather complex full treatment of the free-free radiation transfer.

4.4.2 Line transfer. Standard radiative transfer techniques require a numerical solution of the radiation field everywhere in the gas. Each individual line profile is divided into several frequency bins, and the redistribution in frequency, following an absorption-emission process, is taken into account at all points. This is successfully applied in stellar atmosphere calculations, where conditions are close to LTE. Under such conditions, the local temperature and the level populations are not very sensitive to the emitted line flux and good solutions are obtained even when a small number of transitions are considered.

This is not the case in gaseous nebulae, where conditions are far from LTE, and a complete solution of the statistical equilibrium equations is required in order to calculate the temperature. Realistic photoionization calculations for AGN clouds involved the computation of several hundred emission lines, the large majority of which are optically thick. Neglecting some lines in the energy balance calculations, for the sake of treating the transfer of others in a more complete way, may result in a poor estimate of the kinetic temperature and wrong line ratios. Combining the two types of treatments, by solving the full radiative transfer in all lines, is beyond the capability of the most sophisticated computer codes available. We are thus faced with the choice of treating the radiative transfer in detail, at the expense of the atomic physics, or vice versa.

The alternative, so far preferred in most advanced calculations, is to treat the atomic physics in the most accurate way and use a simplified method for the line transfer. The method is known as *the escape probability method* and is demonstrated here for the simple case of a two level atom.

Consider a two level atom with an energy separation between the levels of E_{12} and a normalized line profile Ψ_ν, which is assumed to be identical for both absorption and emission. Let I_ν be the radiation intensity and J the intensity averaged over angles and frequencies

$$J = \frac{1}{4\pi} \int \int I_\nu \Phi_\nu d\nu d\Omega. \tag{28}$$

Consider only radiative processes; spontaneous emission, with a rate of $n_2 A_{21}$, absorption, with a rate of $n_1 B_{12} J$ and induced emission, with a rate of $n_2 B_{21} J$. The rate equation for the level population is:

$$\frac{dn_2}{dt} = -\frac{dn_1}{dt} = -n_2 A_{21} - J(n_2 B_{21} - n_1 B_{12}). \tag{29}$$

For isotropic line emission the emission coefficient is:

$$\varepsilon_\nu = \frac{1}{4\pi} n_2 A_{21} h\nu_{12} \Phi_\nu \tag{30}$$

and the absorption coefficient is:

$$\kappa_\nu = \frac{1}{4\pi}(n_1 B_{12} - n_2 B_{21}) h\nu_{12} \Phi_\nu, \tag{31}$$

where stimulated emission is counted as negative absorption. The line source function, S_ν, is therefore

$$S_\nu = \frac{A_{21} n_2}{B_{12} n_1 - B_{21} n_2} = \frac{2h\nu^3}{c^2} \frac{1}{(n_1 g_2 / n_2 g_1) - 1}, \tag{32}$$

where we have made use of the fact that $A_{21} = (2h\,\nu^3 / c^2) B_{21}$ and $g_1 B_{12} = g_2 B_{21}$.

Let β_{21} be the probability of a line photon to escape the cloud and (1 - β_{21}) the probability to be trapped. In the escape probability method we assume that

$$J = S(1 - \beta_{21}), \tag{33}$$

which, by using the definition of S (32) and substituting into the rate equation (29), simplifies to

$$\frac{dn_2}{dt} = -\beta_{21} A_{21} n_2. \tag{34}$$

In the same way the emergent line flux, per unit volume, is:

$$\beta_{21} A_{21} n_2 h\nu_{12}. \tag{35}$$

This is the essence of the escape probability method. It shows that the equations are similar to the optically thin case except that an *effective Einstein coefficient*, $\beta_{21} A_{21}$, replaces A_{21}. The method ensures local energy conservation and the local temperature is well determined. The scheme is easily generalized to a many level atom, by replacing A_{ji} for each transition, by $\beta_{ji} A_{ji}$.

The escape probability approximation gives a correct solution where all scatterings are local and there is little diffusion in space (i.e. the photon is scattered many times close to its point of creation and then escapes the cloud without any further interaction). It is also formally correct for the uniform case, where the temperature and degree of ionization are the same throughout the clouds. In such cases β is a "mean escape probability" which is a function of the total cloud optical depth.

Most realistic nebulae are not uniform throughout. Moreover, the line scattering process cannot be entirely local and some diffusion in space must occur. Thus the escape probability describing the trapping of the radiation, in the statistical equilibrium equation (34), is not necessarily the same function needed for calculating the emergent flux (35). Despite this, the advantage of this technique, especially the ability to treat hundreds of optically thick transitions simultaneously, is so great that it is currently being used in many photoionization calculations. The emphasis so far has been on getting reliable estimates of β for different line profiles and cloud geometries.

The scattering of resonance line photons is a well studied problem and various excellent calculations are available to estimate it under a variety of conditions. The number of scattering depends on the geometry, the optical depth and the line profile (or more accurately, the "redistribution function"). A general result of such calculations is that the scattering of line photons is mostly local (i.e. little diffusion in space) if the re-emitted photon is in the core of the line, within 3 Doppler widths of the line center. Such photons escape the cloud by diffusion into the line wings where scattering is coherent and a small number of scattering carry the photon a large distance in space. It means that the "local scattering" assumption, used in the escape probability approximation, is quite adequate for all resonance lines whose optical depth does not exceed about 10^4 (the optical depth corresponding to 3 Doppler widths).

The main result of the numerical transfer calculations mentioned above is expressed as the number of scatterings before escape, $Q(\tau)$. This is related to β via

$$\beta(\tau) = \frac{1}{1+Q(\tau)}. \tag{36}$$

It is usually found that the number of scatterings is roughly linear with the *line center* optical depth, calculated from

$$d\tau_{12} = \frac{0.015 f_{12}\lambda_{12}}{v_{\rm Doppler}}(n_1 - g_1 n_2/g_2)ds, \tag{37}$$

where f_{12} is the oscillator strength and $v_{\rm Doppler}$ is the line Doppler width. [(3)] Thus

$$\beta = \frac{1}{1+k(\tau)\tau}, \tag{38}$$

where $k(\tau)$ is a weak function of τ and is of the order of 2-5.

The total path length traveled by the photon before escape is also proportional to τ, with a different dependence factor, $k'(\tau)$. Numerical calculations show that $k'(\tau) \simeq k(\tau)$, i.e. the time it takes optically thick line photons to escape the cloud is several times longer than the time it takes the optically thin photons. This is important for dynamical reasons, since the trapped line radiation increases the internal pressure in the cloud (see chapter 9). The implication is that the radiation pressure in optically thick lines is enhanced by a factor of ~ 5, almost regardless of the optical depths.

The method most commonly applied in modeling the broad line clouds is the "local escape probability", whereby the escape probability at each point is a function of the optical depth at that location. Thus, in a slab model, at a point in the cloud where the line center optical depth to one surface is τ and to the other surface is ($\tau_{\rm tot}$ - τ), the local escape probability is:

$$\beta(\tau_{\rm tot},\tau) = \frac{\beta(\tau)+\beta(\tau_{\rm tot}-\tau)}{2} \tag{39}$$

Obviously, $\tau_{\rm tot}$ is not known a-priori and two or more iterations are required for a complete convergence of the calculations.

The following expressions for β are similar to what is used in most current calculations:

a. For $L\alpha$, $HeI\lambda$10830 and most resonance lines a good approximation is

$$\beta = \frac{1}{1+2\tau}, \tag{40}$$

b. For all other hydrogen lines, and non-resonance transitions

$$\beta = \frac{1}{1+2\tau} + \frac{0.25a^{1/2}}{\tau^{1/2}}, \tag{41}$$

where a is the damping constant for the line. The notable difference from the resonance line case is the dependence on $\tau^{-1/2}$ at large (~ 5000) optical depths. This different functional form is a question of some debate and is of great significance for lines like $H\alpha$.

c. Stark broadening of the upper levels of some transitions, changes the escape probability at high densities. Some calculations of the modified β are available for hydrogen. They must be incorporated in the calculations for $N_e >> 10^{10}$

cm^{-3}.

4.4.3 Line and continuum fluorescence. Wavelength coincidences between emission lines ("line fluorescence") can be an important source of radiative excitation. The best known examples are the *HeII - OIII* Bowen Fluorescence, at a wavelength of about 304Å, and the OI-Lβ fluorescence at 1025Å. The first involves the excitation of OIII lines by the absorption of HeII $L\alpha$ photons. It is important in both the NLR and the BLR clouds, as indicated by the observed OIII Bowen lines, at wavelengths around 3000Å. The second is illustrated in Fig. 6 and results in extra excitation of the OI $^3D^0$ level by the hydrogen Lβ line. It is very important in the BLR, where the scattering of the $H\alpha$ photons increases the $L\beta$ radiation intensity in the part of the cloud where the $H\alpha$ optical depth is large. Observable lines that are enhanced by this process are $OI\lambda 1302$ and $OI\lambda 8446$ (se diagram).

Wavelength coincidences among FeII lines can be important too. There are *several hundred* such coincidences and some may be more important than others. Another interesting possibility is a wavelength coincidence between $L\alpha$, which has a broad profile due to its large optical depth, and several FeII lines. Other possibilities that have been mentioned involved $MgII\lambda 2798$, $NV\lambda 124O$ and more.

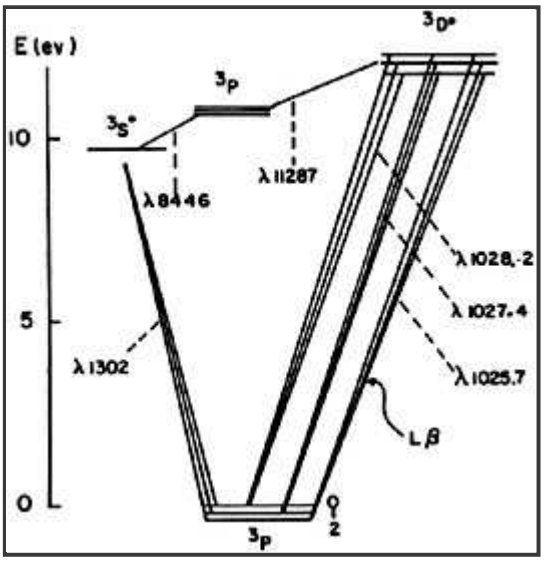

Figure 6. The energy level diagram of *OI* showing the possible fluorescence with $L\beta$. Observable lines that are mostly affected are at $\lambda 1302$ and $\lambda 8446$. The process is most important in regions of large $H\alpha$ optical depth.

Accurate treatment of line fluorescence requires a complete transfer calculation. There is also a local, less accurate solution, based on the escape probability method, that is simple to use and easy to incorporate into the statistical equilibrium equations. It involves the assumption of rectangular line profiles, (or more accurately a constant source function across the line profile), and gives quite good results. Its main disadvantage is the local treatment and the poor approximation at the line wings, where the source function is not constant.

Line fluorescence in AGNs has been a source of some confusion. Such processes are efficient in removing line photons from one transition, and pumping them into another, at frequencies where the radiation field is most intense, i.e. close enough to the line center for the source function to be constant. Further out into the line wings the source function is smaller and the pumping efficiency reduced. A separation of only a few Doppler widths between lines, can result in almost a zero fluorescence efficiency. This is the case even in very large optical depth lines, such as $L\alpha$, where the line profile is many Doppler widths wide.

Line photons can be destroyed by continuum absorption processes. This is sometimes called "continuum fluorescence" and is particularly important for optically thick lines, where the effective absorption optical depth is increased by the increased path length of the photons (see the $k'(\tau)$ factor mentioned earlier). Important examples are the ionization of hydrogen $n = 1$ by resonance lines with $\lambda < 912$Å, the ionization of hydrogen from the $n = 2$ and $n = 3$ levels by $L\alpha$, $MgII\lambda 2798$, $H\alpha$ and *FeII* lines, and the ionization of neutral helium from the 2^1S and 2^3P levels. Absorption by dust grains, that are mixed in with the gas, and by H^-, are other examples.

The escape probability method provides a simple local treatment for this situation. Consider again the two level atom, a line absorption cross sections of κ_l and a continuum absorption cross section, at the line frequency, κ_c. Define

$$X_l = \frac{\kappa_l}{\kappa_l + \kappa_c}; \; X_c = \frac{\kappa_c}{\kappa_l + \kappa_c}, \tag{42}$$

and

$$\beta_{lc} = \beta(\tau_l + \tau_c). \tag{43}$$

The escape probability formalism suggests that in the presence of a continuum opacity source, an effective escape probability

$$\beta_{\rm eff} = X_c + X_l \beta_{lc}, \tag{44}$$

is to replace β_{21} in the statistical equilibrium equation (34). In this case, the emergent line flux, per unit volume, is

$$n_2 A_{21} \beta_{lc} h\nu_{21}, \tag{45}$$

and the number of continuum absorptions (e.g. photoionizations) is

$$n_2 A_{21} X_c (1 - \beta_{lc}). \tag{46}$$

This treatment is local and does not take into account the absorption of line photons away from their point of creation. A possible way to improve it, in cases of large continuum optical depth, is to multiply Eqn. (45) by exp(-τ_c), where τ_c is a typical continuum optical depth, e.g. toward the inner surface of the cloud. The extra amount of continuum absorption should then be added to the expression in (46). This is not the only way to treat the continuum absorption process, and other, rather different methods, have also been suggested.

Absorption of external continuum radiation by spectral lines can be computed with the same formalism. Consider a point in the cloud where the optical depth to the illuminated surface, in a certain line, is $\tau_{\rm in}$. The probability of a photon emitted towards the continuum source to escape is $\beta(\tau_{\rm in})$, which is also the probability of the external radiation to reach that point in the cloud. The local *J* (33) is thus increased by an amount corresponding to the unattenuated external flux multiplied by $\beta(\tau_{\rm in})$. In the case of a central point source with luminosity L_τ, the increase in *J* is

$$\beta(\tau_{\rm in}) L_\nu / 16\pi^2 r^2, \tag{47}$$

and the rate equation, omitting collisional and ionization processes, takes the form

$$\frac{dn_2}{dt} = -\beta_{21} A_{21} n_2 - \beta(\tau_{\rm in}) A_{21} \frac{c^2}{2h\nu^3} \frac{L_\nu}{16\pi^2 r^2} (n_2 - g_2 n_1 / g_1)], \tag{48}$$

where β_{21} is the two-directional escape probability of equation (33). The process is important in cases of large ionization parameter. It can become significant in the partly neutral zone, where continuum absorption in spectral lines is immediately followed by collisional ionization from an excited state.

---

[3] A component of microturbulence has been suggested to increase the line width and to reduce the optical depth. These are not considered here. We also do not consider velocity gradient (e.g. expansion) inside the clouds, that require a different escape probability function. Back.

4.5. The Emergent Spectrum

4.5.1. Input parameters. A complete model for an isolated cloud requires that the following parameters be defined:

a. The frequency dependence of the incident continuum, L_ν.
b. The gas density (or pressure) and column density, N_{col}.
c. The gas chemical composition.
d. The geometrical shape of the cloud.
e. The ionization parameter, U.

The incident continuum is known over a large range of frequencies. Unfortunately, the most important part, the Lyman continuum up to the soft X-ray energies, is not observed except in some high redshift quasars. This is a major drawback and indirect methods (chapter 10) must be used to estimate L_ν in that gap. Another uncertainty is the high energy tail ($h\nu$ > 30 keV) which is not yet observed in many AGNs. This has important implications in models of large N_{col}. Finally, free-free absorption at low frequencies may be a significant heating source for the BLR, but it is not at all clear that the observed far infrared radiation originates in a small, point-like continuum source (see R. Blandford's contribution), If this radiation comes from an extended disk, or any other structure large in comparison with the BLR size, then its effect on the broad line gas, via free-free heating, is largely reduced.

Fig. 7 shows a typical continuum which is used in photoionization calculations and is consistent with our knowledge of many radio quiet AGNs. The characteristic features are the steep infrared (1 - 3μm) slope (a spectral index of about 1.5), the flattening at optical and ultraviolet wavelengths, sometimes referred to as "the big blue bump", the cutoff at about 3-10 Ryd (implied by the models but not directly observed) and the flat X-ray continuum. The drop at λ > 30μm is artificially introduced, because of the above mentioned uncertainty about the origin of this component.

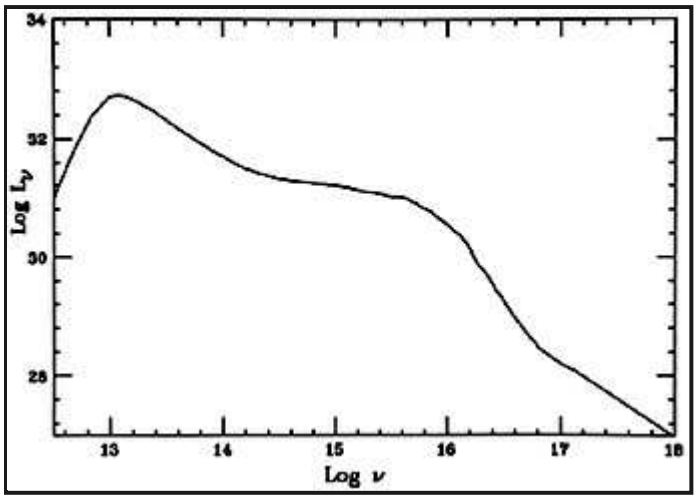

Figure 7. A characteristic AGN continuum.

The gas density can be measured, or at least estimated, from the observed spectrum. Standard methods of nebular analysis, involving the relative strength of several forbidden lines, suggest that $N_e \leq 10^8$ cm^{-3} in all the NLR clouds, with a typical density of about 10^4 cm^{-3}. The density of the BLR clouds is more difficult to estimate. The absence of strong broad forbidden lines of [*OIII*]λ5007 indicates that collisional de-excitation takes place, and therefore $N_e \geq 10^8$ cm^{-3}. On the other hand, the strong intercombination lines of *CIII*]λ1909, *NIII*]λ1750, *NIV*]λ1486 and *OIII*]λ1663 suggest $N_e \leq 10^{12}$ cm^{-3}. Detailed calculations confirm these limits.

It is customary to fix either the density or the pressure at the illuminated face of the cloud, and proceed by assuming constant density, constant pressure, or some other assumption. This depends, of course, on conditions outside the cloud. For example, in the "two phase model" (chapter 9) the BLR clouds are embedded in a hot (~ 10^8 K) intercloud gas that provides the external confining pressure. Constant pressure models are appropriate in this case. On the other hand, the cloud internal pressure, near a variable continuum source, varies in time following the changes in T_e, N_e and the line radiation pressure. Since the sound crossing time (chapter 9) of the BLR clouds is comparable to the variability time of the central radiation source, a stable pressure equilibrium may never be achieved. Constant density models may be more appropriate in this case. Finally, if AGN

clouds are stellar atmospheres or the outer parts of accretion disks (chapter 9), then their the structure is controlled by the local gravity.

The lower limit on the column density of the BLR clouds is of the order of 10^{22} cm^{-2}. This is derived from the presence of strong low excitation lines of MgII and FeII. Some clouds of much larger N_{col} are likely to exist, as deduced from the frequently observed lines of *CaII*, but a general upper limit is difficult to establish. Obviously, N_{col} is not necessarily the same in all clouds and in all objects. The column density of typical NLR clouds is not well known but it is estimated to be smaller than the BLR column density.

The chemical composition of AGN clouds is difficult to measure because of the nonstellar continuum shape, which results in a mixing of several stages of ionizations in one zone. In the BLR it is possible to use some observed line ratios, that do not depend much on the temperature and the ionization parameter, to estimate the composition. An example is the *NIV*]λ1486 / *CIV*λ1549 ratio which is a good C/N abundance indicator. The abundances relative to hydrogen are ill determined because of the uncertainty in the calculated intensity of the hydrogen lines. There is a similar difficulty in the NLR, due to the difficulty in determining the electron density and temperature from optical forbidden lines. The hope is to use ultraviolet HST measurement of dielectronic recombination lines, and to combine them with collisionally excited lines, to determine the temperature. Thus the line pair (*CII*λ1335, *CIII*]λ1909), can be used to measure T_e in the C^{++} zone. This temperature, combined with the measured intensity of *NIII*]λ1750 that comes from the same region, will enable us to directly measure the C/N abundance ratio.

The comparison of observations of many line ratios with the best model calculations suggest that the following *cosmic abundances* (Table 2) are within a factor 2 of the abundances in many AGNs.

Table 2. Cosmic abundances used in AGN models

Element	N/N(H)
helium	0.1
carbon	3.7×10^{-4}
nitrogen	1.2×10^{-4}
oxygen	6.8×10^{-4}
neon	1.0×10^{-4}
magnesium	3.3×10^{-5}
aluminum	2.5×10^{-6}
silicon	3.2×10^{-5}
sulphur	1.6×10^{-5}
argon	3.8×10^{-6}
calcium	2.0×10^{-6}
iron	2.6×10^{-5}

The shape of the clouds is important because it determines the escape of line and continuum photons. The escape probability function in a sphere is different from that in a slab and there are "skin effects" to be considered. An *infinite slab* model has been adopted in many cases and will be used here. Later (chapter 5) we consider spherical BLR clouds but retain the slab escape probability function. This is well within the general limitation and uncertainty of using such transfer methods.

Finally, the value of the ionization parameter has to be determined (alternatively, the cloud distance and L_ν at some frequency). This is often used as the variable parameter in the calculations.

4.5.2 Examples. Fig. 8 shows calculated line fluxes, as a function of the ionization parameter, for an isolated BLR cloud. The input continuum is the one shown in Fig.7, the density is constant at 10^{10} cm^{-3}, the column density is 10^{23} cm^{-2} and the composition is as in Table 2. The line intensities are given relative to $H\beta$. Calculations for an isolated NLR cloud, with the same continuum source and abundances and $N = 10^4$ cm^{-3}, are shown in Fig. 9. In this case the calculations stop at $\tau_{912} = 10^{3.5}$.

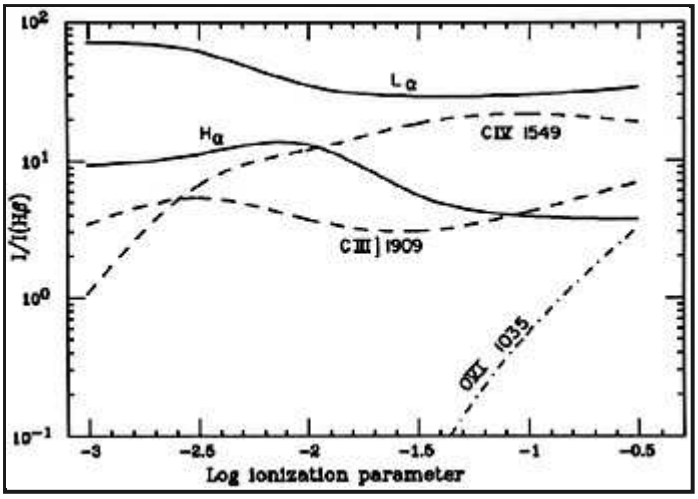

Figure 8. Broad line ratios, relative to $H\beta$, as a function of the ionization parameter.

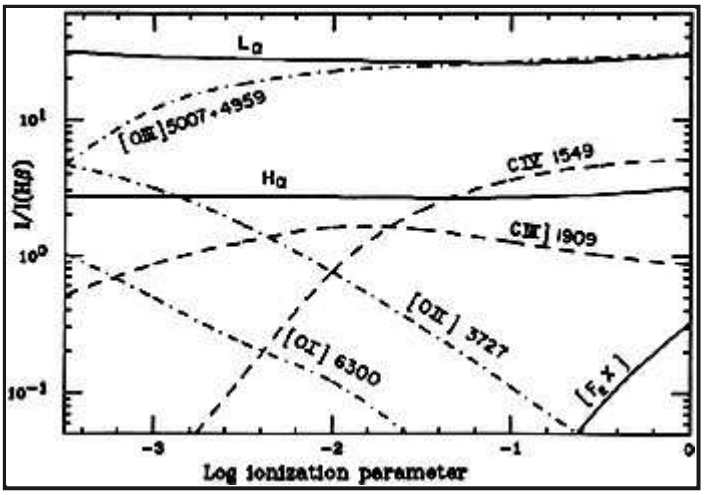

Figure 9. Narrow line ratios, relative to $H\beta$, as a function of the ionization parameter.

As evident from the diagrams, some line ratios are good ionization parameter indicators. In the BLR model, this is $OVI\lambda 1035$ / $CIV\lambda 1549$; in the NLR model $[OII]\lambda 3727$ / $[OIII]\lambda 5007$. The $CIII]\lambda 1909$ / $CIV\lambda 1549$ ratio, that was thought to be a gooc ionization parameter indicator for the BLR, is not so, because of the big changes in the ionization structure at large U that limit the extent of the C^{+++} zone. The low excitation lines of MgII and FeII (not shown here) depend on U in a very complicated way and are not good ionization parameter indicators. They are further discussed in chapter 6.

The observed intensities of the broad high excitation lines (Table 1) suggest that the typical ionization parameter for the BLR is at least 0.1, if all lines are to be produced in the same population of clouds. There are, however, other ways to produce strong, high excitation lines, such as optically thin material. A typical ionization parameter for the NLR is about 0.01, but there is a large diversity in this value, as discussed in chapter 11. The observed strength of $[FeX]\lambda 6734$ and other narrow $[FeX]$ and $[FeXI]$ lines presents a problem, since such lines are calculated to be too weak in clouds with the ionization parameter required to give the observed $[OII]\lambda 3727$ / $[OIII]\lambda 5007$ ratio. The origin of these lines may be some transition zone between the BLR and the NLR, or perhaps the interstellar matter of the host galaxy.

Regarding the broad hydrogen lines, the calculated change in $L\alpha$ / $H\alpha$ / $H\beta$ is mainly due to the increase of the Balmer optical depth with U. This is related to a well known problem of AGN study to be discussed in chapter 6. Finally, the diffuse bound-free and free-free continua, emitted by one of the broad line clouds considered here, are shown in Fig. 10.

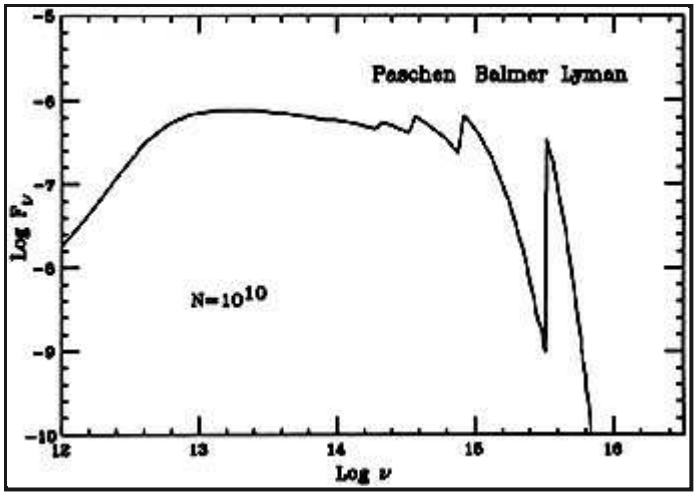

Figure 10. Diffuse continua emitted by a broad line cloud with $U = 0.3$ and all other parameters as specified in the text.

The next step involves the combination of many one-cloud models in order to compare them with observed AGN spectra. This requires some knowledge of the gas distribution and is discussed in the following chapter.

4.6. Bibliography

There are several excellent books on physical processes in low density nebulae. The most recent one is by Osterbrook (1989), where high density processes in AGNs are also described. A complete description of atomic processes is given in Mihalas (1978). Comprehensive discussions of radiative transfer methods are given in a book edited by Kalkofen (1984, see Canfield et el. there for application to AGNs) and in a soon to be published book on Masers by Elitzur. Many of the theoretical aspects dealt with in this chapter have been discussed in several review papers, where a more complete lists of references can also be found. The situation prior to 1979 is summarized by Davidson and Netzer (1979). Later, exhaustive reviews are by Kwan and Krolik (1981), Ferland and Shields (1985) and Osterbrock and Mathews (1986). Some detailed papers, on more specific topics, are:

X-ray related processes: Halpern and Steiner (1983), Kallman and McCray (1982), Shull and Van Steenberg (1985, heating and ionization by secondary electrons) and Ferland and Rees (1988).

Chemical composition: Shields (1976, broad lines, C/N and O/C), Uomoto (1984), Gaskell et al. (1981, metal deficiency in dusty BLRs), Wills, Netzer and Wills (1985, iron abundance), Binnette (1985, narrow lines in LINERs).

H^- and molecules: The most recent and complete paper is by Ferland and Persson (1989), where references to earlier papers are given.

Very high densities: See Ferland and Rees (1988) and Rees, Netzer and Ferland (1989).

Continuum transfer: See Netzer and Ferland (1984) and references therein for a modified on-the-spot approximation. See Collin-Souffrin and Dumont (1989) for treatment of hydrogen $n > 1$ levels. Puetter and Hubbard (1985) describe the formal solution of the free-free radiation transfer.

The escape probability method: The basic formalism is given by Elitzur (1984). The local escape probability is discussed in Kwan and Krolik (1981), and in many later papers. Useful approximations for β and more references can be found in Rees, Netzer and Ferland (1989). For Stark broadening see Puetter (1981). Continuum destruction is discussed in Netzer et al. (1985). Their treatment is however different from the one suggested by Hummer (1968) and at this stage it is not clear which is more applicable to AGN clouds. Puetter and collaborators (see references in Hubbard and Puetter 1985) discussed various aspects of the escape probability method, as well as some more complete transfer methods, as applied to AGN clouds. Most of their calculations are for a pure hydrogen case. A similar approach, including more elements, is described in Collin-Souffrin and Dumont (1986), where earlier references to such work can be found. Avrett and Loeser (1988) described an attempt to perform a complete transfer calculation for some lines, combined with a simplified treatment for many others. Numerical calculation of the scattering of resonance line photons, and references to earlier papers on the subject, can be found in Hummer and Kunasz (1980).

Line and continuum fluorescence: For the escape probability approximation of this process see Elitzur and Netzer (1984, lines), Netzer, Elitzur and Ferland (1985, line and continuum) and Lockett and Elitzur (1989, a critical discussion of the escape probability approximation). A more complete transfer approach to this problem is described by Weymann and Williams (1969) and Eastman and MacAlpine (1985). Line fluorescence in FeII is described in Netzer and Wills (1983), Wills, Netzer and Wills (1985) and Elitzur and Netzer (1984). For fluorescence with $L\alpha$ see Penston (1987).

Complete photoionization calculations: There are quite a few of these, starting from the works of Davidson (1972) and MacAlpine (1972). Some recent ones are: Kwan (1984, BLR, dependences on density and ionization parameter), Mushotzky and Ferland (1984, BLR, dependence on ionization parameter), Netzer, Elitzur and Ferland (1985, BLR and NLR), Ferland and Osterbrock (1986, NLR), Netzer (1987, BLR, continuum shape, angle dependence and large ionization parameter), Krolik and Kallman (1988, continuum shape), Rees, Netzer and Ferland (1989, BLR, including very high densities), Ferland and Persson (1989, BLR, large ionization parameters and extreme column densities), Collin-Souffrin and Dumont (1990) and Dumont and Collin-Souffrin (1990, very low ionization parameter and high densities) and Korista and Ferland (1989, interstellar high ionization lines).

5. Photoionization Models for a System of Clouds

Having calculated the emergent spectrum of isolated clouds, we now consider the gas distribution and the different ways to combine the emission from such clouds into a composite spectrum.

5.1. Spherical BLR Models

Consider a spherically symmetric system of clouds, extending from r_{in} to r_{out}. The mass of the individual clouds is conserved, but it is not necessarily the same for all clouds. The following physical parameters are all functions of r: the cloud number density $n_c(r)$, the cloud particle density N, the cloud emissivity $j_c(r)$, and the cloud velocity $v(r)$.

Most cases of interest involve optically thick clouds, where energy conservation requires that the total emergent line and diffuse continuum luminosity equal the energy absorbed by the gas. In this case, the geometrical cross section of the cloud as seen from the center, $A_c(r)$, is another useful parameter.

Designate $\varepsilon_l(r)$ as the flux emitted by the cloud, in a certain emission line l, per unit projected surface area ($erg\ s^{-1}\ cm^{-2}$), we have the following relation for the cloud emission:

$$j_c(r) = A_c(r)\varepsilon_l(r). \tag{49}$$

We now make the following simplified assumptions about the radial dependence of the different parameters:

$$\varepsilon_l(r) \propto r^{-m}, \tag{50}$$
$$n_c(r) \propto r^{-p}, \tag{51}$$
$$A_c(r) \propto r^{-q}, \tag{52}$$
$$N(r) \propto r^{-s}, \tag{53}$$

and

$$v(r) \propto r^{-t}. \tag{54}$$

Using these definitions, the radial dependence of the ionization parameter is:

$$U(r) \propto r^{s-2}. \tag{55}$$

5.1.1. Covering factor. For optically thick clouds, it is useful to introduce the *covering factor, C(r)*, which is the fraction of sky covered by photoionized gas clouds, as seen from the center. For a single cloud

$$C(r) = \frac{A_c(r)}{4\pi r^2}, \tag{56}$$

and for a thin shell of thickness *dr*

$$dC(r) = A_c(r) n_c(r) dr \propto r^{-(p+q)} dr. \tag{57}$$

The integrated covering factor can be estimated from the Lyman continuum observations (chapter 2) or from comparing the line and continuum luminosities (chapter 6). For the more luminous AGNs it is about 0.1 for the BLR and less than that for the NLR. It is thus justified to neglect obscuration and proceed on the assumption that the flux reaching the clouds depends only on *r*.

5.1.2. Integrated line fluxes. Given the calculated $\varepsilon_l(r)$ for individual clouds (chapter 4), we can now integrate over *r* to obtain cumulative line fluxes. In the most general case

$$\begin{aligned} E_l(r) &\propto 4\pi \int_{r_{\rm in}}^{r_{\rm out}} n_c(r) A_c(r) \varepsilon_l(r) r^2 dr \\ &\propto \begin{cases} \frac{1}{3-(p+q+m)} \left[\left(\frac{r_{\rm out}}{r_{\rm in}} \right)^{3-(p+q+m)} - 1 \right] & (p+q+m \neq 3) \\ \ln \left(\frac{r_{\rm out}}{r_{\rm in}} \right) & (p+q+m = 3) \end{cases} \end{aligned} \tag{58}$$

There are interesting cases where the number of radius dependent parameters is considerably reduced. An important example is a system of spherical clouds, of radius $R_c(r)$, in pressure equilibrium with a confining medium of pressure P. The kinetic temperature of a photoionized gas is only a weak function of *U*, and we can safely assume that the radial dependences of *P* and *N* are identical ($\propto r^{-s}$). Since $R^3_c N = const.$, the cloud cross-section is

$$A_c(r) \propto R_c^2 \propto r^{2/3s} \tag{59}$$

(i.e. $s = -3/2q$) and the column density is

$$N_{\rm col}(r) \propto R_c N \propto r^{-2/3s}. \tag{60}$$

Assume further that the clouds are moving *in or out* with their virial velocity. Mass conservation ($n_c v r^2 = const.$) requires that $p = 2-t$ and substituting $t = 1/2$ we get the following radial dependence of the covering factor:

$$dC(r) \propto r^{2/3s-3/2} dr. \tag{61}$$

General considerations (chapter 9) suggest that $1 \leq s \leq 5/2$ in many cases of interest. In particular, $s = 9/4$ corresponds to a case where the covering factor of a thin shell is proportional to the shell thickness.

The *total* flux, in all forms of emission, from a shell of thickness *dr* is proportional to *dC(r)* (4), and the cumulative flux is proportional to

$$\frac{1}{2/3s - 1/2} \left[\left(\frac{r_{\rm out}}{r_{\rm in}} \right)^{2/3s-1/2} - 1 \right] \quad (s \neq 3/4). \tag{62}$$

This is, in fact, a good approximation for many individual lines (i.e. $m = 2$ is a good approximation for many lines).

We conclude that in those cases with $s > 3/4$, the cumulative covering factor, and therefore the integrated line emission, increases rapidly outward, and the innermost parts of the atmosphere do not contribute much to the line emission. For $s \leq 3/4$ much of the line emission takes place close to the center and there is a natural boundary to the cloud distribution. Note, however,

some potential difficulties. For example, the column density of ionized material depends on U and r, and clouds that are optically thick near r_{out} may become transparent closer in, or vice versa.

5.1.3. Specific models. Fig. 11 shows cumulative BLR line fluxes, as a function of r_{out} for a constant ionization parameter model, $s = 2$. They were calculated as explained in chapter 4, and added according to the prescription explained above. In this particular case, *L(ionizing continuum)* = 10^{46} *erg* s^{-1} $U = 0.3$ for all clouds and the normalization is such that $N_{col} = 2 \times 10^{23}$ cm^{-2} where $N = 10^{10}$ cm^{-3}. The integration starts at $r_{in} = 10^{16.5}$ *cm*, where the density is 10^{12} cm^{-3}, and carried out to large radii. Vertical cuts in the diagram correspond to a certain r_{out} and give the integrated line fluxes up to that radius.

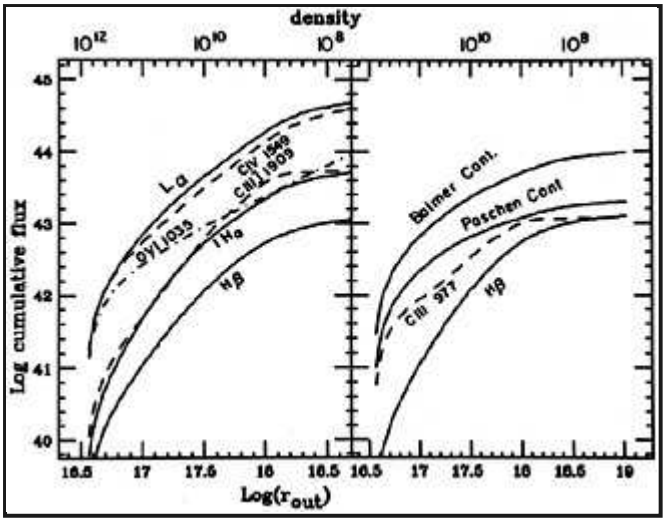

Figure 11. Cumulative broad line fluxes, as a function of r_{out}, for a model with $U = 0.3$ and $s = 2$. The model is calculated for the continuum shown in Fig. 7, assuming *L(ionizing luminosity)* = 10^{46} *erg* s^{-1}. the value of r_{out} for other luminosities is obtained by noting that $r_{out} \propto L^{1/2}$.

The narrow line fluxes can be integrated in a similar way, and Fig. 12 shows a model with $s = 1$, normalized such that $U = 3.6 \times 10^{-2}$ where $N = 10^5$ cm^{-3} and $N_{col} = 10^{22}$ cm^{-2}. Here again *L(ionizing luminosity)* = 10^{46} *erg* s^{-1}, the inner radius is at $10^{19.5}$ *cm* and the density there is 10^6 cm^{-3}. Note that here, and in the BLR model of Fig. 11, the line intensity shown is normalized in such a way that the covering factor is unity at the outermost radius shown.

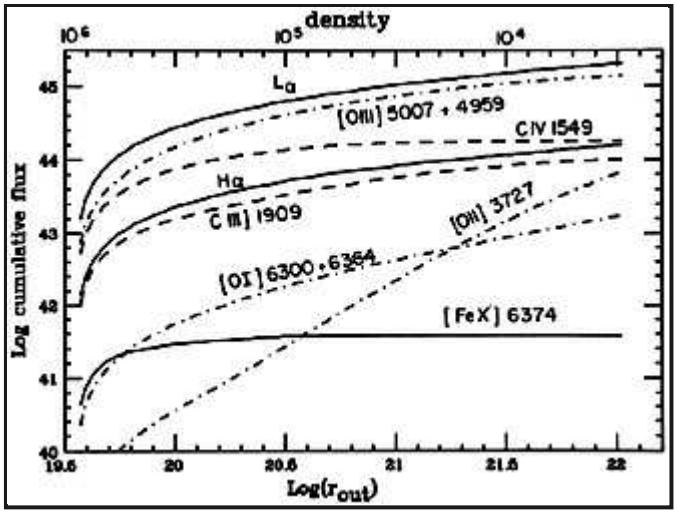

Figure 12. Cumulative narrow line fluxes, as a function of r_{out}, for a model with $s = 1$ and parameters as explained in the text.

---

[4] The radial dependence for individual lines is different, unless $m = 2$. Back.

5.2. Non-spherical Models

There are two classes of non-spherical models, having to do with the isotropy of the radiation field and the distribution of the line emitting gas.

5.2.1 Non-spherical gas distribution. The accretion of material with large angular momentum may lead to the formation of a flat rotating system. In particular, accretion disks are thought to play an important role in AGNs (chapter 10 and R. Blandford's contribution) and it is natural to surmise that the emission line region is an extension of the inner disk.

Some modifications of the spherical model are required in order to allow for the different geometry. The easiest way is to add an extra parameter, which is the latitude angle of the clouds. This would mean an angle dependent covering factor, which is easy to implement within the general integration scheme outlined above.

A more complex picture has been suggested in which part of the centrally emitted continuum radiation is reflected back by some scattering material above the disk surface. This class of models has been introduced to help explain the strong low ionization emission lines (chapter 6) and some line profiles (chapter 9). It assumes a very large accretion disk, up to 10^6 gravitational radii ($R_G = GM / c^2$). The lines are emitted from the outer parts of the disk, where they are excited by the back-scattered hard ionizing radiation. The high ionization lines, and most of the $L\alpha$ flux, come from a more "normal", spherical system of clouds, that are ionized by the non-scattered ultraviolet radiation. A schematic illustration of the model is shown in Fig. 13.

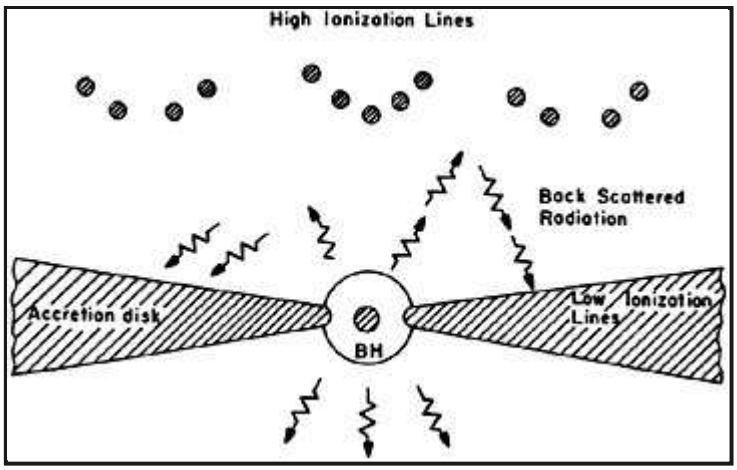

Figure 13. A schematic two-component model for the BLR. The high ionization lines are emitted in a spherical system of clouds, and are excited by the direct ultraviolet radiation of the central source. The low ionization lines come mainly from the outer regions of the central disk, where most of the line excitation is due to back-scattered, hard ionizing photons. (After Collin-Souffrin, Perry and Dyson (1988) , Collin-Souffrin (1986) and Dumont and Collin-Souffrin (1990)).

There are several important implications to the model, to do with the line profiles (chapter 9) and covering factor. A possible difficulty is the very large disk radii postulated to explain the line strength. As explained in chapter 10, and in R. Blandford's contribution, the structure of geometrically thin AGN disks is not well understood. Current models suggest that such disks are radiation pressure dominated, and their self gravity radius is of the order of 10^3 - 10^4 R_G. Much of the postulated low ionization lines originate outside this radius, where the disk, if it exists, is probably fragmented. This is, perhaps, not a strong objection considering the large uncertainties in the disk model. Moreover, a fragmented disk is as likely location for such lines as a uniform, continuous disk.

5.2.2 Anisotropic radiation field. A spherical or a flat cloud system can be illuminated by radiation from an anisotropic central source. This can be caused by relativistic beaming or by the combined effects of inclination and limb darkening in an accretion disk. The anisotropic disk radiation can be supplemented by an isotropic X-ray source, or perhaps some other components. Several examples of this continuum are shown in chapter 10. The ionization and excitation of the gas depends, in this case, on both r and the latitude angle of the clouds. This must be included in a modified integration scheme for calculating the cumulative line emission. Currently, there are too few observational constraints to test these ideas.

5.3 Bibliography

Relatively little has been done on combining isolated cloud models in the way described here. Rees, Netzer and Ferland (1989) suggested the general scheme and calculated many models for different values of s. Some more examples are given in Netzer (1989) . See also Viegas-Aldrovandi and Gruenvald (1984) for references on multi-cloud NLR models. The idea of low ionization disk emission lines is described in several papers by Collin-Souffrin and collaborators, see for example Dumont and Collin-Souffrin (1990) and references therein. Non-spherical models related to thin accretion disks are discussed in Netzer (1987).

6. Comparison with the Observations

As noted earlier, there are some 20 broad, isolated emission lines, and a similar number of narrow lines, that can be measured and compared with the model calculations. Each observed line ratio conveys different information about the line emission region, and there are more than enough constrains on the models. At this stage we are only interested in integrated line intensities. Later we discuss the information obtained from line variability (chapter 8) and line profiles (chapter 9).

6.1 The Broad Line Region

Fig. 14 shows a comparison of the composite quasar spectrum of Fig. 2 and the theoretical model of Fig. 11. The calculated line intensities, up to $r_{out} = 2 \times 10^{18}$ cm, are put on top of an artificial continuum, similar in shape to the observed one, and

normalized to give the observed $L\alpha$ equivalent width.

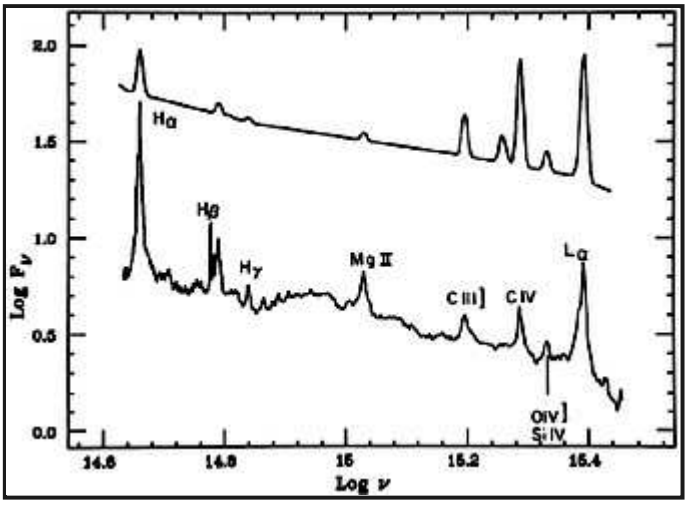

Figure 14. A comparison of a composite quasar spectrum (bottom) with model calculations.

Given the uncertainty in the model parameters, the difficult radiative transfer and the unknown gas distribution, it is quite remarkable that photoionization models for the BLR, like the ones describe here, give a good overall fit to the observed spectrum. Many of the observed line ratios are reproduced by the models and can be used to deduce important physical properties. There are, however, some line ratios that badly disagree with the model predictions, suggesting that some important ingredients are still missing. Below is a brief account of the present status of the theory, and the outstanding problems in this area.

6.1.1 Resonance metal lines. The strong ultraviolet lines of $CIV\lambda1549$, $NV\lambda1240$ and $OVI\lambda1035$ are good indicators of the gas temperature and ionization parameter. As seen from Table 1 and Fig. 14, the calculated strength of these lines, relative to $L\alpha$, are in fairly good agreement with the observations. The agreement is not as good in models of smaller U, although, a harder ionizing continuum can compensate, somewhat, for that. It has been proposed that optically thin BLR clouds, combined with much smaller ionization parameters, can explain the strong high excitation lines. Such clouds are expected to have very strong $NV\lambda1240$, $OVI\lambda1035$ and *HeII* lines. Their contribution to the total broad line flux is large only if their covering factor is much greater than the covering factor of the optically thick clouds.

The $CIII]\lambda1909$ / $CIV\lambda1549$ line ratio has been used, in the past, to deduce the ionization parameter. The models presented here clearly show this line ratio to be insensitive to the exact value of U. In fact, the line ratio is in good agreement with the observations over most of the range calculated, and disagreement appears only where the contribution of lower density material starts to dominate the spectrum.

6.1.2 Intercombination lines. Semi-forbidden lines such as $CIII]\lambda1909$, $NIII]\lambda1750$, $OIII]\lambda1663$ and $NIV]\lambda1486$, are weak in the inner part of the BLR, where the density is above their critical density ($\simeq 10^{9.5}$ cm^{-3} for $CIII]\lambda1909$). Further out, where the density is lower, such lines can be important coolants, and the energy distribution among the different cooling agents is changed. The presence of strong intercombination lines is a sign that the contribution of $N_e > 10^{10}$ cm^{-3} material to the emitted spectrum is not significant.

6.1.3 Broad forbidden lines. With the $N \propto r^{-s}$, $s > 0$ density law considered here, some forbidden lines, such as $[OIII]\lambda4363$, are predicted to be strong in large r clouds, where the density drops to their critical density ($\simeq 10^8$ cm^{-3}). Strong, broad forbidden lines are never observed, although there are hints to the presence of weak, broad $[OIII]\lambda5007$ in some objects. Thus, there seems to be a natural limit to the extent of the BLR. This may be due to the radial dependence of the covering factor at large r, to clouds becoming optically thin, or to some other reasons.

6.1.4 The hydrogen spectrum. The calculated intensity of $L\alpha$ in the $s = 2$ model (Fig. 11) increases with r much like the predicted $r^{5/6}$ dependence of (62). This reflects, mostly, the increase in the covering factor, and suggests that a fixed proportion of all ionizing photons are converted to $L\alpha$. It resembles the so called "recombination Case B flux", occurring in lower density nebulae, where each absorbed Lyman continuum photon results in the emission of a $L\alpha$ photon. In AGN BLR clouds, the situation is more complicated, due to the high density and large optical depth. However, in many models the calculated $L\alpha$ flux

is within a factor 2 of the simple, "Case B" value.

Despite the simple atomic configuration, the good atomic data and the big improvements in the treatment of line transfer, the hydrogen line spectrum of AGNs is not yet well understood. This is demonstrated in Fig. 14 where it is evident that the calculated $H\alpha$ and $H\beta$ lines are much weaker, relative to $L\alpha$, than in the observations. This has come to be known as the "$L\alpha$ / $H\beta$" problem. It is not yet clear whether it reflects wrong physical assumptions, the inaccuracy of the calculations or, perhaps, some reddening.

Regarding wrong physical assumptions, there are two proposed explanations. The first invokes a very strong, hard X-ray continuum, extending to MeV energies, and the second, extreme column densities ($\simeq 10^{25}\ cm^{-2}$). The two are not without difficulties. A strong X-ray-γ-ray continuum is observed only in very few AGNs (there are only very few such observations) while the "$L\alpha$ / $H\beta$" problem seems to be common to most objects. There are also problems in violating the γ-ray background if all AGNs have such a hard continuum. Large column densities are appealing for some reasons (see below) but the large Compton depth makes the line transfer calculations questionable, and there are difficulties associated with the physical size of the clouds in low luminosity objects (chapter 8).

The most likely cause for inaccurate calculations is the simplified escape probability treatment. Typical BLR clouds are expected to have huge $L\alpha$ and $H\alpha$ optical depths ($\tau(L_\alpha) \sim 10^8$, $\tau(H_\alpha) \sim 10^4$), and the local nature of this transfer method may not be adequate for such extreme conditions. Among the present dustless models, that use as an input the typical observed continuum, some get close to explaining the observed $L\alpha$ / $H\alpha$ ratio and some manage to reproduce the observed Balmer decrement, but none is successful in explaining both.

Line reddening is another possible explanation which is not without its difficulties. It is discussed in chapter 7.

6.1.5 The helium spectrum. The optical depth in many HeI lines must be large because of the high population of the HeI 2^3S metastable level. The $HeI\lambda 5876$, $HeI\lambda 10830$ and other HeI line intensities are likely to be affected by that, and accurate transfer calculations are required.

To date most accurate calculations consider an up to 100 level HeI atom, with optical depth in all lines. Such a large number of levels is needed since three-body recombination is important in populating the high energy HeI levels at the BLR densities. The calculated line intensities are quite reliable, but not reliable enough to use the model helium/hydrogen line ratios to determine the helium abundance.

The calculations of the HeII spectrum are much simpler. The optical depth in all lines, except for the Lyman series and, perhaps, $HeII\lambda 1640$, is small, and the three-body recombination process is not as important as in hydrogen. A notable problem is the $HeII\lambda 304$ $L\alpha$ line, which is a major ionization source for hydrogen and a major fluorescence excitation source for $OIII$. The approximate methods (chapter 4) that are used leave much to be desired and the calculated line intensity is rather uncertain. The observation of this line is a major challenge of space astronomy and a real comparison with the calculations is still to come. Another complication is the wavelength coincidence between the hydrogen $L\alpha$ and the HeII $H\beta$ lines (separation of 0.498Å). This is a potential pumping source for the HeII $n = 4$ level but it is thought to be unimportant because of the small optical depth in the HeII $H\beta$ line, and the relatively large wavelength difference, The result of the small optical depth, and the good atomic data, is that the $HeII\lambda\lambda 1640$ / 4686 line ratio is easy to calculate. This line ratio is an important reddening indicator and its use in determining the reddening in AGN clouds is explained in chapter 7.

6.1.6 FeII and MgII lines. The low excitation lines of FeII and MgII are produced in the partly neutral region of the BLR clouds. Such regions are thought to be heated and ionized by X-ray photons. They are characterized by $T_e \simeq 10^4 K$ and $N_{H^0} / N_{H^+} \simeq 10$.

While $MgII\lambda 2798$ is a relatively simple line to calculate, this is not the case for the FeII lines, because of the extremely complicated energy level configuration of Fe^+. There are several thousand FeII transitions to be considered, many with a large optical depth. The atomic data for this ion is poorly known and reliable cross sections are only starting to become available. An additional complication is the large number of wavelength coincidences of different FeII lines; more than 300 (!) with separation less than 10 $km\ s^{-1}$. This is a major population process for the levels that must be taken into account. Other potentially important processes are the absorption of incident continuum radiation in FeII lines and the continuos opacity due the hydrogen $n = 2$ level.

The large number of FeII lines form several distinct emission bands at 2200-2600Å, 3000-3400Å, 4500-4600Å and

5250-5350Å. The strongest ultraviolet FeII lines originate from some odd parity levels with energies of ~ 5 eV above the ground. Other ultraviolet lines, out of energy levels as high as 9 eV, are also observed. Such lines are not consistent with collisional excitation at the deduced electron temperature of ~ $10^4 K$ and fluorescence or some other unknown processes must be responsible for that. All this is not unique to AGNs. The same FeII lines are known to be strong in the spectrum of symbiotic stars; galactic objects with no hard X-ray continuum.

Fig. 15 demonstrates the complicated nature of the FeII spectrum. It shows a calculated FeII spectrum, for AGN clouds, with more than 3000 FeII lines. There is no way to isolate most of these lines, because of their large number and the broad line profiles. The convolution of the theoretical spectrum with a typical observed line profile (bottom part of the diagram) form broad, shallow emission features that demonstrate the difficulties in measuring the continuum luminosity, and the intensity of lines such as $MgII\lambda 2798$ and $H\beta$, in spectral regions rich in FeII lines. The conglomerations of the strong FeII lines, the Balmer continuum, and other spectral features, creates a noticeable energy excess between the wavelengths of 2000 and 4000Å. This feature is sometimes referred to as the "small bump" and was confused, in the past, with the underlying nonstellar continuum of AGNs.

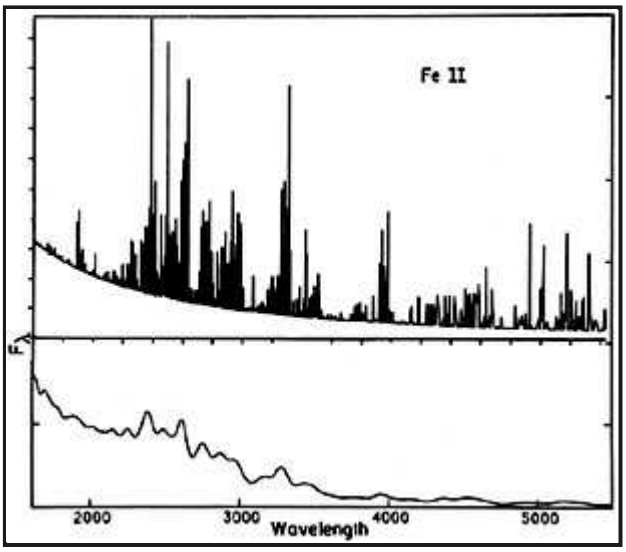

Figure 15. Top: A theoretical FeII spectrum on top of a power-law continuum. Bottom: the same spectrum but lines are 4000 $km\ s^{-1}$ gaussians.

The FeII spectrum is one of the unsolved problems of AGN study. The total observed strength of these lines can equal the $L\alpha$ intensity, while the calculated strength is only about 1/3 or 1/2 of that. The ratio of the optical FeII lines to the hydrogen Balmer lines presents a similar, or even bigger problem, and there is also a difficulty in explaining the observed ratio of optical FeII lines to ultraviolet FeII lines. Suggested explanations, within the general framework of photoionization, include very high densities, large iron abundances and emission from the outer regions of central accretion disks. There was also a suggestion of a different model, based on the idea that the lines are formed in a thick, warm medium which is mechanically heated. Such models have the extra degree of freedom of not being directly associated with the central radiation source.

6.1.7 CaII lines. These are the lowest ionization lines observed in the spectrum of AGNs. The strongest feature is the infrared triplet at 8498, 8542 and 8662Å. The lines are observed in about 1/3 of all objects, while other CaII lines, such as the *H, K* and the forbidden lines near 7300Å, are weak or absent. Theoretical modeling shows that the internal CaII line ratios, and their strength relative to $H\beta$, requires very large column densities, $N_{col} \sim 10^{25}\ cm^{-2}$. Such models are appealing for some theoretical reasons (energy budget, to be explained below, the $L\alpha$ / $H\beta$ problem) but there are difficulties as well. For example, objects with very weak CaII infrared lines are not very different, spectroscopically, from objects with strong CaII lines. In particular, strong CaII emitters are not very different in their $L\alpha$ / $H\beta$ from weak CaII emitters. If large column densities are essential to explain both the observed $L\alpha$ / $H\beta$ and CaII lines in AGNs, it is not very clear why the CaII lines are not more common Furthermore, very large column density clouds, with typical BLR densities, are more than $10^{15}\ cm$ thick, a dimension which is of the order of the cloud-central source separation in low luminosity AGNs (chapter 8).

6.1.8 Diffuse continua. The free-free continuum and several of the bound-free continua (Paschen, Balmer) are cavations.

6.1.9 Very high excitation metal lines. These lines (*CIII*λ977, *OIII*λ835 etc.) are calculated to be strong at small r high density clouds, where the temperature is high due to the collisional suppression of other cooling agents, such as *CIV*λ1549. The lines are weak or unobserved in most AGN spectra which is another argument against having a large contribution from very high density clouds to the broad-line spectrum.

6.1.10 Small dense BLR. Some gas clouds may survive in the innermost part of the BLR, where the radiation field is most intense. These must have very high densities (~ 10^{12} cm^{-3}) since low density material will not achieve thermal equilibrium at this environment (chapter 9). The clouds may be associated with the inflow of gas from the BLR, or perhaps produced near the central black hole. At such high densities the gas must be close to thermal equilibrium, most cooling is via bound-free and free-free emission and no line emission is likely to be important. The clouds are therefore reprocessing the central continuum radiation, absorbing it at some frequencies and re-emitting in others. The resulting spectrum can resemble, in some ways, the spectrum of a thin accretion disk, showing a "blue bump" in optical and ultraviolet energies and a strong edge at the Lyman limit. Currently there are too few observational constraints, and too many theoretical uncertainties, to put this idea into a serious observational test.

6.2. The Narrow Line Region

The observations of narrow lines in high luminosity AGNs are not nearly as good as those of the broad lines. In particular, it is difficult to separate the broad and the narrow ultraviolet lines and there are no reliable measurements of the narrow *CIV*λ1549 and *CIII*]λ1909 lines in quasars and Seyfert 1 galaxies. The situation is likely to be improved with the HST observations but so far the only narrow ultraviolet lines that have been measured are in Seyfert 2 galaxies.

There are very good observations of optical narrow lines that can be compared with the model predictions. The overall agreement is very good and narrow line models, like the one shown in Fig. 12, reproduce the relative strength of [*OIII*]λ5007, [*OII*]λ3727, [*OI*]λ6300 and $H\beta$ quite well. This is not the case for [*FeX*]λ6734, and the line is observed to be much stronger than predicted. A similar, although somewhat smaller discrepancy, occurs for the lines of [*NeV*] and [*FeVII*].

Line profile observations (chapter 9) indicate a large density gradient in the NLR. The validity of the model in Fig. 12, where the density gradient is quite small, is thus questionable and the very high ionization lines may come from a much denser part of the NLR. Another, very different suggestion is that the high ionization lines come from the interstellar medium of the host galaxy.

Lower excitation spectra, such as in LINERs, cannot be explained by the relatively high ionization parameter model of Fig. 12. Such spectra are discussed in chapter 11.

The intensity of the narrow Balmer lines are easy to calculate. The $H\alpha$ optical depth is not likely to be large, and the $H\alpha$ / $H\beta$ ratio is closed to the Case B value. A comparison with the theoretical $L\alpha$ intensity is somewhat less reliable. First, the line is likely to be collisionally excited by a density dependent amount. In addition, the typical NLR density is close to the critical density of the 2-photon transition (~ 1.5 × 10^4 cm^{-3}) and the relative population of the hydrogen $2s$ and $2p$ levels may be different in different clouds. Because of this the recombination $L\alpha$ / $H\beta$ ratio can vary from about 23 (low density limit, the $2s$ and $2p$ levels are not coupled) to 34 (high density limit, the $2s$ to $2p$ population ratio is 1:3). Combined with the collisional enhancement of $L\alpha$, the overall expected range in the $L\alpha$ / $H\beta$ ratio is about 25-100. Accurate modeling is required fo comparing this line ratio with the observations.

6.3. The Energy Budget of the BLR

While the individual line ratios are the best indicators for the physical conditions in the BLR clouds, a simple energy conservation argument provides another strong constraint on the models.

Consider optically thick clouds absorbing *only* ionizing radiation, and no reddening by dust. The total energy emitted by the clouds is simply the energy absorbed by them, which is the product of the ionizing radiation and the covering factor. Photoionization calculations for the BLR indicate that the emitted $L\alpha$ flux is not very different from the "Case B flux' mentioned earlier, whereby each absorbed ionizing photon results in one $L\alpha$ photon. In this case the number of $L\alpha$ photons is the product of the number of ionizing photons and the covering factor. Combining the two we have a simple observational way to measure the mean energy of an ionizing photon, $\bar{\nu}$ (in Ryd.):

$$\bar{\nu} = \frac{total\ energy\ emitted\ by\ the\ clouds}{number\ of\ L_\alpha\ photons}. \qquad (63)$$

This is a most important information about the shape of the Lyman continuum that cannot be obtained by direct observations of the Lyman continuum.

The integrated flux emitted by the BLR clouds is not easy to measure since some of it is in broad spectral features, such as the "small 2000-4000Å bump", the Paschen continuum and several infrared lines. It is estimated to be 5-9 times the $L\alpha$ intensity which means, according to the above relation, $\bar{\nu} \simeq 4$ - 7 Ryd.

To illustrate this further assume that the ionizing continuum is a simple power-law in energy, $L_\nu = C\nu^{-\gamma}$, extending up to a cut-off frequency ν_{cut}, where ν is in Rydberg and C is a constant. The mean energy of an ionizing photon is

$$\bar{\nu} = \frac{\int_1^{\nu_{cut}} C\nu^{-\gamma} d\nu}{\int_1^{\nu_{cut}} C\nu^{-\gamma-1} d\nu} = \left(\frac{\gamma}{1-\gamma}\right) \frac{1-\nu_{cut}^{1-\gamma}}{\nu_{cut}^{-\gamma}-1}, \qquad (64)$$

where we have assumed $\gamma \neq 1,0$. This expression should be compared with (63) to obtain the value of γ. For example, for ν_{cut} = 10 *Ryd*, which is consistent with the observational constraints mentioned in chapter 4, we get $\gamma \simeq 0$. This is in conflict with the observations that show a typical observed slope, at a rest wavelength of 1000Å, of about γ = 0.6 and an even steeper slope at shorter wavelengths. The discrepancy has been named "the energy budget problem".

There are several suggested solutions to this problem. First, only the soft ($\nu \leq 10$ *Ryd*) Lyman continuum photons have been considered here while high energy photons are observed in almost all AGNs. Such photons hardly interact with the gas unless the column density is much greater than 10^{23} cm^{-2}. Very thick clouds have been suggested, in which a large fraction of the high energy continuum is absorbed by the gas. Thick clouds can also absorb the infrared continuum, which helps too. Second, the models may be wrong, in particular the assumption about the number of $L\alpha$ photons and its relation to the ionizing flux. Also, the observed lines may come from two distinct parts of the BLR (the surface of the central disk?). Third, the above argument makes use of the intrinsic properties of AGNs, but the observed fluxes may be different from the intrinsic fluxes. For example, reddening by dust can change the observed line ratio and the inferred mean photon energy. None of these explanations is entirely satisfactory and it is likely that the real solution involves some combination of all.

A somewhat related problem is the ratio of the high and low excitation lines. Generally speaking, much of the "soft" ionizing flux ($\nu \leq 20$ *Ryd*.) is converted to recombination and high ionization lines, while the harder photons, that can penetrate much deeper, are converted to low excitation lines. It can thus be argued that the flux ratio of high to low ionization lines is a measure of the flux at different wavelengths. One can use it to formulate a "second order energy budget problem" related to the fact that the observed low excitation lines of MgII and FeII are too strong relative to $H\beta$. This cannot be solved by reddening but the argument is based, to a large extent, on the observed FeII lines, that are not well understood.

There are other methods for estimating the shape of the ionizing continuum. In particular, the equivalent width (EW) of the recombination lines can be used for that. For example, the "Case B" $L\alpha$ equivalent width, for a system of optically thick clouds with a covering factor *C(r)*, around the above power-law continuum, is:

$$EW(L_\alpha) = \frac{1215}{\gamma}(3/4)^\gamma [1-\nu_{cut}^{-\gamma}] C(r)\mathring{A} \quad (\gamma \neq 0). \qquad (65)$$

A similar ratio can be calculated for *EW(HeII*λ1640), where the integration in this case is for $\nu \geq 4$*Ryd*. The observed EW of these two lines can be compared with this theoretical prediction in order to estimate the continuum slope around 1-4 Ryd. Alternatively, the EW of the HeII lines, combined with an assumption on the covering factor, can be used to estimate L_ν(1640Å) / L_ν(228Å) etc. These arguments cannot be simply used in the disk-like geometry mentioned in chapter 5.

6.4. Bibliography

Many of the theoretical papers mentioned in chapters 4 and 5 include also a detailed comparison with the observations. Specific references addressing topics in this chapter are:

General BLR models: Rees, Ferland and Netzer (1989, very high density models), Ferland and Persson (1989, very large U and N_{col} models, the most complete discussion of the CaII lines), Krolik and Kallman (1988, line ratio dependences on continuum shape), Collin-Souffrin, Hameury and Joly (1988, thick Compton heated BLR clouds).

FeII lines: Netzer and Wills (1983, FeII line fluorescence, general FeII line calculations), Wills, Netzer and Wills (1985, more detailed FeII models and a comparison with the observations), Penston (1987, $L\alpha$ fluorescence with FeII), Joly (1987, detailed FeII calculations for a medium which is mechanically heated), Collin-Souffrin et al. (1988, FeII lines from a Compton heated media), Dumont and Collin-Souffrin (1990, FeII lines from scattered radiation on accretion disks). Many detailed articles on FeII lines can be found in the proceedings of the 94th IAU colloquium held in 1986 (Viotti, Vittone and Friedjung editors, Reidel publishing company).

Small dense BLRs: Ferland and Rees (1988).

Energy budget and continuum slope: Netzer (1985, first presentation of the energy budget problem), Collin-Souffrin (1986, further elaboration and separation into low and high excitation lines), Ferland and Persson (1989, application to a large N_{col} clouds), MacAlpine et al. (1985, determination of the Lyman continuum slope from HeII lines).

NLR models: Ferland and Osterbrock (1986).

7. DUST AND REDDENING

Dust is associated with cool astrophysical gas in almost all known nebulae and it is hard to imagine that AGNs are exceptional in this respect. There are three ways to discover the dust, via its thermal emission, through its effect on the observed spectrum (extinction) and by light polarization. This review is concerned with AGN emission lines and the information they reveal about the physical conditions in the nucleus. Therefore we concentrate on the extinction and mention the two other dust properties only to the extent that they are likely to be correlated with the dust causing the extinction.

7.1. Thermal Emission and Polarization

Consider an optical-ultraviolet continuum source with integrated luminosity L_{46} ($10^{46} erg\ s^{-1}$), surrounded by a cloud of dust particles at a distance r_{pc} parsecs. The particles absorb the optical and ultraviolet continuum radiation and re-emit it at infrared energies. Assume spherical particles and an absorption-emission infrared coefficient which is proportional to λ^{-1}. The quilibrium dust grain temperature, T_{dust}, is given to a good approximation by

$$T_{\rm dust} \simeq 1700 L_{46}^{0.2} r_{\rm pc}^{-0.4} K. \qquad (66)$$

The maximum temperature at which dust can survive is about 1700 *K*, thus the evaporation distance, r_{ev} is roughly

$$r_{\rm ev} \simeq L_{46}^{1/2} pc. \qquad (67)$$

This distance is just outside the estimated BLR size (chapter 8). Thus, dust particles cannot survive in the BLR unless they are shielded from the central radiation source. They can survive almost anywhere outside the BLR, in particular in the NLR.

There are several theoretical suggestions, as well as some observational evidence, that hot dust, just outside the BLR, is responsible for at least some of the observed infrared radiation of luminous AGNs. One possibility is that the dust is in a flat disk-like configuration, which is the extension of the inner accretion disk. Spherical dust distribution has been considered too. There is at least one bright Seyfert galaxy, F-9, where the dimension of the dust cloud has been measured directly, since in this case the large changes in the optical-ultraviolet radiation of the central source induced a similar, but delayed variation in the infrared dust emission. The time lag between the optical and the infrared continuum variation, when converted to physical dimension through the speed of light, indicates that the nearest dust grains are at a distance which is comparable to the evaporation distance of equation (67).

7.2. Internal and External Dust

The dust in external galaxies may not have exactly the same extinction properties as in our interstellar medium. In particular, some of the broad extinction features, such as the one centered at 2200Å, may be weak or absent in other galaxies. The amount of extinction will be estimated assuming a galactic dust-to-gas ratio and a simple, λ^{-1} extinction law. Thus, for a dust on the line of sight to the source, the extinction in magnitude, for a gas column density N_{col}, is

$$m_\lambda \simeq 0.5 \left[\frac{N_{\rm col}}{10^{21} cm^{-2}}\right] \left[\frac{5000\mathring{A}}{\lambda}\right]. \quad (68)$$

Dust can also be mixed in with the gas, absorbing both the external incident radiation and the internally produced line photons. The first and large effect on the emergent spectrum is the extinction of the ionizing radiation in a wavelength dependent way. This can be incorporated into the photoionization calculations provided the extinction properties of the dust at $\lambda \leq$ 912Å are known.

Internal dust can also destroy line photons with an efficiency that depends on the wavelength and the optical depth of the line in question. For forbidden lines, intercombination lines, and all other lines of negligible optical depth, the absorption probability is simply [1 - exp(-$\tau_{\rm dust}$)] and depends only on the line frequency. This is not the case for resonance lines and other lines of considerable optical depth, where the lengthening of the path before escape is considerable (about a factor of 5, see section 4.4.2) due to the large number of scatterings. Such line photons are easily destroyed by dust and the result is a considerable weakening of the large optical depth lines compared with all other lines. AGN observations do not show any large reduction in the strength of $L\alpha$, *CIV*λ1549, and other optically thick lines, compared with the calculated intensity of the intercombination lines like *CIII*]λ1909. Therefore, the amount of internal dust, at least in the BLR clouds, cannot be large.

It is easy to incorporate these effects into the calculations using the formalism described in chapter 4 (equations 42-46). The main complication is the unknown dust distribution, which may not be uniform. In particular, the neutral gas zone is a more likely location for the dust particle to survive the intense radiation of the central source. Finally, internal dust can also change the hydrogen line spectrum in a low density gas, by providing a de-excitation mechanism for some high energy levels, decreasing, in this way, the effective optical depth of the Lyman lines.

7.3. Dust and Reddening in the NLR

The reddening of the narrow emission lines can easily be measured from the observed intensity of the Balmer hydrogen lines. The only modification that is required is a small correction to the predicted $H\alpha$ / H_β, since the intrinsic narrow-line ratio in Seyfert 1 and Seyfert 2 galaxies is about 3.1, rather than the 2.8 calculated from simple recombination theory (possibly a small collisional contribution to $H\alpha$). Other potential reddening indicators for the NLR are the HeII lines at 4686, 3204 and 1640Å the [SII] lines at 10320, 6716+6731 and 4069+4076Å, and perhaps some [OII] lines. The HeII lines are the most promising in this respect, since the theoretical ratios are well known. However, so far only the hydrogen lines have been used, because of the low sensitivity of the pre HST ultraviolet experiments. A further observational limitation in Seyfert 1s and quasars is the uncertainty associated with the separation of the broad and narrow line profiles.

Observations of many narrow line AGNs clearly show a significant amount of line reddening. The amount range from very small to extremely large. In particular, some of the NLXGs show indications for a very large amount of line and continuum extinction. Some papers suggest that the amount of extinction is correlated with the inclination of the host galaxy, being larger in edge-on galaxies. There are other reasons to believe that the obscuring gas has a flattened distribution, thus the amount of extinction can vary a lot from object to object.

The narrow emission line profiles provide another indication for dust in NLRs. Many lines have a noticeable blue asymmetry which is interpreted as a combination of radial motion and dust obscuration. Line profiles are further discussed in chapter 9.

7.4. Dust and Reddening in the BLR

As discussed in the previous chapter, the agreement between models and observations of the BLR is very good for some lines and poor for others. For luminous AGNs, the comparison between the observations and the models (Fig. 12) suggests a smooth trend, in a sense that calculated ultraviolet line intensities, relative to $L\alpha$, are in better agreement with the observations compared with the calculated optical line intensities. The disagreement may thus be a continuos function of wavelength, which is typical of reddening by dust. A small amount of line-of-sight extinction ($m_{\rm V} \simeq$ 0.6 mag.) can considerably reduce this discrepancy. Unfortunately, the situation is far from being simple. The uncertainty in current BLR models is more than enough to account for the above discrepancy and there are several other explanations for this discrepancy.

As for the low luminosity AGNs, there are strong indications that the faint, broad Balmer line wings observed in many of those, are heavily reddened. In view of the observational and theoretical limitations, the idea of reddening in BLRs must be investigated by looking for emission line ratios that are good reddening indicators.

Most broad emission lines are optically thick and their calculated intensity somewhat uncertain. In particular, the $L\alpha$ / $H\alpha$ / H_β

ratio cannot be used as a reddening indicator because of the complicated line transfer and other uncertainties already discussed. The situation regarding the hydrogen Paschen lines is somewhat better, and the uncertainty involved in the calculated ratio of lines originating from a common upper level, such as $P\beta$ and $H\gamma$, is perhaps not as large. Out of all other emission lines, only two line pairs seem to be adequate reddening indicators. These are the HeII and the OI line pairs discussed below.

7.4.1 Reddening from HeII lines. As discussed in the previous chapters, the HeII spectrum of broad line AGNs is relatively simple and reliable calculations are already available. The complicated HeII $L\alpha$ transfer does not influence the HeII Balmer and Paschen lines, and even the small optical depth in the HeII $H\alpha$ line, at 1640Å, does not change the line ratios by too much. Thus, the theoretical Paschen and Balmer HeII lines can be compared with the observations to check for reddening. In particular, the theoretical calculations predict that

$$8 \leq \frac{HeII\ \lambda 1640}{HeII\ \lambda 4686} \leq 11. \qquad (69)$$

Currently, there are not enough reliable measurements of this line ratio to make any general statement about reddening in BLRs. There are some indications, in a few objects, that a small amount of reddening is indeed present. The observations are difficult because of the weakness of the HeII lines and the blending with nearby spectral features. They are also hampered by the large time variation in the intensity of the HeII lines in low luminosity AGNs.

The $HeII\lambda 10123$ line has now been measured in several sources and can be used, given adequate infrared spectral resolution, as another reddening indicator for low redshift AGNs.

7.4.2 Reddening from OI lines. The calculated OI line spectrum is somewhat model dependent because of the fluorescence with $L\beta$. However, most of the emission in the OI lines at 8446 and 1302Å (Fig. 6) is due to this process and there is only a little extra contribution to the $OI\lambda 1302$ line due to collisional excitation. As a result, the line ratio is easy to calculate and it is a useful reddening indicator. Recent photoionization calculations suggest the following range for the theoretical line ratio:

$$4.5 \leq \frac{OI\ \lambda 1302}{OI\ \lambda 8446} \leq 6.5. \qquad (70)$$

Here again the measurements are very difficult to perform and there are only a handful of those. The little information available so far suggest some broad line reddening, by an amount which is highly uncertain.

7.5. Continuum Reddening

Continuum reddening has been investigated too. This has been clearly seen in some narrow line AGNs but the situation regarding broad line objects is not very clear.

The diversity in the shape of the optical-ultraviolet continuum of Seyfert 1 galaxies and quasars is not very large. This would argue against dust extinction since the effect on the continuum slope is likely to be large, even for a very small amount of dust. Arguments to the contrary have also been raised and there is no conclusive evidence yet. It is however clear that a small proportion of AGNs show a very steep ultraviolet continuum, with a shape that is entirely consistent with dust extinction. It is also clear that the Lyman continuum of some quasars, including low redshift ones (i.e. no significant intergalactic absorption) is too steep to account for the observed emission line strength in these objects.

The dust, if it exists, may have a very different effect on the line and continuum spectra. The dust location is thus of primary importance and further progress in this area must await until this is better understood.

7.6 Bibliography

Comprehensive reviews on dust and reddening in AGNs can be found in MacAlpine (1985) and in Osterbrock's book (1989).

Thermal emission and polarization: For model involving dust emission see Barvainis (1987) and Sanders et al. (1989) and references therein. The delayed infrared continuum response in F-9 is described in Clavel, Wamsteker and Glass (1989). There are several infrared polarization studies of quasars, but most of the polarization in such cases is due, probably, to a non-thermal source. A convincing case of dust polarization is described by Rudy and Schmidt (1988). For references on the polarization of Seyfert galaxies see chapter 11.

Internal dust: See Ferland and Netzer (1979), Martin and Ferland (1980) and Cota and Ferland (1988).

Narrow line reddening: Many references are given in MacAlpine (1985). See also De Zotti and Gaskell (1985).

Broad line reddening: See MacAlpine (1985) for references until 1985. Also Ward et al. (1987, use of Paschen and HeII lines), Wamsteker et al. (1990, HeII lines in NGC 5548) and Goodrich (1990, BLR reddening in Seyfert type 1.8-1.9).

Continuum reddening: See references in Lawrence and Elvis (1982) and MacAlpine (1985). Also Sanders et al. (1989).

8. Line and Continuum Variability: Mapping the BLR

The energy output of most AGNs is changing with time, in some cases by a large factor. Such changes in ionizing luminosity drive similar changes in emission line intensities, and the two are expected to be well correlated. This has been observed in many broad line objects and is a clear indication that photoionization is the main source of excitation for the BLR gas. Variable narrow lines are not usually observed, which is explained by the much larger extent of the NLR. The correlated line and continuum variability, and the mapping of the gas distribution, are the subject of this chapter.

8.1. Line and Continuum Light Curves

Consider the case where the continuum luminosity is changing with time. We assume that the recombination time (chapter 4) is much shorter than the light travel time across the line emitting region, and the dynamical time (chapter 9) is much longer than the typical variability time. (5) Thus the gas distribution and the covering factor are not changing with time. We neglect changes in continuum shape and drop the frequency dependence of L_ν, thus $L(t)$ is the *continuum light curve*.

The observed flux in a certain emission line depends on the gas distribution and is also a function of time. Consider the line l whose integrated luminosity, for a constant continuum output, is E_l. The time dependence of E_l is a result of both the varying ionizing continuum and the light travel time across the BLR. A distant observer sees different parts of the BLR responding to a certain continuum variation at different times. If the continuum varies much faster than the light crossing time, the line will be roughly constant, and no information on the geometry will be obtained. For a slower varying continuum, in a symmetric system of clouds, there will be a time lag between the continuum change and the line response which is roughly r/c, where c is the speed of light and r is a "typical" BLR size, to be defined later.

In what follows we assume a similar response for all emission lines and drop the l. For optically thick clouds, the last statement is equivalent to the assumption that the line flux is linearly dependent on the continuum flux, or, in the notation of chapter 5, $\varepsilon_l(r) \propto r^{-2}$. We define $E(t)$ to be the *line light curve* and note that because of the time dependence this is not entirely consistent with the definition of E_l in chapter 5 (equation 58).

The relation between $L(t)$ and $E(t)$, and the information derived from it, will be demonstrated using the specific case of NGC 4151. This source is a well known Seyfert 1 galaxy, whose line and continuum variability are well documented. It was monitored extensively, from the ground, in 1988, and clear variations of the nonstellar continuum and the hydrogen Balmer lines were seen. This is illustrated in Fig. 16.

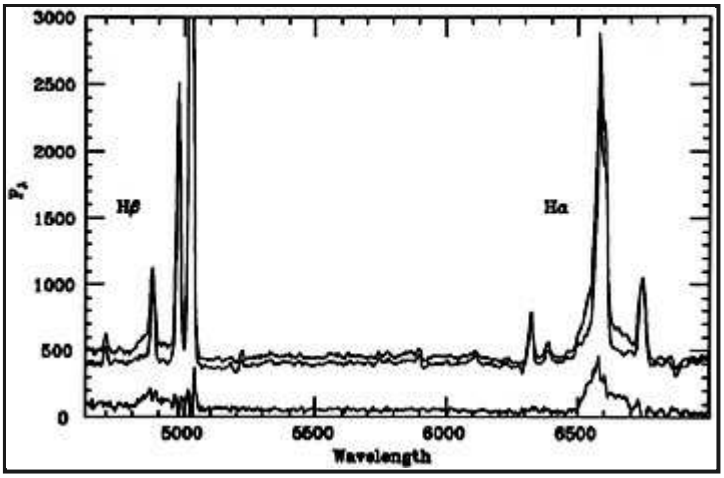

Figure 16. Two spectra of NGC 4151, obtained at the Wise observatory on Jan. 20 and July 17, 1988. The lowest curve is a difference spectrum, showing the variation in broad emission lines and continuum fluxes (from Maoz et al. 1991).

The $H\alpha$ and optical continuum light curves of NGC 4151, during 1988, are shown in Fig. 17. There are 55 observations, obtained over a period of 216 days. The mean sampling interval is about 4 days, but there are some large gaps, as well as periods of more frequent sampling.

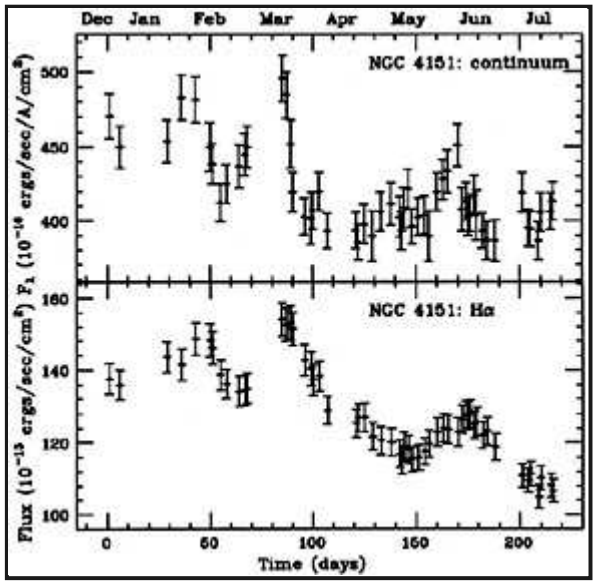

Figure 17. The optical continuum (4730Å) and the $H\alpha$ light curves of NGG 4151 in 1988 (Maoz et al. 1991).

---

[5] The dynamical time for Seyfert 1 galaxies is only a few years (chapter 9) and this assumption may not always hold. Back.

8.2. Cross Correlation

A main aim of studying the line and continuum light curves is to measure the "BLR size". This quantity may be defined in several different ways. For example, an emissivity-weighted average radius, r_{av}, is defined by

$$r_{av} = \frac{\int_{r_{in}}^{r_{out}} r dE(r)}{\int_{r_{in}}^{r_{out}} dE(r)}. \quad (71)$$

Other measures of the "BLR size" are mentioned below.

Cross correlating the line and continuum light curves is a simple way of estimating the dimension of the line emitting region. This is a well known technique, designed to give the most likely time-lag between the line and continuum pulses. The Cross Correlation Function (CCF) is a set of correlation coefficients, giving a measure of the correlation between the line and continuum light curves for certain chosen time lags. Fig. 18 shows the CCF for the two light curves of NGC 4151. A clear broad, significant peak (a correlation coefficient of 0.85 for 55 points) is seen at a lag of 9 days. This time lag, multiplied by c, can be defined as "the cross-correlation size" of the BLR.

There are several problems in applying the cross correlation method to real data sets. Some interpolation is required in order to use this procedure for unevenly sampled light curves. This can be disastrous in cases of large gaps in the data and/or short data strings. Observational errors can also affect the position of the CCF peak. As a general rule, the mean sampling interval must be considerably shorter than the typical continuum variability time scale. This reduces the interpolation errors and the resulting uncertainty in the position of the peak. Finally, the cross-correlation peak position depends on the nature of the continuum light curve and the response (linear or non-linear) of the lines. Thus the above mentioned "cross-correlation size", obtained from the CCF of one emission line, is not very well defined.

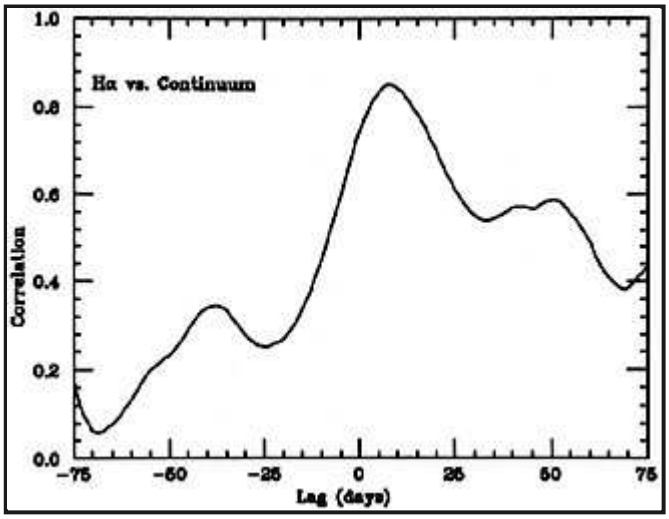

Figure 18. The cross-correlation function of $H\alpha$ vs. the optical continuum of NGC 4151 (Maoz et al. 1991).

A serious limitation of the cross correlation analysis is the lack of a solid criterion for estimating its uncertainty. Some formulaebservations. Here, again, the meaning of the derived time-lag uncertainty is somewhat ambiguous.

A main disadvantage of the cross correlation method is the fact that the entire data set, sometimes the result of one or two observing seasons, is used to obtain *one number* (the time lag). Weather, telescope scheduling and other limitations result in a random sampling of the intrinsic light curve which, if sampling is not frequent enough, means an uncertain result. Many more experiments, of similar duration, must in principle be performed in order to asses the accuracy of such results. This is not practical and numerical simulations, mimicking the real observing conditions, are used instead. One method developed for this purpose utilizes Monte-Carlo simulations to find the Cross Correlation Peak Distribution (CCPD) which gives the probability of finding the peak of the CCF at a certain lag, given an assumed continuum light curve and a certain geometry. Obviously, the CCPD is narrower, and the results more meaningful, for cases of frequent sampling and high signal/noise data.

Finally, the time lag obtained from the peak of the CCF is not necessarily a good indicator of the gas distribution, even for well sampled light curves. It tends to weight the inner parts of the line emission region more than the outer parts, in a way which depends on the continuum light curve. For thick geometries, the cross-correlation size is considerably smaller than the emissivity-weighted radius, r_{av} of (71).

8.3. The Transfer Function

A more ambitious task is to try and map out the entire BLR, using information obtained from the light curves.

Given the assumption of linear response of the line to the continuum pulse, we can formulate the relation between *L(t)* and *E(t)* using a "transfer function", $\Psi(t)$, (called also a "response function"):

$$E(t) = \int_{-\infty}^{\infty} L(\tau)\Psi(t-\tau)d\tau, \qquad (72)$$

i.e. *E(t)* is the convolution of *L(t)* with $\Psi(t)$.

As can be seen from this equation, $\Psi(t)$, in appropriate units, equals the *E(t)* that would result from *L(t)* which is a δ-function at $t = 0$ (a continuum "flash"). For gas which is distributed in a thin shell of radius r, the transfer function is a "boxcar" shaped pulse, lasting from $t = 0$ until $t = 2r/c$, with a constant value of $c / 2r$. The rise at $t = 0$ is due to the fact that the gas along the line of sight appears to respond immediately to the continuum pulse, and the information about the continuum and line variation arrived to the observer simultaneously. The constant value of $\Psi(t)$ results from the time delay of a ring at a polar angle θ, $r(1 - \cos\theta) / c$, and the emissivity of the ring which is proportional to its surface area. In a similar fashion the transfer function of a circular ring, inclined at an angle i to the line of sight, is non-zero between times $r(1 - \sin i) / c$ to $r(1 + \sin i) / c$, with its center at time r/c, This is illustrated in Fig. 19.

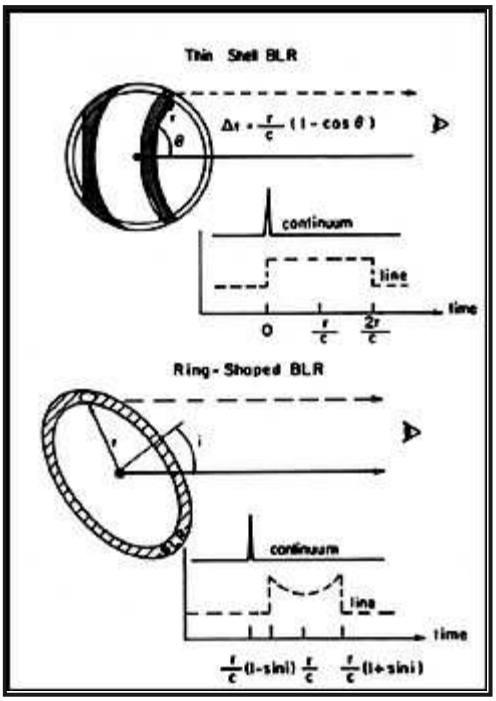

Figure 19. The response of a thin shell and an inclined ring emission line regions to a δ-function continuum light curve. (Shaded area in the top half shows the narrow ring at a polar angle θ.) For such a continuum variation, the shape of transfer function $\Psi(t)$, is identical to the shape of the line light-curve.

The transfer function of a thick shell is obtained by integrating the thin shell $\Psi(t)$ over all radii and weighting the contribution at each radius according to the emissivity. The case of a shell of inner radius r_{in} and outer radius r_{out} is shown in Fig. 20. As seen from this diagram, $\Psi(t)$ is a constant in time between $t = 0$ and $t = 2r_{in} / c$, and declines to zero between $t = 2r_{in} / c$ and $t = 2r_{out} / c$. The shape of the declining part depends on the gas distribution and emissivity. We can find this shape in the simple, optically thick case, using the notation of chapter 5 and the radial dependence of the covering factor from equation (57),

$$\Psi(t) \propto \int \frac{dE(r)}{r} \propto \int \frac{dC(r)}{r} \propto r^{-(p+q)} \quad (p+q \neq 0). \tag{73}$$

This is illustrated in Fig. 20 for the cases of $(p + q)$ = -2, 0 and +2. In a similar fashion, the transfer function of a thick disk is obtained from integrating over rings.

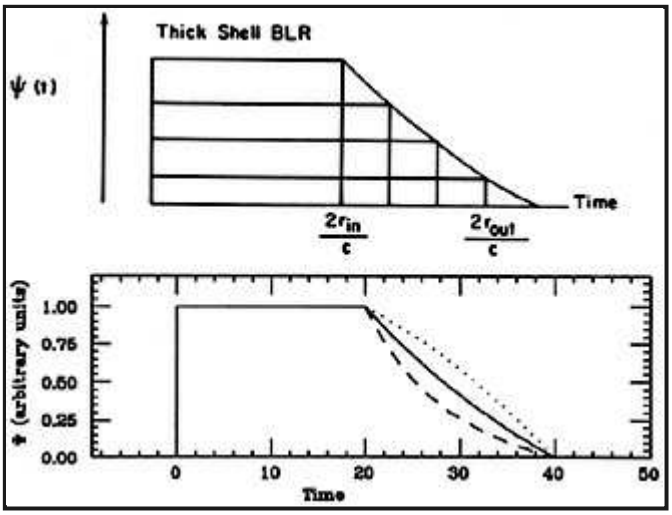

Figure 20. Bottom: Transfer functions of a thick spherical shell of inner radius 10 time units and outer radius 20 time units, for cases of $(p + q)$ = -2 (dotted line), 0 (solid line) and +2 (dashed line). The top half demonstrate the contributions of different thin shells to $\Psi(t)$, for the case $(p + q) = 0$.

We see that valuable information about the gas distribution can be obtained from $\Psi(t)$ and it is desirable to find this function and investigate its shape. In principle, this is not a difficult task since $\Psi(t)$ can be recovered from the data by applying the convolution theorem,

$$\tilde{\Psi}(\omega) = \frac{\tilde{E}(\omega)}{\tilde{L}(\omega)}, \tag{74}$$

where ~ designates the Fourier transform. Performing this operation, using the observed *L(t)* and *E(t)* and transforming back to the time domain, recovers $\Psi(t)$. In practice, this is not a trivial task. *E(t)* and *L(t)* are often unevenly sampled in time, have large gaps and span a relatively short period. Under such conditions, Fourier methods become problematic, and a meaningful transfer function may become hard to obtain. Frequently sampled data, with a sampling interval shorter than the typical variability time scale, can be quite useful, provided the light curve is long enough and the measurement error small compared with the variability amplitude. There are improved statistical methods of recovering $\Psi(t)$ from the data (e.g. the maximum entropy method), using additional constraints on its expected shape at different times.

The transfer function for NGC 4151, obtained from applying the maximum entropy method to the data presented here, is shown in Fig. 21. The diagram also shows the $H\alpha$ light curve which is obtained by convolving this function with the continuum light curve. The fit of the $H\alpha$ light curve is quite satisfactory, suggesting that this $\Psi(t)$ is not a bad approximation to the real transfer function. The empirical $\Psi(t)$ rises sharply at $t = 0$ and drops to zero, in a gradual way, over 30 days. This is consistent with a thick shell geometry with a very small inner radius and an outer radius of about 15 light-days. It is also consistent with an edge-on disk (and other geometries) of similar dimensions.

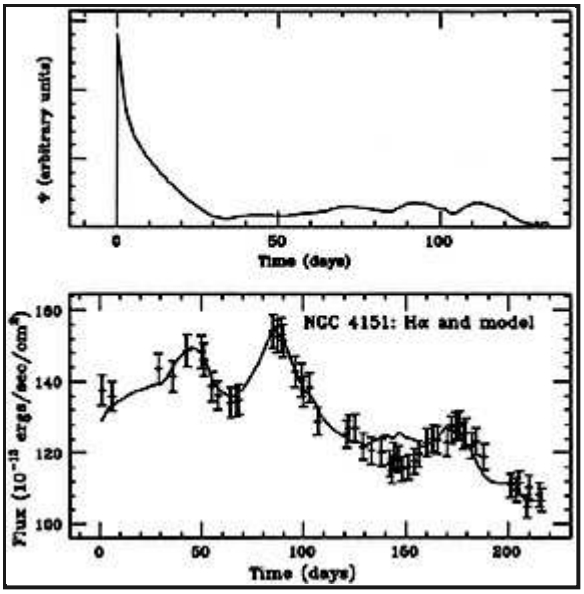

Figure 21. Top: Transfer function for NGC 4151, obtained from the line and continuum light curves in Fig. 17, using a maximum entropy deconvolution. Bottom: A model emission line light curve obtained from the transfer function, on top of the $H\alpha$ light curve.

A word of caution is in order. There are cases where several different transfer functions can fit the data equally well. This depends on the numerical method used and the quality of the light curves. For example, the features in the NGC 4151 transfer function at t ~ 50 - 100 days can be interpreted as due to some line emitting material far away from the nucleus. However, they can also be due to the numerical method used, given the freedom to put the emitting material anywhere around the central source. Physical constraints, such as an imposed upper limit on the BLR extension, should be used in such cases.

The experimental limitations are so severe that today the BLR transfer function is only known in one or two cases. The main problem in ground-based observations is the large amount of telescope time needed for proper sampling of the light curve, and the requirement of flux calibrated data. Space-born instrument are more suitable for the task but the aperture size of most of these is small and it has been extremely difficult to obtain enough observing time to perform the experiment. The first, complete ultraviolet data set was obtained in 1989 by a large group of IUE observers, who monitored the Seyfert 1 galaxy NGC 5548 for a continuous period of eight months. Much of our understanding of AGN variability is based on this data set.

The main theoretical limitation of the method is the assumption of linearity. While the *total* line and diffuse continua emission of an optically thick gas is indeed proportional to the continuum flux, this is not case for *individual* lines. This is well illustrated in Fig. 8 that shows the response of different emission lines to variations in the ionization parameter. The use of $\Psi(t)$ obtained for a certain line to deduce the gas distribution must therefore be done with great care. In addition, the geometry deduced from the empirical transfer function is not unique, and more information is required to choose among all possible alternatives. Finally, all present day studies make the specific assumption that the observed optical, or ultraviolet continuum variations are proportional to the ionizing continuum variations. This is not necessarily the case and alternatives must also be investigated. Line profiles can provide additional constrains on the gas distribution, as discussed in the next chapter.

8.4. Light Curve Modeling

An alternative empirical way to find the gas distribution, is by fitting models to the observed emission line light curve. This is done by convolving the observed continuum light curve with several assumed transfer functions. The most likely geometry is the one resulting in the best fit to the observed line light curve. The result of this methods is not unique and several different geometries can give satisfactory fits. It can be very useful in eliminating some geometries, and reducing the parameter space. The main limitations are again the uncertain interpolation procedure and the non-linear response of the lines.

8.5. The BLR Size

Having discussed the observations and several potential ways of analysis, we are now in a position to estimate the BLR size. In the time of writing there are only a hand-full of Seyfert 1 galaxies where the cross correlation size has been reliably measured.

The range in luminosity is about 500 and the range in cross correlation size about 25. This incomplete data set, combined with a guess that the average BLR size is about double the cross-correlation size, suggest the following approximate relation for low luminosity AGNs:

$$r_{av} \simeq 0.1 L_{46}^{1/2} pc. \qquad (75)$$

While the $L^{1/2}$ dependence is only a guess at this stage, it is in line with the assumption that the average density and ionization parameter in different BLRs is not a strong function of the continuum luminosity. Further discussion of this relation is given in chapter 10.

8.6. Anisotropic Emission and Beaming

Some bright quasars are known, to vary, by a large amplitude, over short periods of time. These are named OVVs (Optically Violent Variables). They are all radio sources that show some of the characteristics of the BL Lac objects, such as a non-thermal continuum and high degree of polarization. It is believed that relativistic beaming is important in this case, and the objects are seen close to the direction of the beam.

Recent observations show rapid emission line variability in some of these objects, on time scales shorter than estimated from the L - r relations of other AGNs. Since beaming is important, the ionizing flux is highly anisotropic, and line emission from clouds along the beam is much more intense than in other directions. The situation is very similar to the one illustrated in the top half of Fig. 19, where the beam illuminates only a small part of the shell-shaped BLR, and θ is the angle between the beam and the observers' direction. The time lag, $r(1 - \cos\theta) / c$, is short since θ is small.

There are several difficulties with this picture. First, for a double sided beam, there is line emission from the opposite side of the source. Unless it is obscured, this should arrive to the observer at a much later time. No such event has yet been observed. Second, the observed line profiles are usually smooth and symmetric. This is difficult to reconcile with a one-sided, jet-like system, whose center of gravity coincides with the central radiation source. Perhaps other mechanisms, such as radiation pressure (see next chapter), control the shape of the line profile. Nevertheless, beaming is a potentially important process that ought to be studied further since it may play a role in many objects whose ionizing beam is pointed away from us.

8.7 Bibliography

Observations: See chapter 2.

Theory: The first theoretical paper on the subject is by Bahcall, Kozlovsky and Salpeter (1972). More recent and detailed calculations are described in Blandford and McKee (1982). The application of the cross-correlation method to line variability studies is discussed in Gaskell and Sparke (1986) and Robbinson and Perez (1990). The uncertainties in the cross-correlation method are discussed by Gaskell and Peterson (1987), Maoz and Netzer (1989, the CCPD method) and Edelson and Krolik (1989, the Discrete Correlation function). Deconvolution and light-curve modeling are discussed in Maoz et al. (1991).

9. GAS MOTION AND DYNAMICS

The discussion in the previous chapters gave support to the accepted model of AGN emission line regions. Such regions are thought to contain numerous optically thick clouds, that are exposed to the intense ionizing flux of a central source. The origin, stability and motion of these clouds, and the resulting line profiles, are the subjects of this chapter.

9.1 Confined Cloud Models

9.1.1 Important time scales: Several time scales must be considered in relation to the formation, stability and motion of the clouds.

The recombination time: This is the time required to reach ionization equilibrium. It is given by

$$t_{rec} = 1/(\alpha N_e) \simeq 10^{-5} N_{10}^{-1} \; years, \qquad (76)$$

where N_{10} is the density in units of 10^{10} cm^{-3}.

The dynamical time: This is the crossing time (or orbital time) of the line emitting region. For the BLR

$$t_{\rm dyn} = \frac{r_{\rm av}}{\langle v \rangle} \simeq 30 L_{46}^{1/2} \ years, \tag{77}$$

where the previous relation between the average dimension and the luminosity (75) has been used.

The sound crossing time: This is the time required to establish pressure equilibrium within a single cloud. The total cloud thickness is not well determined but the thickness of the ionized gas is estimated to be $10^{12\text{-}13}$ *cm* for the BLR clouds. This gives

$$t_{\rm sc} = R_c / c_s \simeq 2 \times 10^{-12} T_{\rm e}^{-1/2} R_c \ years \tag{78}$$

where R_c is the cloud radius in *cm* and c_s = sqrt[$2kT_e$ / m_p] is the sound speed.

9.1.2 Confinement. The mass of individual BLR clouds, as deduced from the models, is well below their Jeans mass, i.e. self gravity is negligible. In the absence of confinement, such clouds will disintegrate on a time scale of t_{sc}. Since this time is much shorter than the dynamical time, the clouds must be confined or else be continuously produced throughout the BLR, which requires extremely large mass flux through the line emission region.

One way to confine the clouds is by a Hot Intercloud Medium (HIM), much like in the interstellar medium. Such a "two-phase model" has been the subject of extensive investigations. Magnetic confinement is another possibility that needs to be considered. Below is a short description of the hot intercloud medium model.

9.1.3 The two-phase model. In this model the cool ($T_e \simeq 10^4 K$) gas is in pressure equilibrium with a lower density, much hotter gas, of temperature $T_{\rm HIM}$, filling the volume between the clouds. Heating and cooling of the hot gas is mainly by Compton and inverse Compton scattering, and $T_{\rm HIM}$ is given by the Compton temperature

$$T_C = \frac{h\bar{\nu}}{4k}, \tag{79}$$

where $h\bar{\nu}$ is the mean photon energy, weighted by the cross section. In this limit the temperature is independent of the gas density and is determined only by the energy distribution of the incident continuum. As a result, $T_{\rm HIM}$ is the same throughout the line emitting region.

The special feature of the two-phase model is that a single parameter controls the ionization and thermal properties of both components. The parameter, called Ξ is defined by

$$\Xi = const. \times \frac{U}{T_e} \propto \frac{incident\ flux}{N T_e} \propto \frac{radiation\ pressure}{gas\ pressure}. \tag{80}$$

The value of this parameter is the same for the hot and cool gas at a certain location. [6]

The Ξ vs. T_e dependence is the key to the understanding of the two-phase model. At small Ξ the temperature is kept around 10^4 *K* due to bound-free and collisional excitation cooling. At this value of Ξ there is only one solution to the kinetic temperature. At much larger Ξ, the ionization increases, the cooling is less efficient, and no equilibrium can be achieved until Compton cooling become dominant, at about 10^7 - 10^8 *K*. In some cases there is a small range in Ξ where the thermal equilibrium conditions may allow *both* Comptonized gas and low temperature gas to coexist and there is a two temperature solution for the same pressure. This is demonstrated in Fig. 22 that shows the calculated T_e vs. U / T_e curve for two different continua, one with a two phase solution and one without.

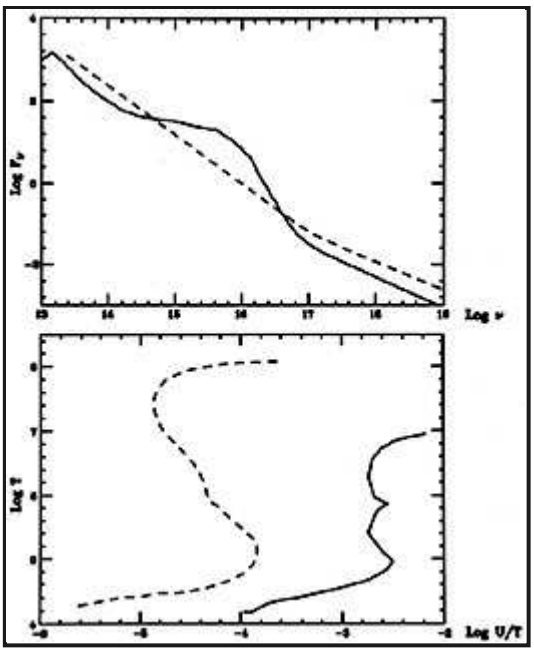

Figure 22. Calculated T_e vs. U/T_e (bottom) for the two incident continua shown in the upper panel. The solid line is the "standard" continuum (Fig.7) adopted in this work. The dashed line is a two-component power-law continuum, with spectral indices of 1.2 in the infrared-ultraviolet and 0.7 in the X-ray. A two-phase solution (S shaped part of the curve) can only be obtained for the power-law continuum (courtesy of T. Kallman)

A two-phase equilibrium can only exist at high enough T_{HIM}, where the T vs. U/T curve is S shaped. In this case there are two stable branches, at low (~ 10^4 K) and high (~ 10^8 K) temperatures, allowing thermal instabilities to grow and develop into a two-component atmosphere. Only one of the continua shown in the diagram (in dashed line) gives this kind of curve. Older photoionization models assumed this continuum to be typical of AGNs. It was consistent with $T_{HIM} \simeq 10^8 K$ and a two-phase model for the gas. Moreover, estimates of the ionization parameter, obtained from emission line ratios, agreed roughly with the U/T required for the two-phase instability. Since this is the only range in which hot and cold gas can coexist, it suggests a specific value of U for the BLR clouds. This was considered to be the explanation for the fact that the ionization parameter in faint Seyferts and bright quasars, a factor of a thousand in luminosity apart, is roughly the same.

Unfortunately, more realistic continua, like the one used throughout this work, changed this result. This continuum has a large ultraviolet excess which results in more Compton cooling. The highest temperature is around 10^7 K, too low to allow a two-phase solution (solid line in Fig. 22). (7) Thus the idea of a stable two-phase BLR, in the form presented here, is questionable. Today it is also known that the allowed range in U is in fact quite large (chapters 4 - 6) and the motivation for a specific value of U is not as strong.

A hot inter-cloud medium with T_{HIM} ~ 10^7 K presents some other problems. First, the optical depth to electron scattering may be large. We can estimate this from the pressure equilibrium condition and the pressure-radius dependence of chapter 5, $P \propto r^{-s}$, with s ~ 2:

$$\tau_{es}(HIM) = \int_{r_{in}}^{r_{out}} \sigma_{es} N_{HIM} dr \simeq \frac{7 \times 10^{-10} r_{in}}{(s-1) T_{HIM}} \simeq \frac{7 \times 10^7 L_{46}^{1/2}}{T_{HIM}}. \quad (81)$$

In making this estimate we have assumed that r_{out} >> r_{in}, the BLR density at r_{in} is 10^{11} cm^{-3}, the temperature of the cold clouds

is 10^4 *K*, and the luminosity-size relation is as in equation (75). This shows that luminous objects, with low T_{HIM}, are opaque to electron scattering. This would have observable consequences. Large amplitude continuum variations will be smeared out and broad electron scattering wings will appear in all emission lines. Moreover, the K-shell opacity in iron and other elements can exceed the electron scattering opacity, and will show up as strong absorption X-ray edges. Such effects are not observed.

There are serious dynamical implications to a cool stationary HIM. Typical velocities in the BLR are several thousands kms^{-1}, much larger than the sound speed in a cool HIM. A super-sonic motion through this medium must result in drag forces, Rayleigh-Taylor instability and breakup of the clouds. This leads to fragmentation into optically thin filaments, in contradiction with the observed strong lines of MgII and FeII. There are additional difficulties and more reasons to abandon the idea of a stable, two-phase model.

The HIM, if it exists, need not be stable. There are additional heating mechanisms, (superthermal particles, radio frequency heating) and the pressure equilibrium may not be exact since cloud evaporation will tend to raise the cloud pressure over the HIM pressure. Line radiation pressure is known to be important in the cold clouds and can exceed the cold gas pressure in cases of a large ionization parameter. A simple pressure equilibrium may not be achieved if this is the dominant pressure inside the clouds. A relativistic intercloud medium can help to solve some of the difficulties, especially the cloud instability problem, since in this case the drag force is very small.

Finally, we should comment on the probable scaling laws for the pressure and density for a stable, or unstable hot confining medium. Using the notation of chapter 5, the value of *s* is likely to be in the range of 3/2 to 5/2, i.e. the assumption of $P \propto r^{-2}$ is quite adequate for such cases.

9.1.4 Magnetic confinement. This is a new idea that has received little attention so far. The field strength required to confine the BLR clouds is about 1 G and its possible origin may be in a relativistic wind, an accretion flow or an accretion driven wind. Magnetically-confined clouds would have a filamentary structure and would tend to elongate along the field lines. The pressure laws expected are $P \propto r^{-5/2}$ in an accretion flow and $P \propto r^{-2}$ in a relativistic wind.

---

[6] Ξ is referred, in some papers, as "the ionization parameter". This should not be confused with *U*, as defined here, which has no temperature dependence. Back.

[7] This temperature may be angle dependent, if the ultraviolet source is a thin accretion disk continuum (chapter 10). Back.

9.2. Other Models

Below is a short account of models not requiring external confinement of the clouds.

9.2.1 Winds. Several wind models have been proposed for the origin and motion of the clouds. The main problem in most of these is the source of the cloud gas. The possibilities of mass loss from giants and from the surface of accretion disks have been considered. In one such model, a hot supersonic wind shocks against some obstacles (supernovae remnants or OB stellar winds) to form clouds in the cooled postshock gas.

9.2.2 Orbiting clouds. Massive clouds, in parabolic orbits, have been proposed for the line emitting gas. The clouds are confined by a central relativistic wind and lose mass as they fall in. Tidal forces break the clouds into smaller fragments, at about 1 pc. Such clouds are assumed to produce observed line emission at all distances, from 1 kpc to 0.lpc. The line core is produced at large distances, where the velocities are small, and the line wings are produced by fragments, at the standard BLR distance.

9.2.3 Disks. There have been several models relating the line emission to the central, hypothetical accretion disk (chapters 5). Such a configuration provides a large amount of cool gas that needs no external confinement, and can produce line emission provided a suitable energy mechanism exist. Standard thin accretion disk models suggest that the temperature and the flux emitted by the disk, at the typical BLR distance, are too low to be observed. Thus an additional heating source for the gas is required. As explained in chapter 5, this can be achieved if part of the central continuum radiation is back-scattered onto the disk surface at large radii (Fig. 13).

9.2.4 Stars. Stellar atmospheres have been proposed for the BLR clouds. Given the size and density of the broad line clouds, these must be giant size atmospheres. Stellar atmospheres require no confinement, which is the main virtue of this model. The difficulty is the large number of giants (~ 10^7) needed to explain the observed covering factor in BLRs. Given a normal stellar population, the total cluster mass is enormous and can dominate the dynamics near the center. It has been suggested that

radiation pressure driven winds, or accelerated stellar evolution, keep the required number of stars small.

If BLR clouds are indeed stellar atmospheres, the density and pressure profiles may be very different from the ones assumed so far. The implications to the line intensity, variability and profiles are still to be investigated.

9.3. Observed Line Profiles

The large diversity in line profiles has already been demonstrated in chapter 2 and several more examples are given in Fig. 23. The broad line profiles of many objects are smooth and symmetric. Their shape is well fitted, in many cases, by a logarithmic function ($E_\lambda \propto$ -log $|\lambda - \lambda_0|$, see Fig. 23). Profile differences can be large or small. There are cases of almost identical profiles for lines of very different excitation. A likely explanation here is that the emission line spectrum of all clouds is the same. There are opposite examples too, and a clear trend is still to be found. It has been claimed that the high excitation lines are systematically broader than the low excitation lines, but there are definitely some exceptions to that. One common trend is observed between the $H\alpha$ and $H\beta$ line profiles, where the latter is relatively stronger away from the line center (see diagram). Another trend is for the $HeI\lambda$5876 line to be somewhat broader than $H\beta$.

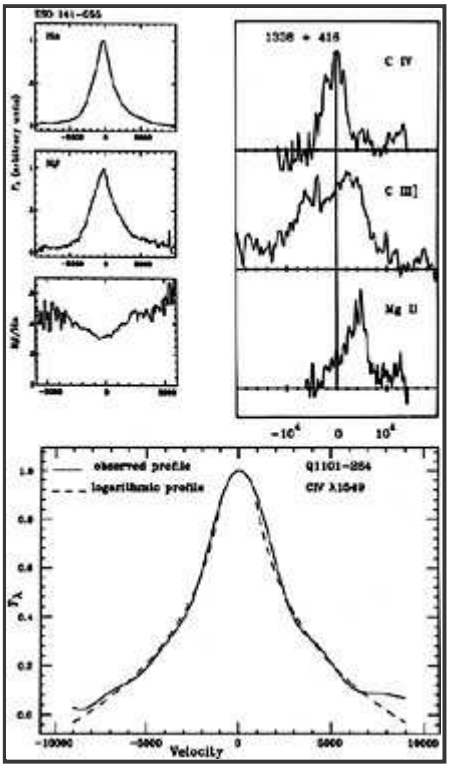

Figure 23. Observed broad line profiles. Bottom: A symmetric $CIV\lambda$ 1549 line (solid curve) fitted with a logarithmic profile (dashed line)(courtesy of B. Wilkes). Top left: $H\alpha$, $H\beta$ and their ratio, showing the larger width of $H\beta$ (courtesy of G. Stirpe). Top right: Emission line redshift differences (Corbin 1990).

Broad, asymmetric lines are seen in many objects, but no clear tendency for the blue or the red wing to be stronger. Some line profiles are bumpy, and their shape varies in time. The best known examples are some steep spectrum radio sources whose line profiles are extremely broad and disturbed. It has been suggested that the lines are emitted in an edge-on, disk-like system, with axis parallel to the direction of the radio jet.

Finally, there is a clear tendency for the high excitation lines in luminous AGNs to be systematically blue-shifted relative to the low excitation lines. The effect can be large, up to 3000 $km\ s^{-1}$, and seems to increase with luminosity. The few detailed studies of this phenomenon suggest that the systemic redshift is given by the low excitation lines. An example is shown in Fig. 23.

As for the narrow lines, the profiles are smooth with a clear tendency for the blue wing of some lines to be stronger. The blue asymmetry is most noticeable in lines of higher excitation and/or critical de-excitation density. This part of the line originates in high density, fast moving NLR clouds. The phenomenon is observed in most Seyfert 1 and Seyfert 2 galaxies.

9.4. Theoretical Line Profiles

9.4.1 Radial forces. We consider the general case of small clouds, moving through a confining medium. The radial motion of a cloud is determined by the gravitational acceleration, g_G, the radiative acceleration, g_{rad}, due to the absorption of the central continuum radiation, and the drag force, f_d. The equation of motion is:

$$\frac{dv}{dt} = -g_G + g_{\rm rad} + \frac{f_d}{M_c}. \qquad (82)$$

The radiation acceleration can be treated in a very general way by noting that the clouds are in ionization and thermal equilibrium. Energy conservation implies that the absorption of a photon of frequency ν is associated with cloud emission (all lines and diffuse continua) of $h\nu$. The momentum transfer to the cloud, per unit time, is $h\nu$ / c. Thus, the radiative accelerating force is proportional to the total cloud emission. In the notation of chapter 5, the cloud emission is $j_c(r)$, the mass of the cloud is M_c, and the radiative acceleration is proportional to $j_c(r)$ / M_c.

We shall now be more specific about radiative acceleration. Consider first a fully ionized gas and assume, for simplicity, the pure hydrogen case. The mean energy of an ionizing photon is $h\bar{\nu}$ and there are αN_e^2 ionizations and recombinations per unit volume and time, each associated with a momentum transfer of $h\bar{\nu}$ / c to the cloud. We neglect the absorption of non-ionizing continuum photons and line photons. The radiative acceleration is

$$g_{\rm rad}(r) = \frac{h\bar{\nu}}{c}\frac{\alpha N_e^2}{m_p N_e} = const. \times N_e, \qquad (83)$$

where m_p is the proton mass and we have neglected the temperature dependence of the recombination coefficient α. Thus, theradiation acceleration of a fully ionized gas is proportional to the gas density and practically independent of the column density. (This is identical to the previous result since $j_c(r) \propto N_e^2 V_c$ and $M_c \propto N_e V_c$, where V_c is the volume of the cloud.)

The other extreme situation is the case where all the ionizing flux is absorbed by an optically thick cloud. Here the amount of flux absorbed is proportional to the cloud cross section, $A_c(r)$, and

$$g_{\rm rad}(r) = \frac{A_c(r)}{cM_c}\int_{\nu_0}^{\infty}\frac{L_\nu}{4\pi r^2}d\nu. \qquad (84)$$

The properties of realistic clouds must be between these two cases. The ultraviolet radiation is absorbed in the fully ionized part and the harder radiation in the neutral zone. In particular, the cloud must be transparent at some frequency and the amount of momentum absorbed depends on the column density. It can be shown that the acceleration associated with the absorption of X-ray photons is proportional to $1/R^2_c(1 + N_{col} / N_0)$, where $N_0 \simeq 2 \times 10^{20}\ cm^{-2}$.

Finally, the drag force exerted on a radially-moving cloud, depends on the cross-sectional area, the intercloud medium density and the relative velocity between the cloud and the intercloud medium.

Given a typical AGN continuum, we find, for optically thin gas,

$$\frac{g_{\rm rad}}{g_G} \simeq 20 N_{10}\frac{r_{18}^2}{M_9}, \qquad (85)$$

where $r_{18} = r / 10^{18} cm$ and $M_9 = M_{BH} / 10^9\ M_\odot$. This ratio is larger than unity even for very large M_{BH}, and in the absence of strong drag forces, the radial motion of optically thin clouds is governed by outward radiation acceleration. As for optically

thick clouds, g_{rad} / g_G depends on the density and column density of the clouds and must be calculated for the given situation.

9.4.2 Pancake clouds. If clouds move radially through an intercloud medium, their shape and optical depth will be modified. Detailed calculations show that fully ionized, low mass clouds, approach a nearly spherical shape as they move out under the influence of radiation pressure acceleration. More massive clouds adopt a "pancake" shape, having much larger dimensions perpendicular to the direction of motion. This has important consequences to the emission line spectrum since relative line strength may depend on the cloud location. Moreover, not all clouds are accelerated outward and those that form closer in, where the ambient density is larger, may fall in under the influence of gravity. The net result is that the simple approximation adopted for $A_c(r)$ in chapter 5 may not be valid in such cases. There are additional implications to the line profiles, as discussed below.

9.4.3 General line profiles. Consider a spherical system of isotropically emitting clouds, with a number density $n_c(r)$ and emission per cloud $j_c(r)$. We further assume that all of the cloud emission is represented by a *single emission line*. The wavelength dependence luminosity ("profile") in a line of rest wavelength λ_0 is

$$E_\lambda = 2\pi \int_{r_{in}}^{r_{out}} \int_{-1}^{1} n_c j_c r^2 \delta[\lambda - \lambda_0(1 + v\mu/c)] d\mu dr, \tag{86}$$

where $\mu = \cos\theta$ in a spherical coordinate system with its z axis parallel to the line of sight. Integration over the δ-function gives $c/v\ \lambda_0$, provided $0 < |\lambda - \lambda_0|\ c/\lambda_0 < 1$.

We now make the simplifying assumptions of pure radial motion and a constant mass flow (mass conservation),

$$\dot{M} = 4\pi r^2 n_c M_c v(r) = \text{const.} \tag{87}$$

All clouds are assumed to form near r_{in} and experience a radial acceleration of $g(r) = vdv/dr$. Substituting into the line profile equation we get,

$$E_\lambda = \frac{\dot{M}_c}{2\lambda_0} \int_{v_1}^{v(r_{out})} \frac{j_c}{g(r) M_c} \frac{dv}{v}, \tag{88}$$

where v_1 is the largest of $v(r_{in})$ and $|\lambda - \lambda_0|\ c/\lambda_0$. The line profile is logarithmic, $E \propto \log(|\lambda - \lambda_0|)$, in those cases where j_c / $g(r)M_c$ is constant. Assuming mass conservation (87) this is equivalent to the following condition:

$$r^2 n_c j_c \propto \frac{dv}{dr}. \tag{89}$$

9.4.4 Line profiles for radiatively driven clouds. The general argument about the relation between the amount of radiation absorbed and the rate of momentum transfer (beginning of 9.4.1) suggests that in this case the radiative acceleration is proportional to j_c / M_c. Thus if the radiation pressure force is the dominant force, the line profile has a logarithmic shape. Below we demonstrate this for the two extreme cases considered earlier.

In the optically thin case, $j_c \propto V_c N_e^2$, $M_c \propto N_e V_c$ and $g_{rad} \propto N_e$. Thus j_c / $g(r)M_c$ = *const.* and the line profile is logarithmic. In this case, the radial velocity at a distance where the density is N is approximately

$$v(r) \sim (Nr)^{1/2} \propto N^{1/2} L^{1/4}, \tag{90}$$

where we have used the previously obtained radius-luminosity relation (75). With the estimate of g_{rad} / g_G (85), and the known density in the BLR, it can be shown that velocities of more than 10,000 *km* s^{-1} can be obtained.

As for the optically thick case, the radiative acceleration is given by Eqn. (84) and the cloud emission by

$$j_c = A_c(r) \int_{\nu_0}^{\infty} \frac{L_\nu}{4\pi r^2} d\nu. \tag{91}$$

Thus, j_c / $g(r)M_c$ = *const.* and we recover the logarithmic line profile. Note again the assumption that all emission comes out in one emission line (or is divided among all lines in the same way at all distances) which is crucial for obtaining this particular line profile.

9.4.5 General logarithmic profiles. The conditions for a logarithmic line profile can be investigated in a more general way, using the radial dependences of the cloud parameters. Adopting Eqn. (89) as the basic requirement for a logarithmic shape, and the previous parametric descriptions, $n_c(r) \propto r^{-p}$, $A_c(r) \propto r^{-q}$ and $v(r) \propto r^{-t}$, we get the following requirement for a logarithmic line profile:

$$p + q + m - t = 3. \tag{92}$$

The line emissivity parameter, m, is approximately 2 for many emission lines, so an almost as general requirement is

$$p + q - t = 1. \tag{93}$$

As an example, consider infalling optically thick clouds, no radiation pressure and no drag force. Here t = 1/2 and mass conservation requires that 2 - p = t or p = 3/2. Logarithmic line profiles will result if q = 0 (also s = 0), i.e. constant radius clouds, In the two-phase scenario, this means a constant confining pressure throughout the emission line region.

The s = 0 situation is illustrated below in more detail for a few velocity laws and complete photoionization models. The models are similar to the ones described in chapters 4 and 5, except that in this case the cumulative line fluxes are calculated with the assumption of a constant confining pressure and a constant gas density, s = 0. These integrated fluxes, as a function of r, are shown in Fig. 24.

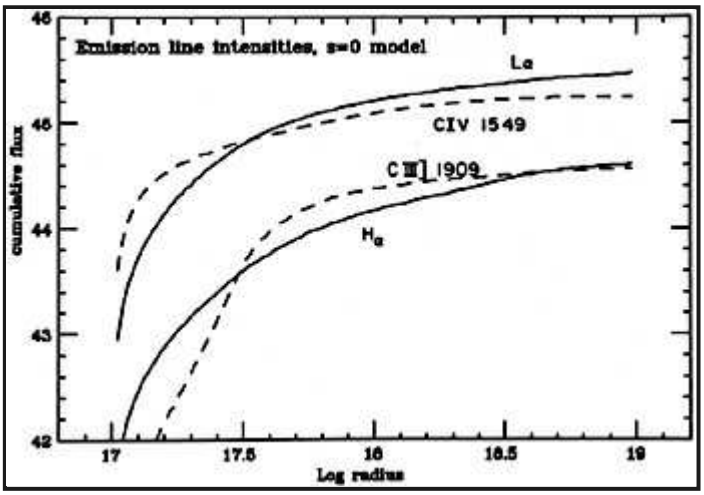

Figure 24. Cumulative line fluxes, as a function of the outer radius, for a photoionization model with s = 0 (constant confining pressure) and $N = 10^{10} cm^{-3}$. The normalization of the model is such that U = 0.1 at $N_{col} = 10^{23.5}\ cm^{-2}$.

Line profiles for this cloud system have been calculated under several different assumptions. The first case is a decelerating outflow, with isotropic line emission and $v \propto r^{-1/2}$. This velocity law satisfies the condition for a logarithmic profile (93) as is evident also from the $L\alpha$ profile shown in Fig. 25. The profile is very similar to the $CIV\lambda 1549$ profile shown in Fig. 23, except for the flat top, which is the result of the finite r_{out} used (i.e. no low velocity material). A flat-topped profile is a signature of radial flow motions with a weak v/r dependence and/or a small r_{out} / r_{in}. In the particular case shown here, the requirement for lines with smooth wings between 200 and 10,000 $km\ s^{-1}$, implies r_{ont} / r_{in} > 2500. This is an extreme and unrealistic ratio for the BLR.

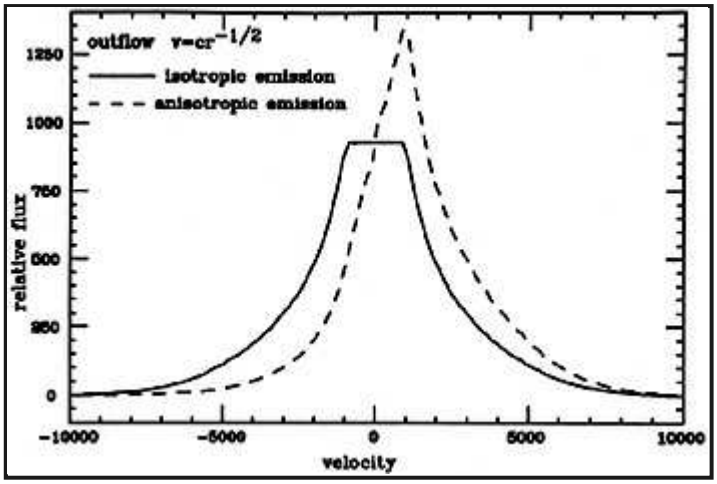

Figure 25. $L\alpha$ profiles obtained by integrating the line emission in the photoionization model of Fig. 24 with the velocity law indicated. Solid line: isotropic $L\alpha$ line emission. Dashed line: anisotropic line emission (90% of the photons escape from the illuminated surface).

A major uncertainty is the dependence of the cloud cross-section on r. It depends on the (hypothetical) inter-cloud medium and the velocity law and may be very different from the simple r^{-q} parametric dependence assumed here. In pancake clouds, which is about the only case that was studied in detail, A_c has a complicated radial dependence. Such clouds may be optically thin around their edge and their column density changes continuously throughout the motion. Needless to say, the resulting line profiles must be calculated with great care, taking the real emissivity into account.

9.4.6 Orbital and chaotic motion. Chaotic (random orientation) cloud motion can produce line profiles that are in good agreement with some observations. Orbital motion can give good agreement too, at least for some emissivity laws. For example, it has been suggested that the BLR clouds are moving in parabolic orbits, with some net positive angular momentum. Reasonable assumptions about the distribution of clouds in angular momentum require that the cloud density be given by $n_c(r) \propto r^{-1/2}$. Making the additional assumption of constant confining pressure (no change of the cloud cross section with r) we obtain $j_c(r) \propto r^{-2}$ which, upon substituting into the line profile equation (86), gives:

$$E_\lambda \propto \int_r n_c j_c r^2 v^{-1} dr \propto \int_v v^{-3} dv \propto (\lambda - \lambda_0)^{-2}. \qquad (94)$$

Such profiles seem to fit nicely the far wings of many lines. Thus there is more than one dynamical model that can explain the observed profile.

As for the accretion disk model, in this case the motion is in a plane and a characteristic profile, made up of two humps and a central dip, results. The relative intensity of the profile components depends on the emissivity as a function of r and the size of the disk. Small disks would tend to give a large central dip, while in very large ones the dip is filled by emission from the outer, slowly rotating gas.

A few AGNs show disk-type line profiles and it has been suggested that this is a common phenomenon, except that the central dip in most other cases is filled in by emission from low velocity material, The distance of the low velocity material can be calculated, given the central mass. In some cases it is way beyond the outer boundary of the BLR, and may be inside the NLR. Such outer parts are well beyond the self gravity radius of a thin, radiation pressure supported accretion disk (chapters 5 and 10).

Much of the effort in fitting AGN line profiles by thin disk models has focused on the Balmer hydrogen lines in BLRGs. The specific disk models used are the ones discussed in chapter 5, where the low excitation lines are the result of back-scattering of the X-ray radiation onto the surface of the disk, at large radii. Such models predict little or no high ionization line radiation from the disk and it remains to be seen whether the observed $L\alpha$ and $CIV\lambda 1549$ lines are indeed different from the $H\alpha$ and $H\beta$ line profiles in those objects.

9.4.7 Line asymmetry and wavelength shifts. All examples so far considered assume isotropic line emission. This is not necessarily the case for lines whose optical depth structure, within the cloud, is nonuniform. The most notable example is $L\alpha$, whose optical depth is very different in the ionized and neutral parts. Most of the emitted $L\alpha$ photons escape through the illuminated cloud surface, and the radiation emitted in the outer direction is almost totally absorbed. Photoionization calculations predict that in a plane-parallel geometry, more than 95% of the broad $L\alpha$ emission is emitted from the illuminated surface of the clouds. The effect is smaller, but not negligible, in other broad lines such as $H\alpha$, $H\beta$ and $MgII\lambda 2798$.

Another example of anisotropic line emission is obscuration by dust. The intercloud medium may be dusty, causing line emission from the farther hemisphere to be fainter. Alternatively, the dust may be embedded in the clouds, mainly in the neutral part. The line emission from the back side of the clouds (the side away from the ionizing source), is weaker in this case. This is a likely situation in NLR clouds.

Anisotropic line emission has a direct consequence on the observed line profile of radially moving clouds. It introduces a profile asymmetry whose magnitude depends on the degree of anisotropy and the velocity pattern. For example, in outflow motion the $L\alpha$ profile would show a strong red asymmetry (red wing stronger than blue wing). A similar asymmetry is obtained for outflowing dusty clouds, whose dust particles reside in the back of the clouds. An outflow motion through a dusty intercloud medium gives a blue asymmetry. Fig. 25 shows the broad $L\alpha$ profile resulting from the outflowing $s = 0$ atmosphere, when the $L\alpha$ anisotropy is taken into account. The strong red asymmetry is clearly visible in this case.

Asymmetric broad line profiles are indeed observed in some cases, but in many AGNs the line profiles, including $L\alpha$, are quite symmetric. There are several possible explanations for this. The first and most obvious one is that there is little, if any, radial motion of BLR clouds. There are other evidences (section 9.5) to support this claim. Alternatively, some of the $L\alpha$ emission may originate in outflowing (or infalling) optically thin clouds, whose emission pattern is much more isotropic. The obvious difficulty is the presence of strong, low excitation lines, that require large neutral hydrogen column densities. Pancake shaped clouds have a variable column density, and may be thin along their rim. This helps to reduce the profile asymmetry in a radially moving system.

An alternative explanation for symmetric line profiles in a radially moving system is the presence of some scattering material in the vicinity of the clouds. The scatterers may be the hot electrons in the HIM or dust particles in the NLR. The main cause of asymmetry is the weak flux from the hemisphere nearer to the observer and there are several ways by which this can change in the presence of scatterers. First, the scattered ionizing radiation can hit the back, neutral side of the clouds, producing more ionization and line emission. Second, if the intercloud medium is optically thick, the radiation observed from the farther hemisphere is reduced. Third, the inward emitted line photons in the near hemisphere can be scattered back into the line of sight. Fig. 26 shows two $L\alpha$ profiles, resulting from the same cloud system as before, but moving in this case through a Compton thick HIM. The line profiles are calculated for the cases of $\tau_{es} = 0$ and $\tau_{es} = 2$, and the latter is indeed more symmetric.

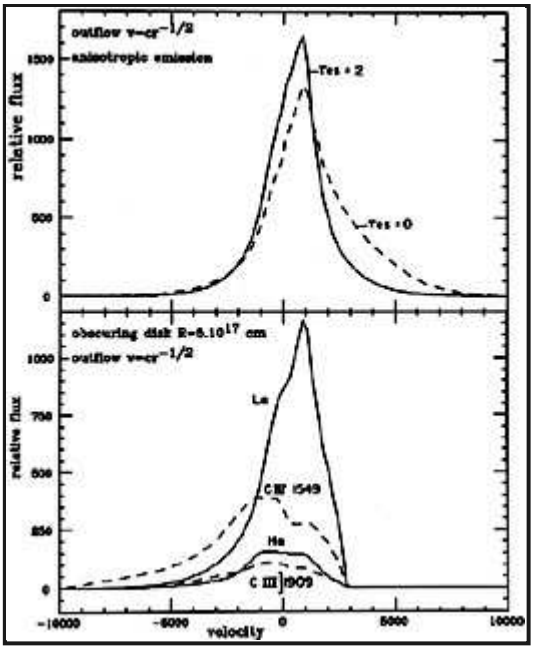

Figure 26. Top: Unnormalized $L\alpha$ profiles for the s = 0 outflowing atmosphere, showing the effect of a Compton thick medium. The $L\alpha$ emission from the clouds is highly anisotropic but the line asymmetry is reduced, compared to the Compton thin case, due to scattering related effects. Bottom: The same, model, with τ_{es} = 0, combined with a central obscuring disk of radius 5×10^{17} *cm*. Note the wavelength shift of the line centers.

The wavelength shift of some broad lines in high luminosity AGNs is definitely of great significance. In the time of writing there is no satisfactory explanation for this. One idea is that the shift is caused by a combination of obscuration and outflow motion. Consider for example a decelerating outflow around a large accretion disk, with *U* decreasing outward. The high excitation lines, like $CIV\lambda$1549, are formed near the disk and much of their red-wing (emission from the other side of the disk) is not observed. Lower excitation lines, such as $MgII\lambda$2798, are produced further away from the disk, where the obscuration is smaller. Their central wavelength is closest to the "true" redshift. An illustration is shown in Fig. 26. This is the same s = 0 outflow model as before but this time with a central obscuring disk of radius 5×10^{17} *cm*. Some wavelength shift between $L\alpha$, $CIV\lambda$1549 and $H\alpha$, is indeed observed, but all lines are asymmetric and the velocity difference is small. A more complex situation, of outflow combined with a flat rotating system whose low ionization lines are predominately from material in the plane of the disk, may give a better match to the observations.

9.5. Cross-correlation Tests

The correlated line and continuum variability provides an additional, powerful test on several of the assumptions made here. Consider a radially moving system of clouds. The emission line light curves of the *blue* and the *red* wings of the lines represent the emission from the near and the far hemispheres. These are very different, because of the different distance to the observer. The response of the near hemisphere is almost immediate, with sharp features, while the the far hemisphere is an average over a longer time, with smooth, features.

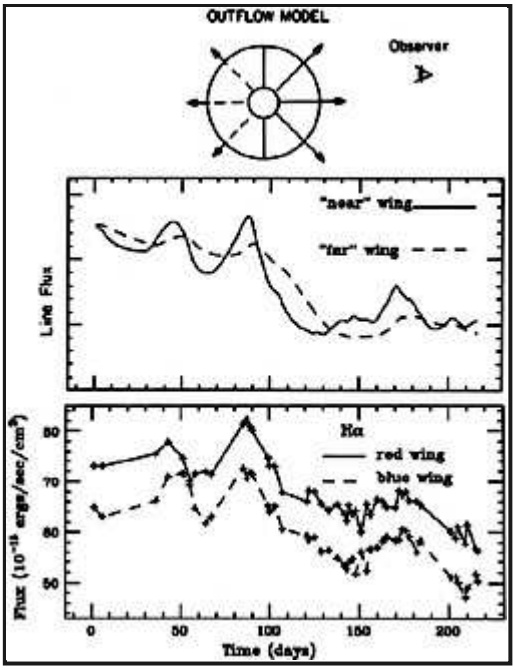

Figure 27. Top: A schematic representation of a spherical outflowing system of clouds. Middle: Theoretical blue and red wing light curves obtained by assuming constant emission per unit covering factor, and the continuum light curve of NGC 4151 (Fig. 17). Bottom: Observed light curves for the blue and red wings of $H\alpha$. (Maoz et al. 1991).

The situation is illustrated in Fig. 27. for the case of NGC 4151 discussed in chapter 8. The top part of the diagram shows theoretical blue and red wing light curves, given tile variable continuum of this source (Fig. 17). This should be compared with the measured light curves of the blue and red halves of the $H\alpha$ line, shown in the lower panel. The difference between the model and the observations is very large indeed: The measured red and blue wing light curves are identical, within the errors (and their cross-correlation gives a zero time lag) and do not resemble the theoretical curves. This suggests that a radial gas motion can be ruled out at a high confidence level, in this source.

Variable line profiles are important since they provide a way for mapping out the velocity field in the BLR. In principle, the transfer function should be constructed for each velocity, and a full 6-dimensional phase-space analysis should be performed. Obtaining profile information at each phase of activity is even more difficult than following the light curve behavior, and at time of writing no such analysis has been carried out.

9.6. Bibliography

The two-phase model: The basic paper is by Krolik, McKee and Tarter (1981). Other detailed papers on this topic are by Lepp et al. (1985), and Kallman and Mushotzky (1985). Krolik (1988) has discussed transient cool clouds embedded in hot gas. The difficulties with the model, especially in relation to the hot medium temperature, are discussed by Fabian et al. (1986) and Mathews and Ferland (1987). The last reference addresses the dynamical implications in great detail. For cloud formation, in relation to thermal instability, see Mathews and Doane (1990).

Other models: Magnetic confinement is discussed in Rees (1987). Cloud formation in winds is discussed by Smith and Raine (1985), Perry and Dyson (1985, winds and obstacles) and Shlosman et al (1985, radiation pressure driven wind from the surface of a disk). Collin-Souffrin, Dyson, Dowell and Perry (1988) suggested a two component model for the BLR, including high ionization broad line clouds, and the outer parts of a central accretion disk. More on accretion disks as a source of line emission can be found in a series of papers by Collin-Souffrin, Dumont and collaborators (See Dumont and Collin-Souffrin 1990 and references therein). The orbiting cloud model has been suggested by Kwan and Carroll (1982), Carroll and Kwan (1985) and Carroll (1985). The implications to the NLR are discussed in Carroll and Kwan (1983). Critical discussions of these and other models are given in review articles by Mathews and Capriotti (1985) and Osterbrock and Mathews (1986). BLR models involving stars are discussed by Voit and Shull (1988), Penston (1988), Kazanas (1989) and Scoville and Norman (1988).

Line profiles: For line profile observations see chapter 2. The basic work on acceleration by radiation pressure is by Mathews (1974, 1982a) and Blumenthal and Mathew (1975, 1979). These authors have also investigated the shape of the clouds, in particular "pancake" clouds. Different radial dependences are discussed by Capriotti et al (1980, 1981), Carroll and Kwan (1983, 1985), Bradley and Puetter (1986) and Penston et al. (1990). Shields has investigated disk line profiles in a number of papers; see Shields (1989) for references. More work on disk-type profiles is in Mathews (1982b). Application of disk profiles to the case of Arp 102B are discussed in Chen et al. (1989). For reviews see Mathews and Capriotti (1985), Osterbrock and Mathews (1986) and Shields (1989).

Line asymmetry and wavelength shifts: The first theoretical discussion of line asymmetry is by Ferland, Netzer and Shields (1979). Further work is by Capriotti et al. (1981) and Puetter and Hubbard (1987). Kallman and Krolik (1986) investigated line profiles in a presence of a Compton thick medium. For the observations, see chapter 2.

Cross-correlation tests of radial motion: See Maoz et al. (1991) and references therein.

10. Line and Continuum Correlations

So far we have only considered line intensities and line profiles in individual objects. More insight on AGNs can be gained by comparing different objects, and by analyzing the statistical properties of large samples. It enables us to search for luminosity dependences, to compare bright and faint objects in a variety of ways, and to examine the consequences of the photoionization theory.

In this chapter we discuss several observed correlations between the broad emission lines and the nonstellar continuum of AGNs. We use them to obtain further estimates on the ionization parameter, the covering factor, the velocities and the masses of AGNs. Thin accretion disks are also discussed. A parallel discussion, based on observations of the narrow lines, is given in chapter 11. Throughout the chapter we use the symbol L to designate the integrated continuum luminosity over some specified frequency range, and L_λ the monochromatic luminosity per Å.

10.1. Line Intensity vs. Continuum Luminosity

The intensity of most broad emission lines is strongly correlated with the continuum luminosity. An example is shown in Fig. 28, where the L_α intensity of 328 AGNs is compared with their continuum luminosity. An almost perfect correlation, with a best slope of 0.88, is found. This gives further support to the idea that photoionization is, indeed, the main source of excitation for the lines.

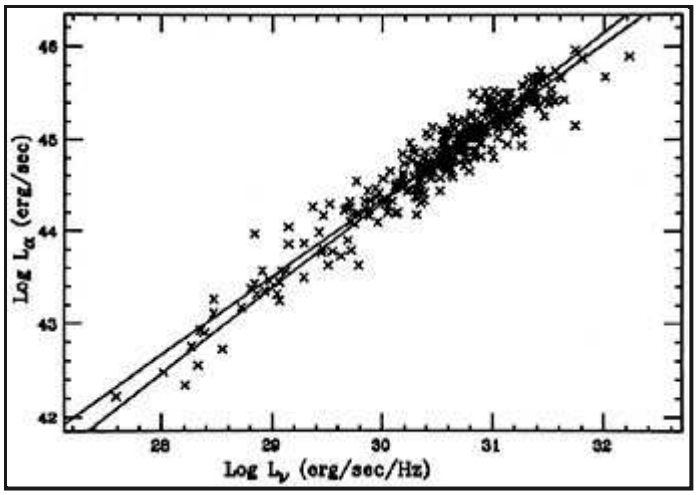

Figure 28. L_α luminosity vs. continuum luminosity for 328 AGNs. (Here and in the following examples $H_0 = 75\ km\ s^{-1}\ Mpc^{-1}$ and $q_0 = 0.5$).

The slope of the correlation in Fig. 28 is close to, but not exactly 1.0. This can be interpreted in several ways. One possibility is that the integrated covering factor decreases with increasing luminosity. If this is correct, and there are no other factors involved, then the decrease in covering factor amounts to a factor of about 3.5 over the range of $10^{4.5}$ in continuum luminosity. Another possibility is a change in the shape of the ionizing continuum, such that the number of ionizing photons (mainly in the 1-4 Ryd.

range), compared with L_{1215}, is smaller in brighter objects; i.e. a softer ionizing continuum in more luminous objects. The change must be small, as the relative intensity of the high excitation lines does not seem to be a function of luminosity. There are other possibilities, such as changes in the amount of the optically thin material and/or the optical depth of the clouds, with luminosity.

10.2. Line - Line Correlations

Emission line ratios are the best ionization parameter indicators, and the correlation of line ratios with the continuum luminosity can be used to check the *U* vs. *L* dependence.

Fig. 29 shows the *CIV*λ1549 / *L*α line ratio, as a function of the continuum luminosity, for a sample of 165 AGNs. The scatter in this ratio is large, but the tendency is for the line ratio to decrease with increasing continuum luminosity. This indicates, perhaps, that the ionization parameter in bright quasars is smaller than in Seyfert 1s (Fig. 8). Although the correlation is statistically significant, it is not clear how representative it is of the AGN population. The objects under study were randomly selected from the literature, and there are several potential selection effects to be considered. Moreover, despite the tendency of decreasing *CIV*λ1549 / *L*α with increasing luminosity, some bright quasars are definitely exceptional in this respect.

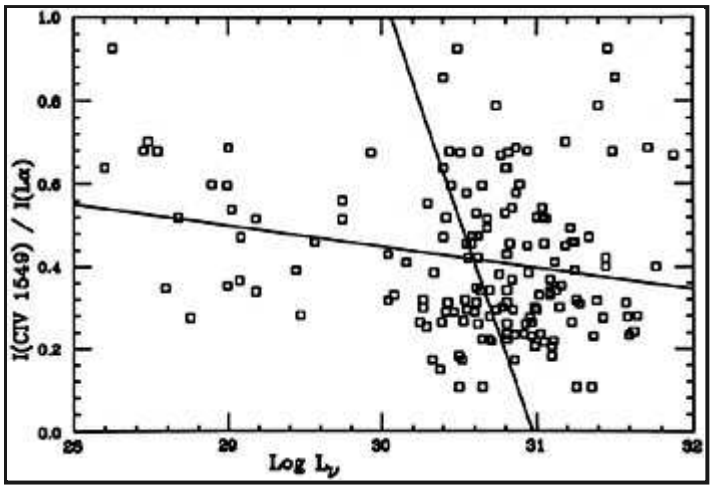

Figure 29. *CIV*λ1549 / *L*α vs. continuum luminosity at 1549Å for 165 AGNs.

Line ratio diagrams have been constructed for other emission lines, some in carefully selected samples, where selection effects are not likely to dominate. Such well selected samples are rare, and the number of objects in them rather small. They cover a limited range in luminosity, and general tendencies are hard to discover. Of the more interesting findings we note the increase of the *CIII]*λ1909 / *CIV*λ1549 line ratio with *L*, suggesting, perhaps, a change in *U* and/or density with luminosity.

10.3. Line Width vs. Continuum Luminosity: M/L for AGNs

10.3.1 Observed correlations. A superficial study of AGN spectra reveals the large diversity in line widths. The FWHM (Full Width Half Maximum) of a certain line, in objects of similar continuum luminosity, can differ by a factor of two or more. For example, the typical FWHM in radio-quiet Seyfert 1s is about 4000 *km* s^{-1}, while in radio-loud Seyfert 1s (the BLRGs), with similar continuum luminosity, it can exceed 10,000 *km* s^{-1}. Extremely broad emission lines seem to be typical of steep spectrum radio quasars. Many of these objects show also a bumpy, asymmetrical line profile.

The *CIV*λ1549 FWHM versus L_{1549} correlation is shown in Fig. 30. There is a weak tendency for brighter objects to have somewhat broader lines which, for the data in the diagram, is expressed by

$$FWHM(CIV\,\lambda 1549) \propto L_{1549}^{0.3}. \qquad (95)$$

The correlation is noisy and only marginally significant. More important, the above sample, which was collected from published line lists, does not include the BLRGs. Having a few such objects in the sample would increase the average FWHM at the low luminosity end, causing the above correlation to weaken, or disappear.

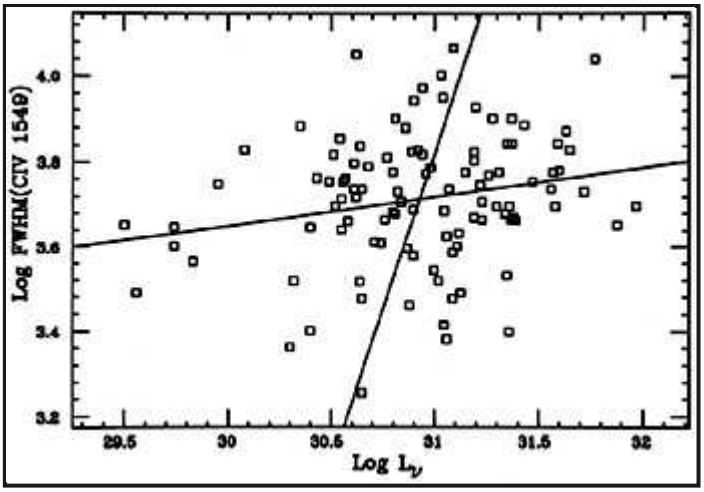

Figure 30. The FWHM of $CIV\lambda 1549$ vs. continuum luminosity at 1549Å for 104 AGNs.

This and several published line width vs. *L* correlations, are all affected by the lack of well selected samples. It will take more observational effort, and better defined samples, to verify whether or not the line-widths are indeed correlated with the continuum luminosity. Since no firm conclusion can be drawn at this stage, we proceed by examining the consequences of two likely possibilities: FWHM independent of *L* and FWHM $\propto L^{1/4}$.

10.3.2 M/L for AGNs. Assume that the emissivity weighted radius, r_{av} in (71), is the typical dimension of the BLR. Assume further that the Keplerian velocity at r_{av}, measured in units of 3000 *km* s^{-1}, is

$$v_{3000} = \sqrt{3}/2FWHM. \tag{96}$$

For a bound Keplerian motion around a central mass *M*,

$$M \simeq 7 \times 10^{-10} v_{3000}^2 r_{av} M_{\odot}, \tag{97}$$

and from the definition of the ionization parameter (5)

$$r_{av} \simeq 3.5 \times 10^{17} \left[\frac{L_{46}(ion)}{U N_{10} \bar{\nu}} \right]^{1/2} \ cm, \tag{98}$$

where $L_{46}(ion)$ is the ionizing luminosity in 10^{46} *erg* s^{-1}, $N_{10} = N/10^{10}$ cm^{-3} and $\bar{\nu}$ the mean energy of an ionizing photon, in Rydberg.

Assume now $U \propto L^a$, $v_{3000} \propto L^b$ and $(N_{10}\,\bar{\nu})$ which is independent of *L(ion)*. Thus

$$M = M_1 [L_{46}(ion)]^{2b+0.5(1-a)}. \tag{99}$$

The previous estimate of r_{av} (75) obtained from line reverberation studies, combined with typically observed FWHM, enable us to estimate that for Seyfert 1 galaxies $M_1 \sim 10^9 M_{\odot}$.

The value of *a* is not well known, but it is likely to be in the range 0 to -1/2. For the case of $a = 0$ (*U* independent of *L*) there are two interesting possibilities: $b = 0$ (line width independent of luminosity), which results in $M \propto L^{1/2}$, and $b = 1/4$, that gives $M \propto L$.

The accretion rate $\dot{m}$, expressed in units of L / L_{Edd}, is proportional to L / M ,

$$\dot{m} \propto L/L_{\rm Edd} \propto L^{-2b+0.5(1+a)}. \qquad (100)$$

With the above estimate of M_1 we find $L / L_{\rm Edd} \simeq 0.05$, which is in the general accepted range for thin accretion disks. The estimates are still u ncertain and more measurements are needed to establish the values of a, b and M_1.

If radiation pressure is the major driving force of the clouds, the velocity field and *L/M* are somewhat changed. For example, in the optically thin outflow case, the acceleration is proportional to N_e and the velocity, at a distance r, is proportional to $(Nr)^{1/2}$. Assume that the measured FWHM is associated with a terminal velocity v_{3000} at a distance $r_{\rm av}$, where the density is the "typical" BLR density. In this case $v_{3000} \propto r_{\rm av}^{1/2} \propto L^{1/4}$ and the *M/L* dependence is similar to the Keplerian case (99) with b = 1/4 and somewhat smaller M for a given L (the velocity at $r_{\rm av}$ is larger, for a given M, than the corresponding Keplerian velocity). The optically thick acceleration case is more complicated, but the $v \propto r^{1/2}$ dependence is quite general.

10.3.3 Line width and radio properties. The radio emission of AGNs is observed to come from either a compact or an extended radio source. The compact source coincides with the optical continuum source. Its radiation is thought to be beamed, due to relativistic motion, and its apparent luminosity depends on the observer's viewing angle. The extended radio emission originates in a much larger volume, it is not beamed and the apparent luminosity is angle independent. Thus the ratio of the compact and extended radio fluxes is a measure of the orientation of the central radio source. This ratio (compact/extended) is found to be *smaller* in objects with *broader* emission lines. This may influence all line-width vs. continuum luminosity correlations in samples including radio-loud objects. It suggests that the emission lines in those radio-loud objects are emitted, preferentially, from material in a plane perpendicular to the direction of the radio beam, which may also be the plane of the central accretion disk.

10.4. The Baldwin Relationship

This relation, discovered by J. Baldwin in 1977 and confirmed in several later studies, is a strong correlation between the equivalent width (EW) of *CIV*λ1549 and the continuum luminosity. It is clearly observed in radio selected samples but seems to be weaker in optical samples. In particular, quasars discovered on objective prism plates show a weak, less significant correlation. This is, perhaps, not surprising given the fact that these objects are selected by the strength of their emission lines. It is also known that the correlation is different for different lines, in particular the EW of the optical lines is not well correlated with the optical continuum luminosity. Some of the uncertainty is due to the lack of well selected, bias free samples.

The original sample studied by Baldwin covered only a small range in continuum luminosity (~ $10^{1.5}$) and resulted in a well defined slope for EW(*CIV* λ 1549) vs. L_{1549}. Later studies extended the range to more than four orders of magnitude in continuum luminosity, and to a much larger number of objects. The correlation is still present, but its slope is very different. An example is shown in Fig. 31 where the $L\alpha$ EW of more than 300 AGNs is compared with the continuum luminosity at 1215Å. The best (harmonic mean) slope in this case is -0.3, i.e.

$$EW(L\alpha) \propto L_{1215}^{-0.3}. \qquad (101)$$

A regression analysis for a sub-sample of the same data set, covering the range $10^{30} \leq L_{1215} \leq 10^{31.5}$ *erg* s^{-1} Å^{-1}, gives a much steeper slope, of 0.5, which is similar to the original slope found by Baldwin. This change of slope, as a function of the luminosity range of the sample, is a key to the understanding of the Baldwin relationship.

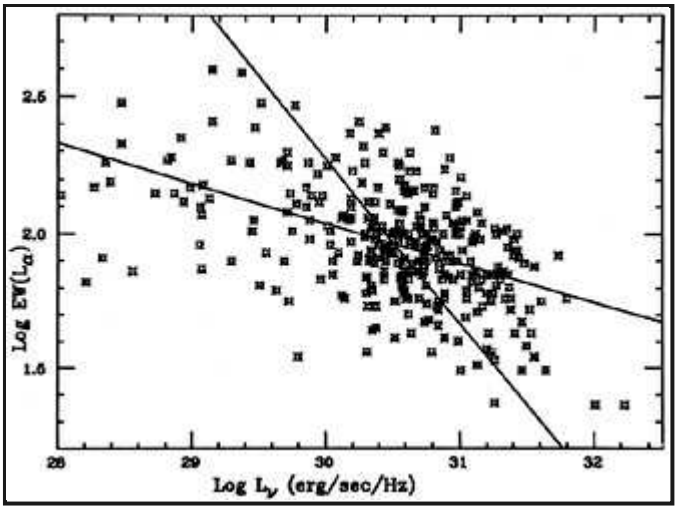

Figure 31. $L\alpha$ equivalent width vs. continuum luminosity (the Baldwin Relationship) for 328 AGNs.

Several attempts have been made to explain the Baldwin relationship. The shape of the ionizing continuum may be luminosity dependent in such a way that the continuum is "softer" in more luminous objects. Because of that the $CIV\lambda 1549$ line luminosity increases less than the continuum luminosity, resulting in smaller EW for brighter objects. This cannot be a large effect since high excitation lines, such as $NV\lambda 1240$ and $OVI\lambda 1035$, are strong in bright quasars. Alternatively, the ionization parameter in bright AGNs can be somewhat smaller than in fainter objects (see the discussion on the $L\alpha$ / CIV $\lambda 1549$ ratio in 10.2). This gives the right tendency but the difficulty with the high excitation lines is not resolved. Moreover, the Baldwin relationship for $L\alpha$ cannot be explained in this way, since there is no physical reason for a decrease in EW($L\alpha$) with increasing continuum luminosity. Photoionization calculations confirm most of these objections. They show that an increase in U can explain only a part of the effect, over a part of the observed luminosity range.

A third possibility is an inverse correlation between continuum luminosity and the covering factor. The tendency is consistent with the $L\alpha$ vs. continuum relation shown in Fig. 28, but the deduced range in covering factor is not large enough to explain the Baldwin relationship. Also, the dependence on the luminosity range is not explained.

It has been suggested that large continuum variations, that are *not* associated with corresponding emission line variations, can produce the observed correlation, This is a plausible explanation for quasars, since emission line variability in them are small compared with the continuum variability. Some confirmation of this idea comes from the fact that the Baldwin diagram for *individual* Seyfert 1 galaxies, constructed from line and continuum measurements at different phases of activity, is not very different from the original relationship found for a *sample* of bright quasars.

Lately it has been realized that the presence of geometrically thin accretion disks may introduce an EW-continuum luminosity dependence. This is discussed in the following section.

10.5. AGN Accretion Disks

10.5.1 Theoretical disk models. Theoretical justifications for accretion disks and their properties are discussed by R. Blandford. Here we limit the discussion to the observational implications of geometrically thin, optically thick, accretion disks.

The calculations of the radiation emitted by thin accretion disks, around massive black holes, are extremely complex. There were several attempts to calculate the spectrum of "bare disks", i.e. those without a corona, but none combined a full atmospheric solution with a general relativistic treatment. The most sophisticated calculations, so far, combine a full relativistic treatment with a simplified transfer solution (all examples in this chapter are from this set of calculations). Differences between existing models are large, reflecting, most probably, the different approximation used.

The following is a short summary of those results that are most relevant to the observations of AGNs.

a: The spectrum of "bare disks" with $L/L_{\rm Edd}$ ~ 0.1, gives a fair fit to the observations of many AGNs, in the spectral range 1000-6000Å. Disks around fast rotating black holes are hotter, and give a somewhat better fit to the observed spectra. The largest accretion rate allowed by the models, expressed in units of $L/L_{\rm Edd}$, is about 0.3. For larger accretion rate, the geometrical thickness of the disk is too large to be consistent with the "standard thin disk" assumption. The disks are radiation pressure

dominated and their self-gravity radius is relatively small.

b: The polarization of AGN disks is considerably smaller than the polarization of Newtonian disks, with fully scattering atmospheres.

c: The soft X-ray continuum (0.3-2 keV) of many AGNs is too strong to be fitted by the disk models that fit the observed optical-ultraviolet continuum. The hard (2-20 keV) X-ray continuum of *all* AGNs is inconsistent with standard thin disk spectra.

d: Aspect dependent effects are very important. A simple, wavelength independent limb darkening law of the form

$$F(\theta) \propto \cos\theta(1 + a\cos\theta), \tag{102}$$

with a ~ 1.5, gives a good approximation to the angle dependent flux at optical wavelengths. This limb darkening law fails at very short wavelengths, where relativistic effects dominate the emission. In particular, the continuum of an edge-on disk is much harder than that of a face-on disk. This is illustrated in Fig. 32 that shows the flux emitted by the disk at three inclination angles. The relativistic effects are important at soft X-ray energies for low luminosity AGNs, and at ultraviolet energies for high luminosity (i.e. more massive central black hole) objects.

e: The lack of a direct observational method to find the inclination angle in individual objects, implies that the fitting of AGN continua by disk models is not unique. It can amount to a factor of 10 uncertainty in the inferred central mass and accretion rate for a given object.

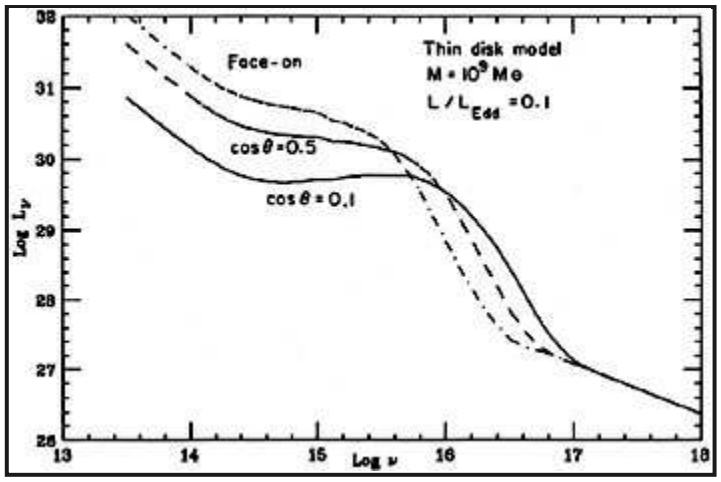

Figure 32. Theoretical thin disk spectra at three different viewing angles. The infrared and the X-ray continua are approximated by power-laws, with spectral indices of 1.4 and 0.7, respectively (courtesy of A. Laor).

A fit of a theoretical disk model to the observation of a particular quasar is shown in Fig. 33. There are three major continuum components in this fit. The first is an infrared power-law, made to fit the 1-3μm range, and extended into shorter wavelengths with the same slope. Such a component is always needed since the disk emission cannot explain the observed infrared continuum. The assumption of a power-law shape is neither certain nor essential. It is a reasonable guess over the limited wavelength range in question, but other possibilities, such as thermal emission by dust and stars, can be made to fit the data, at least in some cases. The second component is the thermal disk emission, It is about as intense as the infrared component at lμ and produces most of the emission at shorter wavelengths. There are indications that the relative contribution of this component, compared with the infrared component, is larger in more luminous objects. Finally a third, X-ray component, is needed in all cases. It dominates the emission at energies larger than about 1 keV, the energy where all disk models are found to radiate well below the observed flux. It is important to note that despite the very good match to the observed spectrum, in this and other cases, some AGN spectra cannot be fitted by any disk model calculated so far.

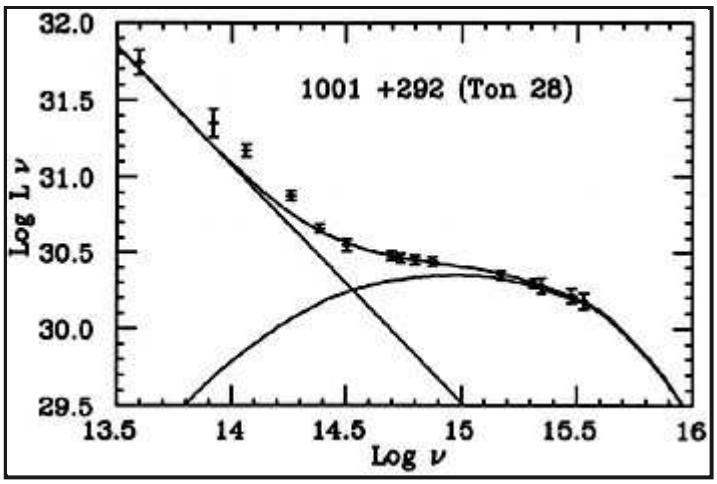

Figure 33. A model fit to the spectrum of the quasar Ton 28, showing the infrared power-law component and a theoretical disk continuum (courtesy of A. Laor).

Future, more realistic thin disk models, must incorporate several of the ingredients missing in present day calculations. The X-ray source must be given some thought. If this radiation is coming from the innermost part of the disk, then some of it may intersect the disk outer parts, changing the local energy balance and the surface temperature there. This can be due to direct illumination (flaring out of the disk or a thick central part) or via some scattering material above the disk. Hot corona is a component that can scatter the disk radiation back onto its surface, and can also be a local source of X-ray radiation. None of these have been treated in detail so far. Finally, better transfer calculations, employing full atmospheric solution, are greatly needed. They will provide the only theoretical way to answer the important question whether such disks are likely to have *emission and absorption lines and edges*. Such spectral features may turn out to be the best indications for the presence or absence of massive accretion disks in AGNs.

10.5.2 Thin accretion disks and the Baldwin relationship. The successful fitting of observed AGN continua by disk models does not give a conclusive evidence for the presence of such disks. There are other continuum emission processes that are consistent with the data and the model uncertainties are large. There are other ways to search for such disks, using viewing angle related effects. The observed disk flux depends on the inclination to the line of sight. On the other hand, the emission line flux originates, presumably, in isotropically emitting clouds, and is independent on the observer's viewing angle. Thus the line-to-continuum ratio, i.e. the line EW, is a measure of the disk inclination.

The intrinsic line/continuum ratio can differ from object to object and it is not possible to determine the disk inclination by a single EW measurement. The statistical properties of a large sample are more promising in this respect. The disk continuum flux is roughly proportional to cos θ (102) and the line EW, assuming isotropic line emission is, therefore, proportional to 1 / cos θ. The probability distribution of equivalent widths, in a sample with random disk orientations, is thus

$$P(EW)d(EW) \propto (EW)^{-2}d(EW). \qquad (103)$$

The observed EW distributions in several AGN samples is consistent with that.

Testing the EW distribution, and other disk-related phenomena, is hampered by various selection effects. Some of those are well known and are related to the discovery methods and the incompleteness of magnitude limited samples. Thin disks, if they exist, may introduce yet another selection effect. Such objects are brighter when observed face-on, which may cause the drop-out of edge-on objects from flux limited samples. The effect is most difficult to estimate in objective-prism surveys, where the objects are detected due to some combination of their continuum brightness and line strength. Searching for thin disks in big AGN samples, by ways of their characteristic EW distribution, can only be performed if the discovery technique is independent of the disk properties. Radio selected samples, especially those found by their extended, steep radio spectrum, may prove to be most appropriate for that.

An example illustrating all this is shown below. Several theoretical thin disk models, with $10^8 \leq M \leq 10^{10}\, M_{\odot}$, $0.1 \leq \cos(\theta) \leq 1$ and two values of $L/L_{\rm Edd}$, 0.1 and 0.3, were calculated to produce a set of theoretical continua. These were used in photoionization calculations to find theoretical $L\alpha$ intensities, like in chapter 4. The resulting theoretical I($L\alpha$) vs. L_{ν}(1215Å) correlation is shown in Fig. 34. The horizontal lines in the diagram are due to the fact that *a given $L\alpha$ flux* is associated with a

range of continuum fluxes, because of the disk inclination.

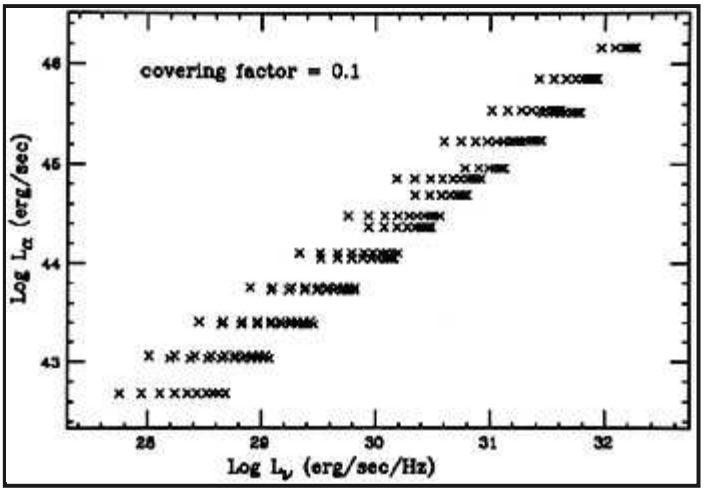

Figure 34. Theoretical $L\alpha$ vs. L_ν(1215Å) for disk continua.

The same data, transformed into an EW($L\alpha$) vs. L_{1215} by assuming a constant covering factor of 0.1, is shown in Fig. 35. The previous horizontal lines are transformed into diagonal lines and there is a tendency for EW($L\alpha$) to decrease with increasing L_{1215}. This is due to the combined effect of the disk inclination and the disk ionizing flux being softer in more luminous (larger mass) systems.

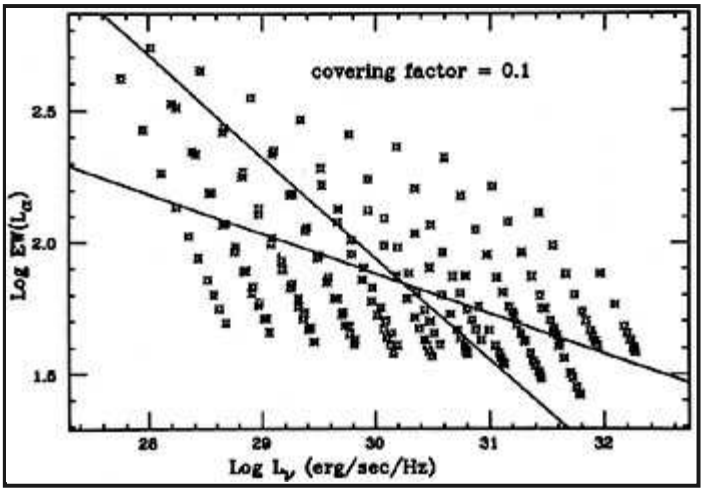

Figure 35. Theoretical EW($L\alpha$) vs. L_ν(1215Å) for AGN disks.

The theoretical distributions in Figs. 34 and 35 are similar to the observed distributions in Figs. 28 and 31, and can explain, therefore, the Baldwin relationship. They are also consistent with the observational finding that the slope of the Baldwin relation depends on the luminosity range of the sample. In this case, there is no need to assume a luminosity dependence of the covering factor or the ionization parameter. Note again the possible selection effects and the inhomogeneity of the sample used here.

10.6. Bibliography

Line-continuum correlations: There are many papers on this subject. See for example Baldwin, Gaskell and Wampler (1989), Joly (1987b) and references therein.

Line width vs. continuum luminosity: See Wandel and Yahil (1985), Joly (1987b), Mathews and Wampler (1985), Busko and Steiner (1989). The relation of the line width with the compact/extended radio luminosity ratio is discussed in Wills and Browne (1986). Some papers discussing M/L in AGNs, using line width and ionization parameters, are: Wandel and Yahil (1985), Joly et al. (1985), Wandel and Mushotzky (1986), Padovani et al. (1988) and Netzer (1989).

Thin disk models: For theoretical disk continua see Czerny and Elvis (1987), Laor and Netzer (1989), Sun and Malkan (1989),

Laor (1990) and references therein. The calculations used here are from Laor and Netzer (1989) and Laor (1990). For the polarization properties of massive disks see Laor, Netzer and Piran (1990) and references therein. Recent papers on the fitting of AGN continua by disk models are Sun and Malkan (1989), Czerny and Elvis (1987) and Laor (1990).

The Baldwin relationship: The original paper is by Baldwin (1977). Some more observational studies are described in Wampler et al. (1984), Osmer and Smith (1980), Baldwin, Wampler and Gaskell (1989) and Kinney et al (1990). The Baldwin relation in individual objects is discussed in Wamsteker and Collina (1986), Kinney et al (1990) and Edelson et al (1990). Theoretical discussion can be found in Mushotzky and Ferland (1984, dependence on U and the covering factor), Murdoch (1983, line and continuum variability) and Netzer (1985, thin disks).

11. QUASARS, MINIQUASARS AND MICROQUASARS

Much of the previous analysis focused on the broad emission lines. This limits the discussion to the more luminous AGNs, where these lines are strong and easy to measure. The aim in this chapter is to concentrate on fainter AGNs, those in which the broad lines are weak or absent. These are mostly low redshift objects showing some, but not all the AGN characteristics. Many of their observed properties have already been discussed in chapters 1 and 2, and the emphasis here is on the physical interpretation. At the end of the chapter we use the observed narrow-line properties to suggest a classification scheme for the entire AGN family.

11.1 Narrow Line X-ray Galaxies

Many of these objects have been discovered in X-ray surveys and identified, subsequently, with emission line galaxies. Some of their observed characteristics have been discussed in chapter 1. They include strong narrow lines, mostly of high excitation, strong X-ray emission and weak ultraviolet continuum. There is a great similarity in the spectral distribution of the X-ray continuum of NLXGs and Seyfert 1 galaxies.

The key to the understanding of NLXGs is the faint, broad $H\alpha$ observed in many of them. In these objects the broad $H\beta$ is extremely weak, or absent, giving a strong lower limit to the broad $H\alpha$ / $H\beta$ ratio of ~ 10. This can be understood if NLXGs are heavily reddened Seyfert 1 galaxies. Most observed differences between NLXGs and "normal" Seyfert 1s are consistent with this idea. The amount of dust is large, A_V ~ 2 mag. or so, but not large enough to absorb the hard X-ray radiation. This explains the weak ultraviolet continuum. There are some indications that the amount of reddening is correlated with the inclination of the host galaxy, with edge-on spirals showing the largest extinction. This suggests that reddening may be common in many AGNs, being less noticeable in the so called "normal" Seyferts, which, in this scheme, are located in face-on host galaxies. The dust is associated, most probably, with the interstellar medium, and is not necessarily related to the dust suspected to cause some of the broad line reddening, closer to the center (chapter 7).

11.2. Seyfert 2 Galaxies

The narrow emission lines of Seyfert 2 galaxies cover a large range of ionization. Lines from [*OI*] to [FeXI] are observed, and the spectrum is similar to the narrow line spectrum of Seyfert 1s. The equivalent width of the lines, relative to the nonstellar continuum, is systematically larger than in Seyfert 1s. The line width distribution is broad, from 250 to 900 $km\ s^{-1}$, with an average around 400 $km\ s^{-1}$. Blue asymmetry is observed in most lines, being stronger in lines of higher critical density. This again is similar to the observations of Seyfert 1 galaxies, and suggests that the higher density clouds move faster with respect to the central source.

The nonstellar optical, ultraviolet and X-ray continua of Seyfert 2 nuclei are very weak but their *ratios* are not too different from those in Seyfert 1s, thus the overall continuum *shape* is similar in the two sub-groups. The extrapolation of the observed ultraviolet continuum to high energies, does not seem to give enough ionizing flux to explain the observed emission lines (i.e. the required covering factor is larger than 1). Thus, there are several indications that much of the nonstellar continuum is not observed by us.

The key to the understanding of the difference between Seyfert 1 and Seyfert 2 galaxies is in recent polarization measurements of these objects. The degree of polarization is small, 1-3%, but when *the polarized flux* is plotted separately from the rest, as in Fig. 36, it shows, very clearly, a typical Seyfert 1 spectrum, with strong broad emission lines of hydrogen and FeII. The small fraction of polarized flux explains why this detection escaped the notice for many years. Currently there is a handful of Seyfert 2 galaxies showing this phenomenon.

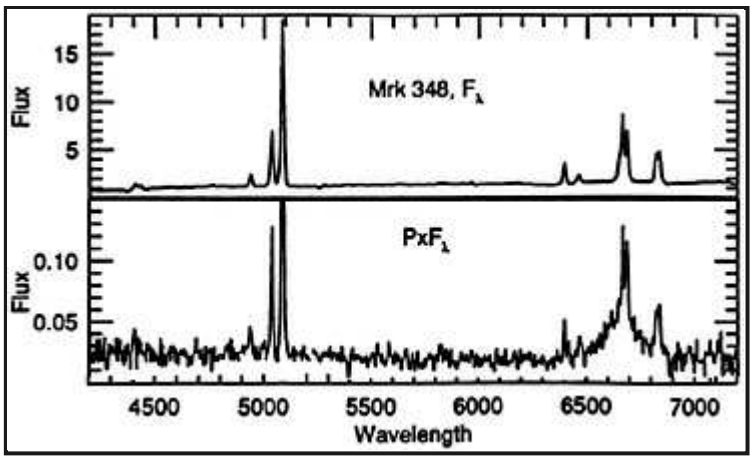

Figure 36. Top: the spectrum of the Seyfert 2 galaxy Mkn 348. Bottom: The polarized flux of Mkn 348, showing the typical broad emission lines (after Miller and Goodrich 1990).

The following physical model for Seyfert 2 galaxies has emerged (Fig. 37). A "normal" Seyfert 1 nucleus, surrounded by its BLR, is situated at the center of the system. A thick torus, of inner radius ~ 1*pc* and similar thickness, is present too. Most of the torus material is in molecular clouds, that are shielded from the central radiation by dust and by free electrons that evaporate from the clouds. The central BLR is obscured from some observers by the molecular torus. Such observers can only see the small fraction of BLR light that is scattered in their direction. The intensity of the scattered light depends on the Compton depth of the medium, and the degree of polarization on the observer's viewing angle. Some viewing angles are not obscured, and a Seyfert 1 type spectrum is observed. The NLR size greatly exceeds the dimension of the torus, and the narrow emission lines are seen by all observers. However, the NLR illumination and ionization is not isotropic, because of the torus, and the *observed* NLR is likely to attain a jet-like structure. There are radio observations and narrow emission line maps that support the claim for a jet-like NLR in Seyfert 2 galaxies.

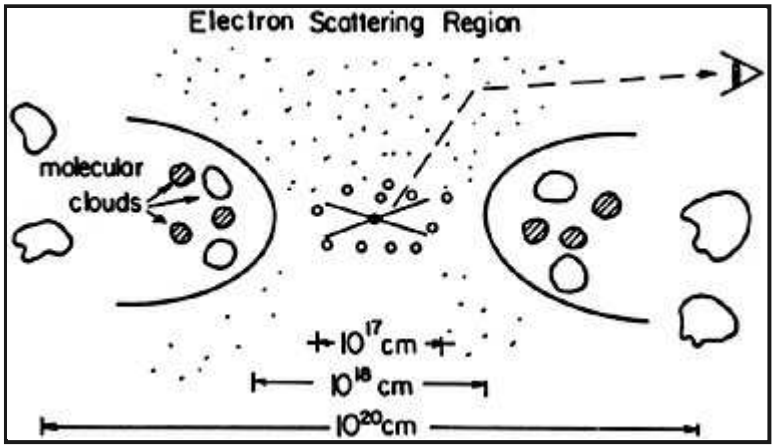

Figure 37. A unified model for Seyfert galaxies. The central source and the BLR are surrounded by a thick torus of molecular gas. The Seyfert 1 galaxies are those objects observed from the pole direction. Seyfert 2 galaxies are those sources whose inner parts can only be seen through reflected radiation.

The above model provides a natural explanation for the difference between Seyfert 1 and Seyfert 2 galaxies. One suggestion is that the different viewing direction is the only distinction between the two groups of objects. In this case the thickness and dimension of the torus can be estimated from the relative number of Seyfert 1 and Seyfert 2 galaxies. There are difficulties too, such as several well studied Seyfert 2s where the polarized flux is extremely small and no broad lines are seen. The role of dust is not very clear and heavy reddening is likely to be present, at least in some directions. Light scattered by dust is polarized in a wavelength dependent way, and there are observational ways to test this idea. The Compton depth should be large enough to scatter part of the broad line radiation, but not too large to smear out the line and continuum variability in Seyfert 1 galaxies. There are theoretical uncertainties too, to do with the structure and stability of the torus.

An alternative explanation to the differences between the two groups of galaxies is related to their variability. The broad emission lines of some Seyfert 1 galaxies exhibit a large amplitude variations. In some objects the variability so large that the spectrum at minimum light resembles a Seyfert 2 spectrum. It has been suggested that some Seyfert nuclei spend a large fraction of their active phase in a "turned-off" state, when the ionized flux is too weak to excite the gas. The recombination time of the broad line gas is short and the lines disappear several hours after the continuum decline. The recombination time of the low density gas is long enough to show strong narrow lines many years after the decline. Such an object, with strong narrow lines and weak continuum, will be classified as a Seyfert 2 galaxy. A possible cause for the drop in luminosity is a large decrease in the accretion rate. The big continuum bump observed in broad line AGNs has been attributed to emission from accretion disks. If this is indeed the case then the time scale for its fading is very long. It is hoped that future HST observations will help to decide whether the continuum of Seyfert 2 galaxies shows any sign of such a bump.

To summarize, Seyfert 2 galaxies may be Seyfert 1 nuclei that are hidden in space or in time. This may explain many, perhaps most observed properties of Seyfert 2s. However, we should not neglect the possibility of the presence of genuine narrow line objects, with no BLR at all.

11.3. LINERs

LINERs are the least luminous and the most common AGNs. At least 30% of all spirals show this phenomenon and the fraction may even be larger. LINERs show strong, low excitation emission lines, compared with the high excitation narrow lines of other AGNs. Their typical [*OII*]λ3727 / [*OIII*]λ5007 line ratio is about 1, while in Seyfert 1s it is 0.5 or less. The [*OI*]λ6300 line in LINERs is very strong and lines of [*NeV*] and [*FeVII*] are not observed. There is very little information about the ultraviolet emission lines in LINERS, a situation that is likely to change with the successful operation of the HST. A LINER spectrum is shown in Fig. 38.

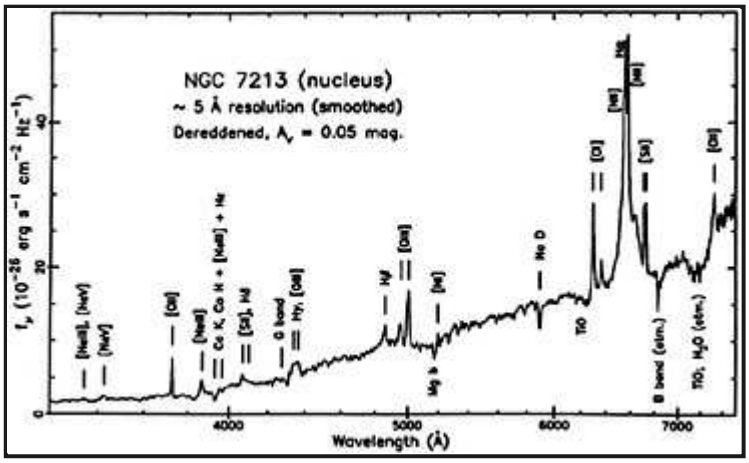

Figure 38. The spectrum of the inner region of NGC 7213, showing the typical narrow line spectrum of a LINER and weak broad $H\alpha$ wings. (Filippenko and Halpern 1986).

Typical emission line widths in LINERs are 200-400 $km\ s^{-1}$, smaller than in Seyfert galaxies and comparable to the stellar rotational velocity in the nucleus. The optical, nonstellar continuum luminosity is about 1% of the Seyfert 1 continuum luminosity, i.e. weak compared with the stellar background measured through a typical aperture of a ground-based telescope. There are clear indications, from the emission line spectrum, of ionization by a nonstellar continuum, but no direct observation of this continuum. X-ray emission has been detected in several LINERS but the optical/X-ray flux ratio of the nonstellar source is difficult to measure for the reasons explained above. For similar reasons, it is not yet clear whether the extrapolated ultraviolet continuum is intense enough to explain the observed emission lines. Thus, most of the information on LINERs comes from the analysis of their optical emission lines.

Two types of observations provide the key to the understanding of LINERs. The first is the detection, in many such objects, of faint, broad emission wings to $H\alpha$. This is demonstrated in Fig. 38 and is known to be quite common. Thus, a faint broad line region is probably present and many LINERs are faint, low excitation Seyfert 1 nuclei. Other broad emission lines are not observed and it remains to be found whether the broad lines are weak because of extinction, like in the NLXGs, obscuration or some other reason. The narrow line spectrum of LINERs is clearly distinguished from that of Seyfert galaxies, in having a much lower degree of ionization. The way to understand this is by a comparison of some emission line ratios with those of brighter AGNs. This is done by ways of constructing diagnostic diagrams, as explained below.

11.3.1 Diagnostic diagrams. Diagnostic diagrams are constructed from pairs of observed line ratios. They are very useful since different line ratios reveal different information on the ionizing continuum, the ionization parameter, the gas temperature etc. Such diagrams can help to separate blackbody photoionized nebulae from non-thermal photoionized ones and help to identify shock-excited gas. This is crucial for LINERS where the number of well measured emission lines is small, and their intensity is sometimes uncertain due to the presence of stellar absorption features. For example, the so called "Star-burst Galaxies", which are galaxies with giant nuclear HII regions, have often been confused with LINERS and line ratio diagrams can help to separate these groups.

Fig. 39 shows a diagnostic diagram that it is useful for separating HII regions, and other nebulae that are ionized by a blackbody continuum, from AGNs. The diagram compares the $[OIII]\lambda 5007$ / $H\beta$ line ratio with the $[NII]\lambda 6563$ / $H\alpha$ ratio, and is a good way of measuring the mean energy of an ionizing photon. This can be used to separate LINERs from star-burst galaxies. Another useful diagram is $[OIII]\lambda 5007$ / $H\beta$ vs. $[OII]\lambda 3727$ / $[OIII]\lambda 5007$. On this diagram the HII regions are well separated from planetary nebulae, and from object ionized by a power-law continuum, and all photoionized nebulae occupy a different region from the shock exINERs to other classes of AGNs.

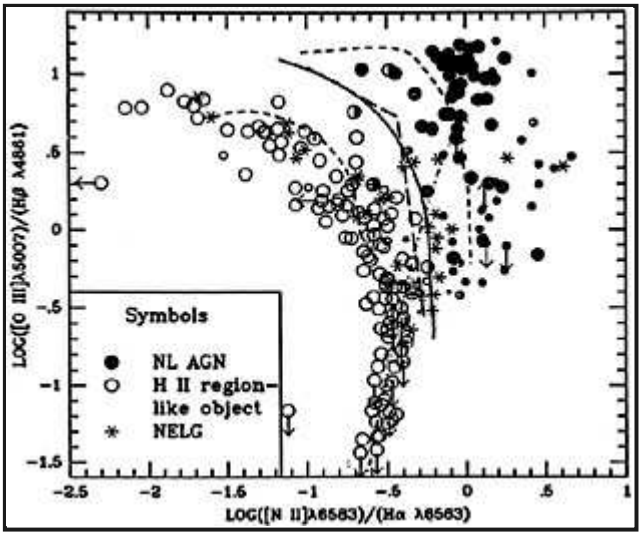

Figure 39. line ratio diagram for different emission line objects. The solid lines separate HII type objects from AGNs and the dashed lines are theoretical line ratios from several photoionization models (after Veilleux and Osterbrock, 1987).

11.3.2 Shock-wave models for LINERs. The main motivation for considering shock-wave excitation, is the observation of $[OIII]\lambda 4363$ in the spectrum of some LINERs. This line originates from the $^1S_0$ level of O^{+2}, at 5.3eV above the ground term. A strong $[OIII]\lambda 4363$ indicates a very high kinetic temperature, 40,000 K or so, which is inconsistent with photoionization, given the other observed lines. Shock-wave excitation is more consistent with such a temperature.

Shock-wave models applied to LINERs assume cloud motion through an interstellar medium, with velocities of the order of 200 $km\ s^{-1}$. The models are not entirely successful and several observed line ratios are not reproduced, despite the freedom exercised in choosing the velocity and density of the gas. The situation is not entirely clear since there are not enough constrains on such models. Future measurements of ultraviolet lines in LINERS will help to clarify the situation.

There are other uncertainties associated with $[OIII]\lambda 4363$. First, the critical de-excitation density of the line is much higher than for $[OIII]\lambda 5007$, and a large $[OIII]\lambda 4363$ / $[OIII]\lambda 5007$ ratio does not necessarily mean high temperatures. High ($\geq 10^6\ cm^{-3}$) densities could cause a similar effect. Second, measuring the line intensity is tricky because it falls in a spectral region full of stellar absorption features, and the recovery of its intrinsic intensity is uncertain. The intensity of other emission lines, such as $H\alpha$ and $H\beta$, are also affected by the stellar features.

11.3.3 Photoionization models for LINERs. Photoionization models for LINERs are motivated by the success of such models in explaining the spectrum of more luminous AGNs. The observational situation is, however, very different, since many of the important ultraviolet diagnostic lines have never been observed in LINERs. Another unknown is the shape of LINER ionizing continuum. Other uncertainties include the amount of dust and reddening, obscuration (like in Seyfert 2s) and the contamination

of the spectrum by light from nuclear HII regions.

Present photoionization models for LINERs are simple and do not treat the density and covering factor in a very sophisticated way. A power-law ionizing continuum is assumed, with a rather steep slope, to account for the weak observed HeII and other high ionization lines. Despite their limitation, such models are quite successful in explaining many emission lines, and have already revealed an important relation between LINERS and other AGNs.

Fig. 40 shows one narrow line diagnostic diagram, $[OIII]\lambda 5007$ / $H\beta$ vs. $[OII]\lambda 3727$ / $[OIII]\lambda 5007$, for a large number o AGNs. Shown also are calculated line ratios obtained in a simplified, single-cloud photoionization model, where the only variable is the ionization parameter. The density in these models is constant, 10^4 cm^{-3}, and the ionizing spectrum as in Fig. 7. There are two representative abundances, "cosmic" (Table 2) and 0.1 cosmic. As evident from the diagram, all AGNs, from luminous quasars to the faint LINERs, form a continuous sequence of decreasing ionization parameter. The bright quasars and Seyfert 1s are at the top of the diagram, with $U \simeq 10^{-2}$, Seyfert 2 galaxies have somewhat smaller U, and LINERs are characterized by $U \simeq 10^{-3.5}$. This is a strong indication that LINERs are indeed active galactic nuclei. In this respect, the narrow emission lines are the most useful indicators of AGN activity.

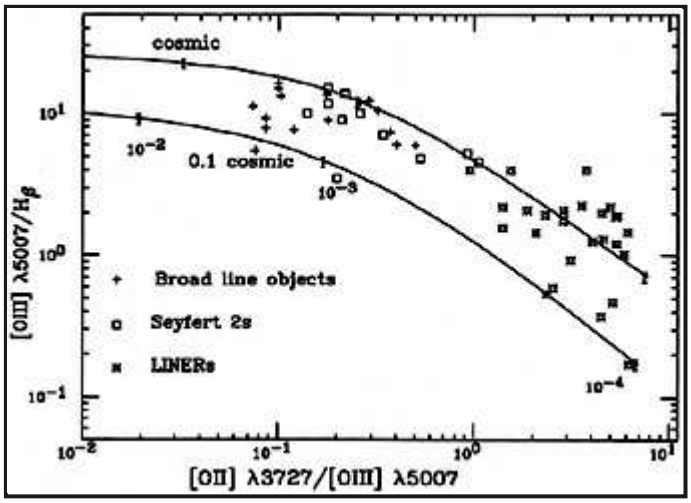

Figure 40. A line ratio diagram for AGNs. Dereddened narrow line ratios of different types of objects are shown. The continuous curves are the results of two sets of photoionization calculations, with cosmic and 0.1 cosmic abundances. These are single cloud models, with a constant density of 10^4 cm^{-3} and variable ionization parameter, as marked. The ionizing spectrum is the standard continuum adopted in this work (Fig. 7). The narrow emission lines of all AGNs seem to form a continuous sequence of decreasing ionization parameter.

There are several problems in LINERS photoionization models. The narrow $HeII\lambda 4686$ line predicted by the models is stronger than observed in many LINERs (in the particular example discussed here $HeII\lambda 4686$ / $H\beta \simeq 0.09$), and other lines are only marginally consistent with the observations. More realistic models must therefore be computed. More diagnostic diagrams can help to clarify the situation. They should be compared with the theoretical calculations and a more detailed investigation of the parameter space (density, covering factor etc.) must be perform. As for the comparison with shock-wave models, some line ratios are very promising in this respect, in particular lines of [*SII*] and [*SII*] that provide a good distinction between the two suggested mechanisms. The few observations of these lines, already obtained, seem to agree better with photoionization model calculations.

covering factor etc.) must be perform. As for the comparison with shock-wave models, some line ratios are very promising in this respect, in particular lines of [*SII*] and [*SII*] that provide a good distinction between the two suggested mechanisms. The few observations of these lines, already obtained, seem to agree better with photoionization model calculations.

11.3.4 Composite models for LINERs and Seyfert galaxies. There have been several attempts to combine shock-wave and photoionization excitation and to explain, in this way, the narrow line spectrum of LINERS and other AGNs. In this picture, the clouds are moving supersonically through the interstellar medium, being illuminated on one side by the central source. The

shocked region can be on the illuminated (infall) or the back (outflow) face of the clouds, depending on the direction of motion. There are a large number of free parameters in the model, in particular the relative emission of the photoionized and the shocked gas must be specified. It means that the cloud thickness and the covering factor are inter-related. Such models can, by careful adjustment, produce almost all the observed emission lines. It is unfortunate that the observational limitations do not allow, at this stage, a serious test of this idea.

11.4. AGN Classification: QI, QII and QIII

Despite the large diversity, all AGNs seem to share some common properties. It is therefore useful to attempt to construct a detailed classification scheme, related to as many as possible observed characteristics. The main division I propose is to three luminosity classes: QI, QII and QIII. They overlap, in luminosity, with what is sometimes called Quasars, Miniquasars (Seyfert 1 and bright Seyfert 2 galaxies) and Microquasars (faint Seyferts and LINERs). The subdivision is into spectral types, using the intensity ratio of the broad and narrow component of the permitted lines. This follows a suggestion by Osterbrock and collaborators to assign a number between 1.0 and 2.0 to each Seyfert galaxy, according to its narrow/broad line ratio. Objects of type 1.0 do not show any narrow permitted lines and objects of type 2.0 have only narrow lines. The narrow hydrogen lines of many Seyfert 1 galaxies are 10-20% as intense as the broad lines. These have been classified as Seyfert 1.5 galaxies. As for NLXGs and LINERs that show faint broad $H\alpha$ wings, they were classified as Seyfert type 1.8 or 1.9. Thus a simple way to classify Seyfert galaxies, using the broad and narrow Balmer lines, is

$$spectral\ type\ = 1 + \left[\frac{I(narrow\ line\ flux)}{I(total\ line\ flux)}\right]^{0.4}. \qquad (104)$$

Other properties are self-explanatory and are summarized in Table 3.

Table 3. AGN classification

	QI	QII	QIII
Luminosity (X+ optical)	$10^{45\text{-}47} erg\ s^{-1}$	$10^{43\text{-}45} erg\ s^{-1}$	$10^{41\text{-}43} erg\ s^{-1}$
Spectral type	1.0 - 1.5	1.0 - 2.0	1.8 - 2.0
Line width($km\ s^{-1}$)	400 - 10,000	300 - 10,000	200 - 400
continuum variability	yes	yes	not observed
line variability	in some	in most	not observed
line or continuum reddening	?	in some	in most
$[OIII]\lambda 5007 / H_\beta(narrow)$	6-12	6-12	1-2
$[OII]\lambda 3727 / [OIII]\lambda 5007$	0.1-0.3	0.1-0.6	1-5
$[NII]\lambda 6583 / H\alpha(narrow)$	0.5-1	0.3-0.8	0.8-2
$[OI]\lambda 6300 / H\alpha(narrow)$	0.05-0.3	0.05-0.3	0.1-0.6
$[SII]\lambda 6716 + 6731 / H\alpha(narrow)$	0.3-0.7	0.3-0.7	0.5-1.5
EW(H_β)	~ 100Å	10 - 100Å	1 -10Å
Ionization parameter (BLR)	0.03 - 1	0.03 - 1	?
Ionization parameter (NLR)	~ 10^{-2}	10^{-2}-10^{-3}	10^{-3}-10^{-4}

The table refers to *observed* properties, and some of the entries are still questionable. For example, the fraction of very bright objects (QI) showing any indication of reddening is not known, for reasons explained in chapter 7 (the entry in the table refers to the observed property of extinction and not to dust emission). Also, the intrinsic continuum luminosity of some QII objects (the Seyfert 2s and the NLXGs) may be much larger than indicated by their classification.

Some of the AGN properties seem to change, continuously, along the QI, QII, QIII sequence. The most obvious ones are:

The spectral type: The relative strength of the narrow emission lines increases along the sequence.

Reddening: Line and continuum reddening is more noticeable in low luminosity AGNs.

The NLR ionization parameter: Accepting the idea of photoionization as the main excitation mechanism for all classes of AGNs, the narrow emission lines seem to form a single parameter sequence, with the ionization parameter decreasing from QI to QIII.

Variability: Much more common in QI, although the observations of the non-stellar continuum, and the broad lines in the QII and QIII classes leave much to be desired.

There are glaring omissions too, most notably the central mass and accretion rate. Adding these is a real challenge for future AGN studies.

Obviously, some of the above properties, and trends, are subject to ambiguity and selection effects. Nevertheless, the connection between the sub-classes starts to reveal itself, and we are perhaps justified in looking for a common physical mechanism in all AGNs.

11.5. Bibliography

Observations of narrow line AGNs: See chapter 2. The narrow line spectrum of Seyfert 1 galaxies is discussed by Cohen (1983).

NLXGs and dust: The relation between optical and X-ray properties, and the correlation with inclination and reddening, is discussed by Lawrence and Elvis (1982). More references can be found in a review article by Lawrence (1987).

Seyfert 2 galaxies: Polarization measurements: The first paper is by Antonucci and Miller (1985). More recent work is by Miller and Goodrich (1990). For models see Krolik and Begelman (1988).

LINERs: Useful review articles are Keel (1985) and Filippenko (1989). For basic observations see chapter 2. Evidence for broad $H\alpha$ and a large range of densities is given by Filippenko and Sargent (1985, 1988).

Diagnostic diagrams: See Baldwin et al. (1981), Veilleux and Osterbrock (1987) and Kirhakos and Phillips (1989). For a discussion on the use of [*SII*] and [*SIII*] lines see Diaz et al. (1985) and Kirhakos and Phillips (1989).

Shock wave models: See Shull and McKee (1979) and Binette et al. (1984).

Photoionization models: See Ferland and Netzer (1983), Halpern and Steiner (1983), Stasinska (1984, multi-component model) and Binnette (1985, abundances) for photoionization by a power-law continuum. See Pequignot (1984) for ionization by a blackbody source.

Composite models: The basic idea and most theoretical calculations are by Contini and Aldrovandi. See Viegas-Aldrovandi and Contini (1989) for references.

REFERENCES

1. Alloin, D., Boisson, C., and Pelat, D., 1988, Astr.Ap., 200, 17.
2. Antonucci, R. and Miller, J. 1985, Ap.J., 297, 621.
3. Antonucci, R.R.J., Kinney, A.L., and Ford, H.C., 1989, Ap.J., 342, 64.
4. Averett, E.H. and Loeser, R., 1988, Ap.J., 331, 211.
5. Baldwin, J.A., 1975, Ap.J., 201, 26.
6. Baldwin, J.A., 1977, Ap.J., 214, 679.
7. Baldwin, J.A., and Netzer, H., 1978, Ap.J., 226, 1.
8. Baldwin, J.A., Phillips, M.M., and Terlevich, R., 1981, PASP, 93, 5.
9. Baldwin, J.A., Wampler, E.J. and Gaskell, G.M. 1989, Ap.J., 338, 630.
10. Bahcall, J.N., Kozlovsky, B.Z., and Salpeter, E.E., 1972, Ap.J., 171, 467.
11. Barvainis, R., 1987, Ap.J., 320, 537.
12. Binette, L., 1985, Astr.Ap., 143, 334.
13. Binette, L., Dopita, M.A., and Tuohy, I.R., 1984, Ap.J., 297, 476.
14. Blandford, R.D., and McKee, C.F., 1982, Ap.J., 255, 419.
15. Blumentha, G.R., and Mathews, W.G., 1975, Ap.J., 198, 517.
16. Blumentha, G.R., and Mathews, W.G., 1979, Ap.J., 233, 479.
17. Bonatto, C., Bica, E., and Alloin, D., 1989, Astr.Ap., 226, 23.

18. Bradeley, S.E., and Puetter, R.C., 1986, Astr.Ap., 165, 31.
19. Busko, I.C., and Steiner, J.E., 1989, MNRAS, 238, 1479.
20. Capriotti, E.R., Foltz, C.B., and Byard, P., 1980, Ap.J., 241, 903.
21. Capriotti, E.R., Foltz, C.B., and Byard, P., 1981, Ap.J., 245, 396.
22. Carroll, T.J., 1985, MNRAS, 214, 321.
23. Carroll, T.J., and Kwan, J. 1983, Ap.J., 274, 479.
24. Carroll, T.J., and Kwan, J. 1985, Ap.J., 288, 73.
25. Chen, K., Halpern, J.P., and Filippenko, A.V., 1989, Ap.J., 339, 742.
26. Clavel, J., and Wamsteker, W., 1987, Ap.J.Lett., 320, L9.
27. Clavel, J., Wamsteker, W., and Glass, I., 1989 Ap.J., 337, 236.
28. Clavel et al. 1990, Ap.J., (in press)
29. Cohen, R.D., 1983, Ap.J., 273, 489.
30. Collin-Souffrin, S., 1986, Astr.Ap., 166, 115.
31. Collin-Souffrin, S., Dyson, J.E., McDowell, J.C, and Perry, J.J., 1988, MNRAS, 232, 539.
32. Collin-Souffrin, S., and Dumont, A.M., 1986, Astr.Ap., 166, 13.
33. Collin-Souffrin, S., and Dumont, A.M., 1989, Astr.Ap., 213, 29.
34. Collin-Souffrin, S., and Dumont, A.M., 1990, Astr.Ap., 229, 292.
35. Collin-Souffrin, S., Hameury, J.M. and Joly, M., 1988, Astr.Ap., 205, 19.
36. Corbin, M.R., 1990, Ap.J., 357, 346.
37. Cota, S.A., and Ferland, G.J., 1988, Ap.J., 326, 889.
38. Czerny, B. and Elvis, M., 1987, Ap.J., 312, 325.
39. Crenshaw, D.M., 1986, Ap.J.Suppl., 62, 821.
40. Davidson, K., 1972, Ap.J., 171, 213.
41. Davidson, K., and Netzer, H. 1979, Rev.Mod.Phys., 51, 715.
42. De Robertis, M., 1985, Ap.J., 289, 67.
43. De Robertis, M., and Osterbrock, D.E., 1984, Ap.J., 286, 171.
44. De Robertis, M., and Osterbrock, D.E., 1986, Ap.J., 301, 727.
45. De Zotti, G., and Gaskell, C.M., 1985, Astr.Ap., 147, 1.
46. Diaz, A.I., Pagel, B.E.J., and Wilson, R.G., 1985, MNRAS, 212, 737.
47. Dumont, A.M., and Collin-Souffrin, S., 1990, Astr.Ap., 229, 302.
48. Eastman, R.G., and MacAlpine, G.M., 1985, Ap.J., 299, 785.
49. Edelson, R.A., and Krolik, J.H., 1989, Ap.J., 333, 646.
50. Elitzur, M., 1984, Ap.J., 280, 653.
51. Elitzur, M., and Ferland, G.J., 1986, Ap.J., 309, 35.
52. Elitzur, M., and Netzer, H., 1984, Ap.J., 291, 464.
53. Espey, B.R, Carswell, R.F., Bailey, A., Smith, M.G., and Ward, M.J, 1989, Ap.J., 342, 666.
54. Fabian, A.C., Guilbert, P.W., Arnud, K., Shafer, R.A., Tennant, A.F. and Ward, M.J., 1986, MNRAS, 218, 457.
55. Ferland, G.J., and Mushotzky, R.F., 1984, Ap.J., 286, 42.
56. Ferland, G.J., and Netzer, H., 1979, Ap.J., 229, 274.
57. Ferland, G.J., and Osterbrock, D.E., 1986, Ap.J., 300, 658.
58. Ferland, G.J., and Rees, M.J., 1988, Ap.J., 332, 141.
59. Ferland, G.J., and Persson, S.E., 1989, Ap.J., 347, 656.
60. Ferland, G.J., and Shields, G.A., 1985 in *Astrophysics of Active Galaxies and Quasi-Stellar Objects* (J.Miller ed. p.157)
61. Ferland, G.J., Netzer, H., and Shields, G.A., 1979, Ap.J., 232, 382.
62. Filippenko, A.V., in *Active Galactic Nuclei*, 1989 (IAU Symp. 134) p.495.
63. Filippenko, A.V. and Halpern, J.P. 1984, Ap.J., 286, 485.
64. Fillipenko, A.V., and Sargent, W.L.W., 1985, Ap.J.Suppl., 57, 503.
65. Fillipenko, A.V., and Sargent, W.L.W., 1988, Ap.J., 324, 134.
66. Gaskell, M., 1982, Ap.J., 263, 79.
67. Gaskell, M., and Peterson, B.M., 1987, Ap.J.Suppl., 65, 1.
68. Gaskell, M., and Sparke, 1986, Ap.J., 305, 175.
69. Gaskell, C.M., Shields, G.A., and Wampler, E.J., 1981, Ap.J., 249, 443.
70. Gondhalekar, P.M., 1990, MNRAS, 243, 443.
71. Goodrich, R.W., 1989, Ap.J., 340, 190.
72. Goodrich, R..W., 1990, Ap.J., 355, 88.
73. Halpern, J.P., and Filippenko, 1988, Nature, 331, 46.
74. Halpern, J.P. and Steiner, J., 1983, Ap.J., 269, 137.
75. Hubbard, E.M., and Puetter, R.C., 1985, Ap.J., 290, 394.
76. Hummer, D.G., 1968, MNRAS, 138, 73.
77. Hummer, D.G., and Kunasz, P.B., 1980, Ap.J., 236, 609.
78. Joly, M., 1987a, Astr.Ap., 184, 33.

79. Joly, M., 1987b, in *Emission Lines in Active Galactic Nuclei*, (P. Gondhalekar ed. p160)
80. Joly, M., Collin-Souffrin, S., Masnou, J.L., and Nottale, L, 1985, Astr.Ap., 152, 282.
81. Kalkofen, W. (editor) 1984, *Methods in Radiative Transfer* (Cambridge University Press).
82. Kallman, T. and Krolik, J., 1986, Ap.J., 308, 805.
83. Kallman, T., and McCray, R. 1982, Ap.J.Suppl., 50, 263.
84. Kawara, K., Nishida, M., and Gregory, B., 1990, Ap.J., 352, 433.
85. Kazanas, D., 1989, Ap.J., 347, 74.
86. Keel, W.C., 1983, Ap.J., 269, 466.
87. Keel, W.C., 1985 in *Astrophysics of Active Galaxies and Quasi-Stellar Objects* (J.Miller ed. p.1)
88. Kinney, A.L., Rivolo, A.R., and Koratrar, A.P., 1990, Ap.J., 357, 338.
89. Kirhakos, S., and Phillips, M.M., 1989, PASP, 101, 949.
90. Korista, K.T., and Ferland, G.J., 1989, Ap.J., 343, 678.
91. Koski, 1978, Ap.J., 223, 56.
92. Krolik, J.H., 1988, Ap.J., 325, 148.
93. Krolik, J , H., and Begelman, M.C., 1988, Ap.J., 329, 702.
94. Krolik, J., and Kallman, T.A., 1988, Ap.J., 324, 714.
95. Krolik, J., McKee, C.M. and Tarter, C.B., 1981, Ap.J., 249, 422.
96. Kwan, J., 1984, Ap.J., 283, 70.
97. Kwan, J., and Krolik, J.H., 1981, Ap.J., 250, 478.
98. Kwan, J., and Carroll, T.J., 1982, Ap.J., 261, 25.
99. Laor, A., 1990, MNRAS, (in press)
100. Laor, A., and Netzer, H., 1989, MNRAS, 238, 897.
101. Laor, A., Netzer, H., and Piran, T., 1990, MNRAS, 242, 560.
102. Lawrence, A., and Elvis, M., 1982, Ap.J., 256, 410.
103. Lawrence, A., 1987, PASP, 99, 30.
104. Lockett, P., and Elitzur, M., 1989, Ap.J., 344, 525.
105. Maoz, D., and Netzer, H., 1989, MNRAS, 236, 21.
106. Maoz, D., Netzer, H., Mazeh, T., Beck, S., Almoznino, E., Leibowitz, E., Brosch, N., Mendelson, H., and Laor, A., 1991, Ap.J., (in press)
107. MacAlpine, G.M., 1972, Ap.J., 175, 11.
108. MacAlpine, G.M., 1985 in *Astrophysics of Active Galaxies and Quasi-Stellar Objects*, (J.Miller ed. p.259)
109. MacAlpine, G.M., Davidson, K., Gull, T.R., and Wu, C.C., 1985, Ap.J., 294, 147.
110. Martin, P.G., and Ferland, G.J., 1980, Ap.J.Lett., 235, L125.
111. Mathews, W.G., 1974, Ap.J., 189, 23.
112. Mathews, W.G., 1982a, Ap.J., 252, 39. 156
113. Mathews, W.G., 1982b, Ap.J., 258, 425.
114. Mathews, W.G., and Wampler, J., 1985, PASP, 97, 966.
115. Mathews, W.G., and Doane, J.S., 1990, Ap.J., 352, 423.
116. Mathews, W.G., and Ferland, G.J., 1987, Ap.J., 323, 456.
117. Mathews, W.G., and Capriotti, E.R., 1985, in *Astrophysics of Active Galaxies and Quasi-Stellar Objects* (J.Miller ed. p.185)
118. Mihalas, D., 1978, *Stellar Atmospheres*, (San Francisco: Freeman)
119. Miley, G.K., and Miller, J.S., 1979, Ap.J.Lett., 228, L55.
120. Miller, J.S., and Goodrich, B.F., 1990, Ap.J., 355, 456.
121. Morris, S.L., and Ward, M.J., 1988, MNRAS, 230, 639.
122. Murdoch, H.S., 1983, MNRAS, 202, 987.
123. Mushotzky, R.F., and Ferland G.J., 1984, Ap.J., 278, 558.
124. Netzer, H., 1985a, Ap.J., 289, 451.
125. Netzer, H., 1985b, MNRAS, 216, 63.
126. Netzer, H., 1987, MNRAS, 225, 55.
127. Netzer, H., 1989, Comments on Astrophysics, 14, 137.
128. Netzer, H., and Davidson, K. 1979, MNRAS, 187, 871.
129. Netzer, H., Elitzur, M., and Ferland, G.J., 1985, Ap.J., 299, 752.
130. Netzer, H., and Ferland, G.J., 1984, PASP, 96, 593.
131. Osmer, P.S., 1980, Ap.J.Suppl., 42, 523.
132. Osmer, P.S., and Smith, M.G., 1980, Ap.J.Suppl., 42, 333.
133. Osterbrock, D.E., 1977, Ap.J., 215, 733.
134. Osterbrock, D.E., 1984, Q.J.R.Asrt.Soc., 25, 1.
135. Osterbrock, D.E., 1989, *Astrophysics of Gaseous Nebulae and Active Galactic Nuclei* (University Science Books)
136. Osterbrock, D.E., Koski, A.T., and Phillips, M.M, 1976, Ap.J., 206, 898.
137. Osterbrock, D.E., and Mathews, W.G., 1986, Ann.Rev.Ast.Ap., 24, 171.

138. Osterbrock, D.E., Shaw, R.A., and Veilleux, S., 1990, Ap.J., 352, 561.
139. Osterbrock, D.E., and Shuder, J.M., 1982, Ap.J.Suppl., 49,
140. Padovani, P., Burg, R., and Edelson, R.A., 1990, Ap.J., 353, 438.
141. Penston, M.V., 1987, MNRAS, 229, 1p.
142. Penston, M.V., 1988, MNRAS, 233, 601.
143. Penston, M.V., and Perez, E., 1984, MNRAS, 211, 33p.
144. Penston, M.V., Croft, S., Basu, D., and Fuller, N., 1990, MNRAS, 244, 357.
145. Perez, E., Penston, M.V., Tadhunter, C., Mediavilla, E., and Moles, M., 1988, MNRAS, 230, 353.
146. Perez, E., Penston, M.V., and Moles, M., 1989, MNRAS, 239, 75.
147. Perez, E., Penston, M.V., Tadhunter, C., Mediavilla, E., and Moles, M, 1987, MNRAS, 230, 353.
148. Perry, J.J., and Dyson, J.E., 1985, MNRAS, 213, 665.
149. Persson, S.E., 1988, Ap.J., 330, 751.
150. Peterson, B.M., 1988, PASP, 100, 18.
151. Peterson, B.M., et al., 1991, Ap.J., in press.
152. Puetter, R.C., 1981, Ap.J., 251, 446.
153. Puetter, R.C., and Hubbard, E.N., 1985, Ap.J., 295, 394.
154. Puetter, R.C., and Hubbard, E.N., 1987, Ap.J., 320, 85.
155. Rees, M., 1987, MNRAS, 228, 47p.
156. Rees, M., Netzer, H. and Ferland, 1989, Ap.J., 347, 640.
157. Reichert, G.A., Mushotzky, R.F., Petre, R., and Holt, S.S., 1985, Ap.J., 296, 69.
158. Robinson, A., and Perez, E., 1990, MNRAS, 244, 138.
159. Rudy, R.J., and Schmidt, G.D., 1988, Ap.J., 331, 325.
160. Sanders, D.B., Phinney, E.S., Neugebauer, G., Soifer, B.T., and Matthews, K., 1989, Ap.J., 347, 29.
161. Sargent, W.L.W., Steidel, C.C., and Boksenberg, A., 1988, Ap.J.Suppl., 69, 703.
162. Schneider, D.P., Schmidt, M., and Gunn, J.E., 1989, A.J., 98, 1507.
163. Scoville, N., and Norman, C., 1988, Ap.J., 332, 163.
164. Shull, M.J.M, and McKee, C.E., 1979, Ap.J., 227, 131.
165. Shull, J.M,, and Van Steenberg, M.E., 1985, Ap.J., 298, 268.
166. Shields, G.A., 1976, Ap.J., 204, 330.
167. Shields, G.A., 1978, Nature, 272, 706.
168. Shields, G.A., 1989, in *Active Galactic Nuclei*, (IAU Symp. 134) p.577.
169. Shlosman, I., Vitello, P.A., and Shaviv, G., 1985, Ap.J., 294, 96.
170. Smith, M.G., Carswell, R.F., Whelan, J.A.J., Wilkes, B.J., Boksenberg, A., Clowes, R.G., Savage, A., Cannon, R.D., and Wall, J.V., 1981, MNRAS, 195, 437.
171. Smith, M.D., and Raine, D.J., 1985, MNRAS, 212, 425.
172. Stasiaska, G., 1984, Astr.Ap., 135, 341.
173. Stirpe, G.M., van Groningen, E., and de Bruyn, A.G., 1989, Astr.Ap., 211 , 31.
174. Sulentic, J.W., 1989, Ap.J., 343, 54.
175. Sun, W.H., and Malkan, M.A., 1989, Ap.J., 346, 68.
176. Terlevich, R., and Melnick, J., 1988, Nature, 333, 239.
177. Terlevich,R., 1989, in *Evolutionary Phenomena in Galaxies* (Beckman and Pagel ed. Cambridge Univ. Press)
178. Uomoto, A., 1984, Ap.J., 284, 497.
179. Veilleux, S., and Osterbrock, D.E., 1987, Ap.J.Suppl., 63, 295.
180. Viegas-Aldrovandi, S.M., and Gruenvald, R.B., 1988, Ap.J., 324, 683.
181. Viegas-Aldrovandi, S.M., and Contini, M., 1989, Ap.J., 339, 689.
182. Voit, G.M., and Shull, J.M., 1988, Ap.J., 331, 197.
183. Wamsteker, W., and Colina, L., 1986, Ap.J., 311, 617.
184. Wamsteker, W., Rodriguez-Pascual, P, Wills, B.J., Netzer, H., Wills, D., Gilmozzi, R., Barylak, M., Talavera, A., Maoz, D., Barr, P., and Heck, A., 1990, Ap.J., 354, 446.
185. Wampler, E.J., Gaskell, C.M., Burk, W.L. and Baldwin, J.A., 1984, Ap.J., 276, 403.
186. Wandel, A., and Yahil, A., 1985, Ap.J., 295, L1.
187. Wandel, A., and Mushotzky, R.F., 1986, Ap.J.Lett., 306, L61.
188. Ward, M.J., Geller, T., Smith, M., Wade, R., and Williams, P., 1987, Ap.J., 316, 138.
189. Whittle, M. 1985a, MNRAS, 213, 1.
190. Whittle, M. 1985b, MNRAS, 216, 817.
191. Wilkes, B.J., 1986, MNRAS, 218, 331.
192. Wilkes, B.J. and Carswell, R.F., 1982, MNRAS, 201, 645.
193. Weymann, R.J., and Williams, R.E. 1969, Ap.J., 157, 1201.
194. Wills, B.J., Netzer, H., and Wills, D., 1985, Ap.J., 288, 94.
195. Wills, B.J., and Browne, I.W., 1986, Ap.J., 302, 56.
196. Wu, C.C., Boggess, A., and Gull, T.R., 1983, Ap.J., 266, 28.

197. Zheng, W., 1988, Ap.J., 333, 188.
198. Zheng, W., and O'Brien, P.T., 1990, Ap.J., 356, 463.

LIST OF SYMBOLS

$A_c(r)$	Cloud cross section
A_{ji}	Radiative transition rate
a	Damping constant
B_{ij}	Aborption coefficient
b_i	Derture coefficient for level i
C_{ij}	Collisional excitation rate
$C(r)$	Cumulative covering factor (up to distance r)
c	Velocity of light
c_s	Sound speed
$E_l(r)$	Cumulative line flux (up to distance r)
$E\lambda$	Line profile
$E(t)$	Emission line light curve
E_{ij}	Energy separation of levels ij
EW	Equivalent width
F_ν	Monochromatic continuum flux
f_d	Drag force
f_{ij}	Oscillator strength
G	Gravitational constant
g_{ff}	Gaunt factor for free-free transition
g_G	Gravitational acceleration
g_i	Statistical weight of level i
g_{rad}	Radiative acceleration
h	Planck's constant
I_ν	Radiation intensity
J	Mean radiation intensity
$j_c(r)$	Total cloud emission
k	Boltzmann constant
$k(\tau)$	Number of scattering factor
$k'(\tau)$	Path length increase factor
L	Integrated continuum luminosity
L_{46}	Luminosity in 10^{46} $erg\ s^{-1}$
L_ν	Monochromatic continuum luminosity
$L(t)$	Continuum light curve
L_{Edd}	Eddington luminosity
M_c	Mass of a cloud
M_{BH}	Mass of the central black hole
M_9	M_{BH} / 10^9 $M_\odot$
$\dot{M}$	Accretion rate
$\dot{m}$	Accretion rate in units of L/L_{Edd}

m_e	Electron mass
m_p	Proton mass
$m\lambda$	Magnitude of extinction
N	Particle number density
N_{10}	$N / 10^{10}\ cm^{-3}$
N_e	Electron density
N_{HIM}	Density of the hot inter-cloud medium
N_{col}	Column density
$n_c(r)$	Number of clouds per unit volume at distance r
n_i	Population of level i
P	Pressure
$Q(\tau)$	Number of scattering before escape
R_c	Radius of a cloud
r	Distance of a cloud
r_{av}	Emissivity-weighted average radius
r_{in}	Inner radius of the emission line region
r_{out}	Outer radius of the emission line region
S	Source function
T_C	Compton temperature
T_e	Electron temperature
T_{ex}	Excitation temperature
T_{HIM}	Temperature of the hot inter-cloud medium
T_{rad}	Radiation temperature
t_{dyn}	Dynamical time
t_{rec}	Recombination time
t_{sc}	Sound-crossing time
U	Ionization parameter
V_c	Volume of a cloud
$v(r)$	Cloud velocity at a distance r
$v_{Doppler}$	Doppler velocity
v_{3000}	$v/3000\ km\ s^{-1}$
X_c	Relative continuum opacity
X_l	Relative line opacity
Z	Nuclear charge
z	Redshift
α	Recombination coefficient
α_T	Temperature averaged recombination coefficient
β	Escape probability
β_{eff}	Effective escape probability
γ	Continuum spectral index
$\varepsilon_l(r)$	Line emission ($erg\ s^{-1}\ cm^{-2}$)

ε_ν	Line emission coefficient
η_ν	Continuum occupation number
κ_ν	Line absorption coefficient
κ_c	Continuum absorption cross section at line center
κ_l	Line absorption cross section at line center
λ_{ij}	Wavelength of the *ij* transition
λ_0	Line center wavelength
μ	cos θ in a spherical coordinate system
ν	Frequency
ν_0	Threshold ionization frequency
$\bar{\nu}$	Mean photon frequency or mean photon energy
ν_{cut}	Cut-off frequency
Ξ	(radiation pressure) / (gas pressure) $\propto U/T$
σ_ν	Continuum absorption cross section
σ_c	Effective Compton cooling cross section
σ_{es}	Electron scattering cross section
σ_h	Effective Compton heating cross section
τ	Optical depth
τ_{in}	Optical depth to the inner (illuminated) face of the cloud
τ_{out}	Optical depth to the outer face of the cloud
Φ_ν	Normalized line profile
$\Psi(t)$	Transfer function
Ω_{ij}	Effective collision strength
ω	1 / *t*